Fall 2011

Tris(guanidinato)complexes of iridium and rhodium in the oxidation states +III and +IV: synthesis, characterization, and reactivity

Wei-Tsung Lee
University of Iowa

TRIS(GUANIDINATO) COMPLEXES OF IRIDIUM AND RHODIUM IN THE OXIDATION STATES +III AND +IV: SYNTHESIS, CHARACTERIZATION, AND REACTIVITY

by

Wei-Tsung Lee

An Abstract

Of a thesis submitted in partial fulfillment
of the requirements for the Doctor of
Philosophy degree in Chemistry
in the Graduate College of
The University of Iowa

December 2011

Thesis Supervisor: Assistant Professor Jan-Uwe Rohde

ABSTRACT

Mononuclear [Ir{ArNC(NR$_2$)NAr}(C$_8$H$_{14}$)$_2$] complexes (where R = Me or Et; Ar = Ph or 4-MeC$_6$H$_4$; and C$_8$H$_{14}$ = *cis*-cyclooctene) were synthesized from the neutral *N*,*N*-dialkyl-*N*′,*N*′′-diarylguanidines via deprotonation and transmetalation. As confirmed by single-crystal structure determination, the guanidinato(1−) ligands coordinate the low-valent d^8 Ir^{I} center in an N,N′-chelating binding mode, and the C–N distances of the CN$_3$ core suggest that these ligands function as stronger donors than related monoanionic, bidentate nitrogen-based ligands. In the reaction of the complexes with O$_2$, new [Ir{ArNC(NR$_2$)NAr}]$_3$ complexes were identified among the products, suggesting a new route for their synthesis.

Tris(guanidinato) complexes of Ir^{III}, [Ir{ArNC(NR$_2$)NAr}$_3$] (R = Me or Et; Ar = Ph or 4-MeC$_6$H$_4$), were synthesized and, as revealed by electrochemical measurements, can be oxidized reversibly at unusually low potentials. These potentials are even lower than those of other Ir^{III} complexes with very electron-rich, trianonic ligand sets as, for example, in cyclometalated tris(2-pyridylphenyl), corrolato and tris(dithiocarbamato) complexes. Chemical oxidation by [FeCp$_2$]PF$_6$ afforded isolable, paramagnetic Ir^{IV} compounds, [Ir{ArNC(NR$_2$)NAr}$_3$]PF$_6$, which were characterized by elemental analysis, mass spectrometry, electronic absorption and EPR spectroscopy and X-ray crystallography. The reactivity of these Ir^{IV} complexes toward mild inorganic and organic reductants and substrates with O–H bonds was investigated.

Similar tris(guanidinato) complexes of Rh^{III}, [Rh{ArNC(NR$_2$)NAr}$_3$] (R = Me or Et; Ar = Ph, 4-MeC$_6$H$_4$ or 4-MeOC$_6$H$_4$), were synthesized. These complexes also were oxidized reversibly at low potentials, as compared to the corresponding tris(amidinato) and tris(triazenido) complexes. Chemical oxidation by [FeCp$_2$]PF$_6$ afforded thermally unstable, paramagnetic Rh^{IV} compounds, [Rh{ArNC(NR$_2$)NAr}$_3$]PF$_6$, which were characterized by mass spectrometry and electronic absorption spectroscopy.

Furthermore, two Fe^{II} complexes of tetradentate tripodal ligands, [Fe(**L1**)$(OTf)_2$] and [Fe(**L2**)$(OTf)_2$]; where **L1** = *N*,*N*-bis(2-benzimidazolylmethyl)-*N*-(2-pyridylmethyl) amine and **L2** = *N*,*N*-bis[(1-methylbenzimidazol-2-yl)methyl]-*N*-[(pyridin-2-yl)methyl] amine; were synthesized and characterized. The ^1H NMR spectra for [Fe(**L1**)$(NCMe)_2$]$(OTf)_2$ and [Fe(**L2**)$(NCMe)_2$]$(OTf)_2$ in CD_3CN solution at ambient temperature exhibit paramagnetically shifted peaks typical of high-spin Fe^{II} complexes, while variable-temperature ^1H NMR spectroscopy showed that the Fe center in [Fe(**L1**)$(NCMe)_2$]$(OTf)_2$ is in a spin equilibrium and that in [Fe(**L2**)$(NCMe)_2$]$(OTf)_2$ in the high-spin state (at 25 °C). Highly reactive oxoiron(IV) complexes were obtained by reaction of the Fe^{II} complexes with an excess of *m*-CPBA at –40 °C.

Abstract Approved: _____
Thesis Supervisor

_____
Title and Department

_____
Date

TRIS(GUANIDINATO) COMPLEXES OF IRIDIUM AND RHODIUM IN THE OXIDATION STATES +III AND +IV: SYNTHESIS, CHARACTERIZATION, AND REACTIVITY

by

Wei-Tsung Lee

A thesis submitted in partial fulfillment
of the requirements for the Doctor of
Philosophy degree in Chemistry
in the Graduate College of
The University of Iowa

December 2011

Thesis Supervisor: Assistant Professor Jan-Uwe Rohde

Graduate College
The University of Iowa
Iowa City, Iowa

CERTIFICATE OF APPROVAL

_____

PH.D. THESIS

_____

This is to certify that the Ph.D. thesis of

Wei-Tsung Lee

has been approved by the Examining Committee
for the thesis requirement for the Doctor of Philosophy
degree in Chemistry at the December 2011 graduation.

Thesis Committee: _____
Jan-Uwe Rohde, Thesis Supervisor

_____
Maxwell L. Geng

_____
Edward G. Gillan

_____
F. Christopher Pigge

_____
Eric E. Nuxoll

ACKNOWLEDGMENTS

I want to first thank my advisor, Jan-Uwe Rohde. I owe most of my abilities as a scientist to his high standards and excellent advisement.

I thank Profs. Lei Geng, Edward Gillan, Chris Pigge, and Eric Nuxoll for being on my committee and their valuable suggestions.

I would also like to thank the following people in the Department of Chemistry for their help over the years: Dale for the acquisition of crystallographic data and solving twinned structures; Peter for his great help with all of my glass needs; and Santana for his help and discussion with NMR spectroscopy.

The friendliness from my labmates is fruitful and makes me feel I am not alone in Iowa. I would also like to thank the following group members: Matt, Travis, Tony, and Jeong-Ah for their supports and providing such a wonderful research environment.

There are many friends in Iowa City I wish to give them my thanks. They also helped me getting through many difficulties.

Further, I would like to thank my wife Ai-Ting who has been incredibly helpful during my job-seeking and dissertation-writing processes. I surely would have had a much more difficult time without her in my life, sharing laughs and tears. She is a great partner and ally.

Finally, I must thank my parents who have inspired and supported me in many ways. I have been blessed with an amazing family and I could not have done this without them.

ABSTRACT

Mononuclear [Ir{ArNC(NR$_2$)NAr}(C$_8$H$_{14}$)$_2$] complexes (where R = Me or Et; Ar = Ph or 4-MeC$_6$H$_4$; and C$_8$H$_{14}$ = *cis*-cyclooctene) were synthesized from the neutral *N*,*N*-dialkyl-*N*′,*N*′′-diarylguanidines via deprotonation and transmetalation. As confirmed by single-crystal structure determination, the guanidinato(1−) ligands coordinate the low-valent d^8 Ir^{I} center in an N,N′-chelating binding mode, and the C–N distances of the CN$_3$ core suggest that these ligands function as stronger donors than related monoanionic, bidentate nitrogen-based ligands. In the reaction of the complexes with O$_2$, new [Ir{ArNC(NR$_2$)NAr}]$_3$ complexes were identified among the products, suggesting a new route for their synthesis.

Tris(guanidinato) complexes of Ir^{III}, [Ir{ArNC(NR$_2$)NAr}$_3$] (R = Me or Et; Ar = Ph or 4-MeC$_6$H$_4$), were synthesized and, as revealed by electrochemical measurements, can be oxidized reversibly at unusually low potentials. These potentials are even lower than those of other Ir^{III} complexes with very electron-rich, trianonic ligand sets as, for example, in cyclometalated tris(2-pyridylphenyl), corrolato and tris(dithiocarbamato) complexes. Chemical oxidation by [FeCp$_2$]PF$_6$ afforded isolable, paramagnetic Ir^{IV} compounds, [Ir{ArNC(NR$_2$)NAr}$_3$]PF$_6$, which were characterized by elemental analysis, mass spectrometry, electronic absorption and EPR spectroscopy and X-ray crystallography. The reactivity of these Ir^{IV} complexes toward mild inorganic and organic reductants and substrates with O–H bonds was investigated.

Similar tris(guanidinato) complexes of Rh^{III}, [Rh{ArNC(NR$_2$)NAr}$_3$] (R = Me or Et; Ar = Ph, 4-MeC$_6$H$_4$ or 4-MeOC$_6$H$_4$), were synthesized. These complexes also were oxidized reversibly at low potentials, as compared to the corresponding tris(amidinato) and tris(triazenido) complexes. Chemical oxidation by [FeCp$_2$]PF$_6$ afforded thermally unstable, paramagnetic Rh^{IV} compounds, [Rh{ArNC(NR$_2$)NAr}$_3$]PF$_6$, which were characterized by mass spectrometry and electronic absorption spectroscopy.

Furthermore, two Fe^{II} complexes of tetradentate tripodal ligands, [Fe(**L1**)$(OTf)_2$] and [Fe(**L2**)$(OTf)_2$]; where **L1** = *N*,*N*-bis(2-benzimidazolylmethyl)-*N*-(2-pyridylmethyl) amine and **L2** = *N*,*N*-bis[(1-methylbenzimidazol-2-yl)methyl]-*N*-[(pyridin-2-yl)methyl] amine; were synthesized and characterized. The ^1H NMR spectra for [Fe(**L1**)$(NCMe)_2$]$(OTf)_2$ and [Fe(**L2**)$(NCMe)_2$]$(OTf)_2$ in CD_3CN solution at ambient temperature exhibit paramagnetically shifted peaks typical of high-spin Fe^{II} complexes, while variable-temperature ^1H NMR spectroscopy showed that the Fe center in [Fe(**L1**)$(NCMe)_2$]$(OTf)_2$ is in a spin equilibrium and that in [Fe(**L2**)$(NCMe)_2$]$(OTf)_2$ in the high-spin state (at 25 °C). Highly reactive oxoiron(IV) complexes were obtained by reaction of the Fe^{II} complexes with an excess of *m*-CPBA at –40 °C.

TABLE OF CONTENTS

LIST OF TABLES

LIST OF FIGURES

LIST OF SCHEMES

CHAPTER 1

INTRODUCTION

This thesis covers the synthesis, characterization, and reactivity of iridium and rhodium complexes. The results show that *N*,*N*-dialkyl-*N*',*N*''-diarylguanidinato ligands can support metal complexes in a wide range of the oxidation states (+I, +III, and +IV).

The synthesis, characterization, and application of the rare well-defined high-valent Ir and Rh complexes found in the literature will be discussed in Chapter 2. In order to stabilize electron-deficient metal centers, proper selection of a ligand system is crucial. Therefore, a series of electron-rich monoanionic nitrogen-donor ligands will be discussed in this chapter. Among these ligands, dialkyldiarylguanidinato ligands, which have shown the exceptional ability to support metal center in high oxidation states, are the best candidates for approaching high-valent Ir and Rh complexes.

In Chapter 3, the preparation and characterization of Ir^{I} complexes bearing a dialkyldiarylguanidinato and two cyclooctene ligands will be discussed. The reaction with dioxygen displayed two-phase behavior. Although the blue intermediates, which formed in the first phase, were not defined, the analysis of the green products suggested that reorganization of the complexes occurred during the reaction. If the oxidation reaction was performed in the presence of excess guanidinato ligand, well-defined tris(guanidinato) Ir^{III} complexes could be observed, providing an opportunity to explore a rational synthesis.

The synthesis and characterization of mid- to high-valent iridium and rhodium complexes will be discussed in Chapters 4 and 5. The mid-valent tris(chelate) metal complexes were prepared from the reaction of M^{I} (M = Ir and Rh) cyclooctene complexes, described in Chapter 3, with O_2 in the presence of an excess of dialkyldiarylguanidinato ligands. In order to investigate the accessibility of high-valent

metal complexes, electrochemical methods are utilized. Subsequently, the chemical oxidation with mild oxidants showed that high-valent iridium and rhodium complexes can not only be observed in voltammograms, but also can be chemically generated. The single-crystal structure determination and EPR spectroscopy indicated that the products from the oxidation of Ir^{III} complexes are Ir^{IV} rather than Ir^{III} ligand-radical complexes. Although single crystals of the Rh^{IV} complexes could not be obtained due to their thermal instability, the spectroscopic methods showed that they are analogous to their Ir^{IV} counterparts and have higher redox potentials shown by the electrochemical studies.

The reactivity of the high-valent Ir^{IV} and Rh^{IV} complexes will be revealed in Chapter 6. The interconversion between The Ir^{III} and Ir^{IV} complexes is chemically reversible, and both can only be protonated at low pH (<1.4). The high-valent Ir and Rh complexes can oxidize substrates with O−H bonds. But substrates having C−H bond dissociation energies similar to those of the O−H bonds could not be oxidized.

The synthesis and characterization of two Fe^{II} complexs supported by tripodal tetradentate ligands will be briefly discussed in the Appendix. The ligands were designed and synthesized in a systematic manner, and their Fe^{II} complexs were characterized by UV−Vis, ^{1}H NMR, VT NMR spectroscopy, and X-ray crystallography. Finally, the generation and characterization of oxoiron(IV) complexes will also be discussed here.

CHAPTER 2

BACKGROUND

2.1 Introduction

The common oxidation states of iridium and rhodium in organometallic and coordination compounds are +I and +III, whereas compounds with Ir and Rh in high oxidation states, *i.e.* +IV and +V, are very rare. In the case of Ir, however, some intriguing reactivity is associated with high-valent intermediates. For example, complexes of Ir^{IV} and Ir^{V} have been proposed as key intermediates in C–H bond activation,[1-4] oxygen atom transfer reactions,[5] and water oxidation chemistry.[6-10] Simple complexes of Ir^{IV} are also known as strong one-electron oxidants.[11-14] The high reactivity and limited stability of high-valent Ir and Rh compounds often precludes their identification and characterization. One goal of the research presented herein is to gain access to more stable, well-defined complexes of Ir^{IV} and Rh^{IV} whose spectroscopic properties and structures can be investigated in detail. Another goal is to utilize the new complexes for a broader exploration of the chemistry of these high-valent metal centers.

The approach taken in this work involves strongly electron-releasing nitrogen-donor ligands that may stabilize metal centers in high oxidation states. Guanidinato ligands are well-known for their strongly electron-donating character in transition metal complexes but have previously not been used extensively as ligands for late transition metals. Here, tris(chelate) complexes of Ir^{III} and Rh^{III} with monoanionic *N*,*N*-dialkyl-*N*′,*N*″-diarylguanidinato ligands have been synthesized and employed as platforms for accessing the +IV oxidation state of these metal centers. These studies have led to the

stabilization and spectroscopic and crystallographic characterization of a series of Ir^{IV} and Rh^{IV} complexes.

This background chapter begins with an overview of high-valent Ir intermediates involved in the activation of inert molecules and atom transfer, followed by a summary of the synthesis and characterization of known organometallic and coordination compounds of Ir^{V}, Ir^{IV} and Rh^{IV}. Lastly, the electronic properties of guanidinato ligands in complexes of high-valent early transition metals are described.

2.2 High-valent Iridium and Rhodium

High-valent iridium has become an attractive target in recent years, mainly due to its role in C–H bond activation and oxygen atom transfer reactions.[1-5] The proposed mechanisms of C–H bond activation are shown in Scheme 1.[1] Two possible pathways were proposed: a) the reaction undergoes oxidative addition of R–H followed by reductive elimination of CH_4. The oxidation state of the Ir center changes throughout the reaction ($Ir^{III} \rightarrow Ir^{V} \rightarrow Ir^{III}$ in this mechanism); b) the reaction undergoes a concerted σ-bond metathesis without change of oxidation state of the Ir center. Although the oxidative addition/reductive elimination pathway has been suggested by the theoretical studies,[15] Ir^{V} species has always been proposed as the intermediates in this kind of reaction.[1]

In 2000, Tilley and Bergman *et. al.* discovered the experimental evidence, which the Ir^{V} complex was isolated, further supported an oxidative addition mechanism in C–H bond activation reactions.[2] The idea for the viability of the Ir^{III} to Ir^{V} C–H oxidative addition reaction was obtained by replacing the triflate (TfO^{-}) group with a less coordinating anion. This was accomplished by treating $[Ir(C_5Me_5)(PMe_3)(SiPh_2OTf)(Ph)]$ with $NaBAr_f$ (BAr_f = $\{B(3,5\text{-}(CF_3)_2C_6H_3)_4\}^{-}$) in an anion-exchange reaction, or

alternatively by reacting the more potent C–H bond activating complex $[Ir(C_5Me_5)(PMe_3)(Me)(CH_2Cl_2)]BAr_f$ with the tertiary silane $HSiPh_3$ (Scheme 2). These results offer the experimental support for an oxidative addition mechanism in C–H bond activation reactions through high-valent Ir (Scheme 1 pathway (a)).

Scheme 1. Possible Mechanisms of C–H Bond Activation Through High-valent Ir

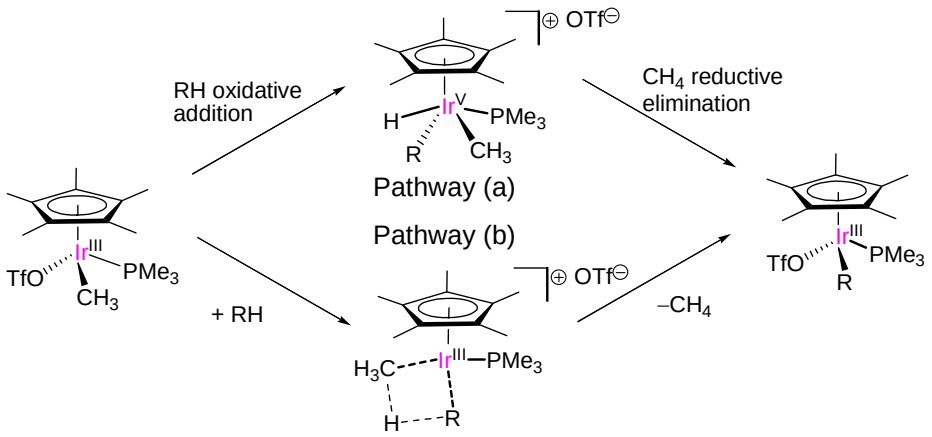

Scheme adapted from *Organometallics* **1999**, *18*, 2707.

Scheme 2. High-valent Ir in C–H Bond Activation

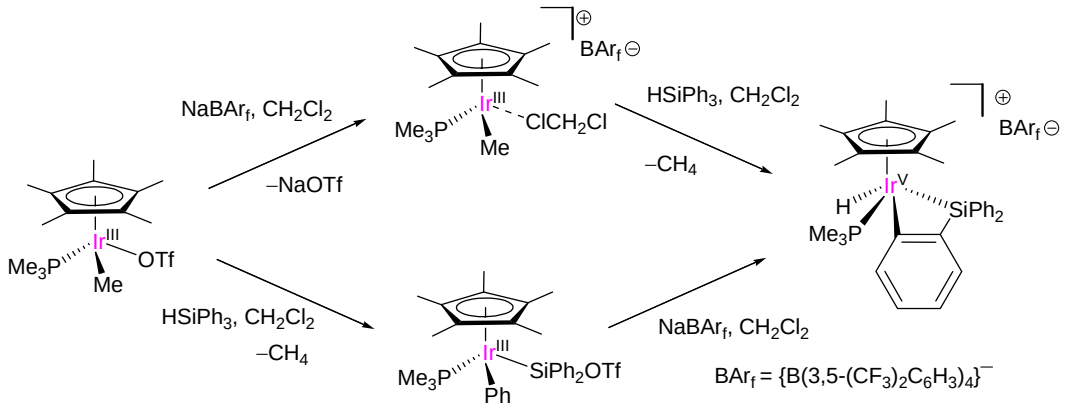

Scheme adapted from *J. Am. Chem. Soc*. **2000**, *122*, 1816.

Further evidence for the C–H bond activation came from isolable boryl Ir^{V} complexes, $[Ir(C_5Me_5)H_2X(BR_2)]$, (X = H or $BO_2C_2Me_4$) discovered by Hartwig *et. al.* in 2001.[3] The authors reported the generation and the isolation of a series of Ir^{V} boryl polyhydrides, which react regiospecifically with alkanes to produce functionalized products. The synthesis was carried out by thermolyzing $[Ir(C_5Me_5)H_4]$ with boranes to form boryl Ir^{V} complexes, which could functionalize C–H bonds of both alkanes and benzene. For example, 1-*n*-octyl-Bpin and C_6H_5Bpin (Bpin = boryl pinacolate) were produced from the reaction of $[Ir(C_5Me_5)H_3(BPin)]$ with octane and benzene, respectively (Scheme 3). The results demonstrate the property of the boryl group to induce C–H functionalization, and further reinforce the statement that high-valent Ir is involved in C–H bond activation.

Scheme 3. High-valent Ir in C–H Bond Activation

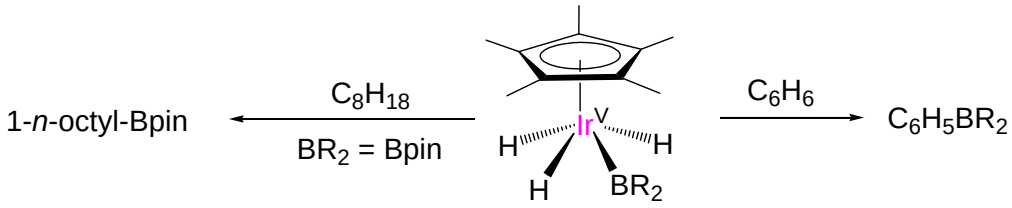

BR_2 = $BO_2C_2Me_4$ (Bpin); $BO_2C_6H_4$; $B(C_6H_{11})_2$.

Scheme adapted from *J. Am. Chem. Soc.* **2001**, *123*, 8422.

An interesting example of the chemical reaction through a proposed high-valent Ir intermediate was reported by Periana *et. al.* in 2007.[4] The cyclometalated Ir complex, $[Ir(NN)(NC)(CH_3)OTf]$ (NN = 4,4′-di-tert-butyl-2,2′-bipyridine-κ^2, NC = 6-phenyl-2,2′-bipyridine-κ^2, see Scheme 4), which reacts in a stoichiometric C–H activation reaction with benzene to generate the corresponding phenyl complex, as well as catalytic benzene C–H activation in the presence of acetic or trifluoroacetic acids. Most interestingly, this

compound also has been shown to undergo oxy-functionalization with oxidants such as $PhI(OAc)_2$ and $PhI\{OC(O)CF_3\}_2$ to generate CH_3X (X = AcO^-, $CF_3C(O)O^-$, TfO^-). The reaction could proceed via an Ir^V–R intermediate followed by reductive functionalization (Scheme 4). It should be noted that the high-valent Ir was proposed but not observed by authors in these reactions.

Scheme 4. High-valent Ir in C–H Bond Activation

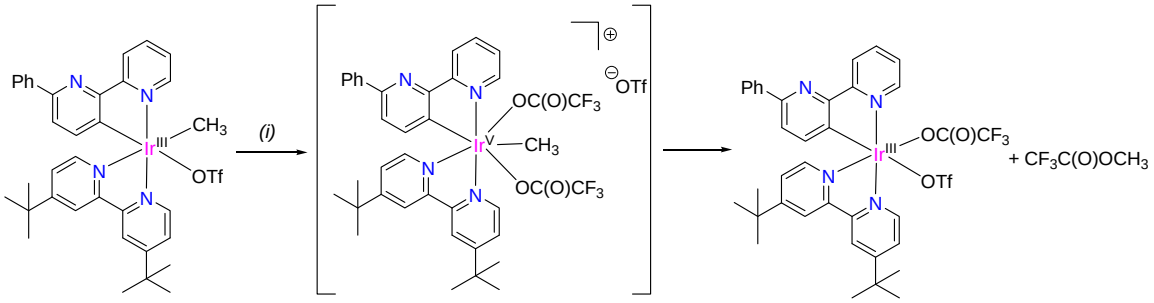

(i) $PhI(OC(O)CF_3)_2$.

Scheme adapted from *Organometallics* **2007**, *26*, 2137.

Oxygen atom transfer reactions play important roles in biological systems[16,17] and also synthetic oxidation chemistry.[18] High-valent Ir complexes could also serve as oxygen atom transfer agents.[5] For example, oxotrimesityliridium(V), $[IrO(mes)_3]$ (mes = 2,4,6-trimethylphenyl), could undergo degenerate oxygen atom transfer with trimesityliridium(III), $[Ir(mes)_3]$ (Scheme 5). In addition, oxotrimesityliridium(V) could also undergo oxygen atom transfer to organic substrates, *i.e.* formation of triphenylphosphine oxide from the reaction of $[IrO(mes)_3]$ with triphenylphosphine through oxygen atom transfer (Scheme 5).

Scheme 5. High-valent Ir in Oxygen Atom Transfer

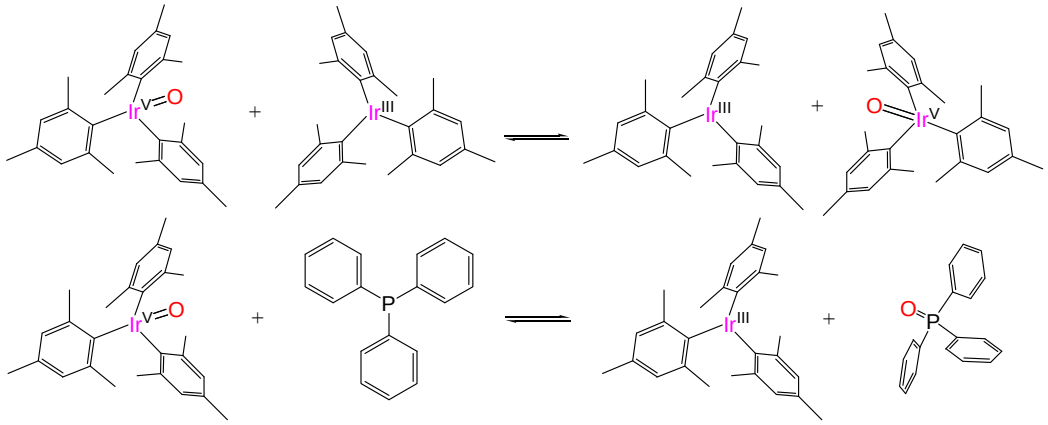

Stable complexes of Ir^{IV} have found applications as one-electron oxidants for synthetic purposes and in mechanistic studies,[11,12] whereas transient Ir^{IV} species are involved in oxidatively induced C–H bond cleavage.[13,14] More recently, an Ir^{IV} complex was proposed to be an intermediate in water oxidation chemistry.[6] A series of bis(aquo)iridium(III) complexes have been shown to robustly and efficiently catalyze the oxidation of water to dioxygen in the presence of a sacrificial oxidant, $(NH_4)_2[Ce^{IV}(NO_3)_6]$ (Scheme 6), through a proposed Ir^{IV} intermediate.

Scheme 6. High-valent Ir in Water Oxidation

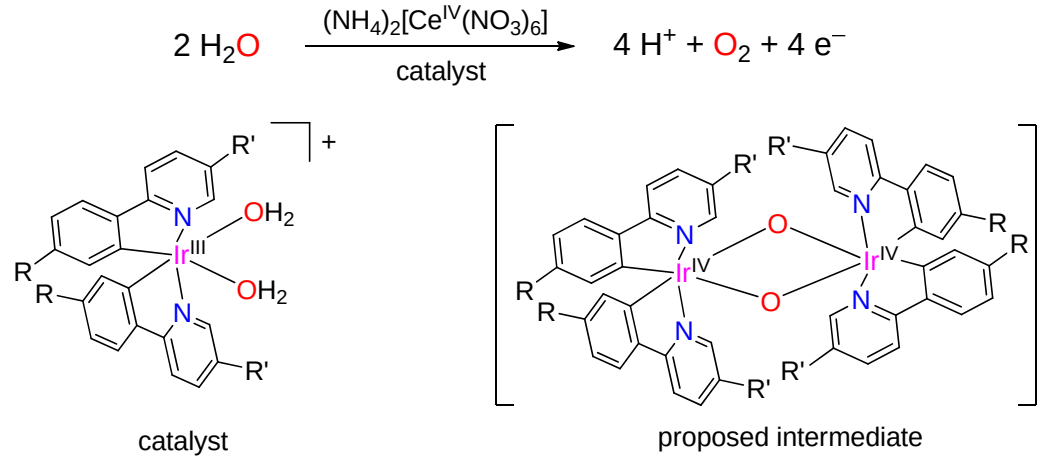

Despite these developments, well-defined examples of Ir in the +IV and +V oxidation state are still limited.[19,20] These include inorganic hexahalogeno complexes[21,22] and several organometallic compounds[5,23-27] with substituted phenyl or cyclopentadienyl ligands. The rare examples of crystallographically characterized Ir^{IV} complexes are shown in Scheme 7. The rarity of well-defined high-valent Ir complexes is due to their instable nature which results in difficulty in the synthesis and characterization of such complexes, especially when supported by organic ligands.

Scheme 7. Crystallographically Characterized Ir^{IV} Complexes

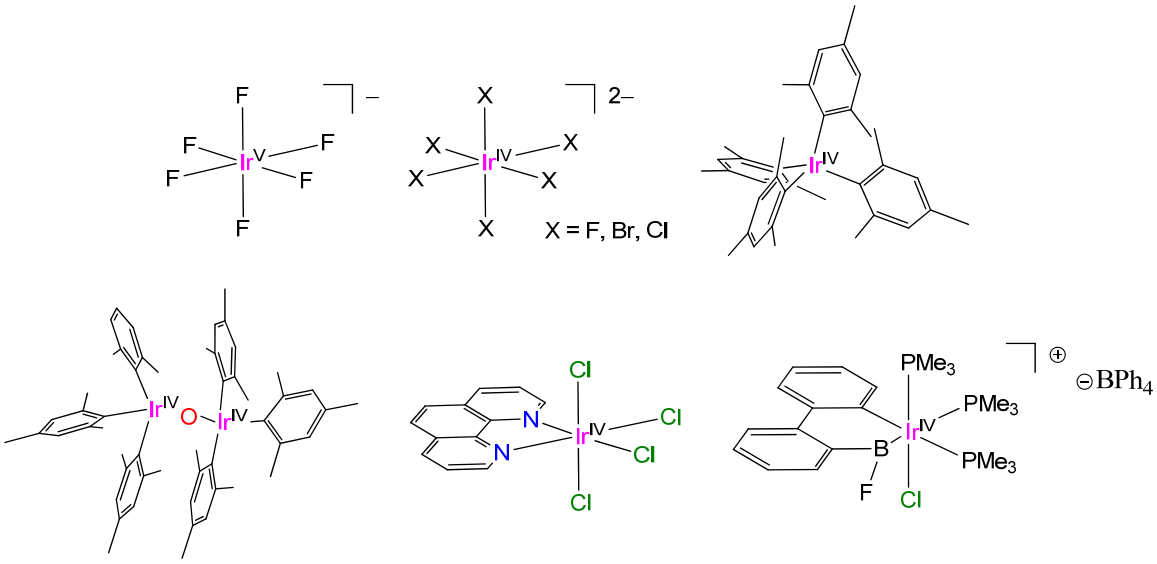

The following examples are the synthesis and characterization of existing high-valent Ir complexes. In 1965, the high-valent Ir^{V} compound, $[Ir^{V}H_5(PR_3)_3]$, was synthesized by treatment of $[Ir^{III}(PR_3)_3]Cl_3$ with $LiAlH_4$,[28] although it was initially assigned as mid-valent Ir complex, $[Ir^{III}H_3(PR_3)_3]$. However, reinvestigation of the ^{31}P and ^{1}H NMR spectra suggests that the previous trihydrido complexes was in fact high-valent pentahydrido ones.[29]

The first high-valent organoiridium(V) compound, $[(C_5Me_5)IrMe_4]$, was prepared from the reaction of $[\{Ir(C_5Me_5)Cl\}_2(\mu\text{-}Cl)_2]$ with Al_2Me_6 at −78 °C in the inert atmosphere following by oxidation with O_2 (from air). The product was characterized by ^{1}H NMR spectroscopy and mass spectrometry.[23]

The extensive studies of tetrahalogenoiridium(IV) complexes were reported in 1987.[32] Purple Ir^{IV} complexes $[IrL_2Cl_4]$ [L = pyridine (py), PEt_3, PEt_2Ph, $PEtPh_2$, $AsEt_3$, $AsMe_2Ph$, SMe_2, or $SeMe_2$] were synthesized by oxidation of the Ir^{III} anions $[IrL_2Cl_4]^-$ with chlorine. Dark green $[IrL_2Br_4]$ (L = py, PEt,, PMe,Ph, AsEt,, AsMe,Ph, or SMe,) were obtained similarly from $[IrL_2Br_4]^-$ and Br_2. The $[IrL_2Cl_4]$ (L = PPh_3, $AsPh_3$, or $SbPh_3$) were prepared directly from $IrCl_3{\cdot}nH_2O$ + 2L, followed by chlorination. The Ir^{IV} complexes have been characterized by IR, and UV−Vis spectroscopy and for the complex $[Ir(AsEt_3)_2Br_4]$ by X-ray diffraction. The redox potentials (0.21–0.70 V *vs.* $[FeCp_2]/[FeCp_2]^+$) were obtained by cyclic voltammetry.

Similar investigation from the same research group was explored in 1988.[33] The Ir^{IV} complexes *cis*-$[Ir(L\text{-}L)Cl_4]$ [L-L = $MeSCH_2CH_2SMe$, $MeSeCH_2CH_2SeMe$, 2,2'-bipyridyl (bipy), or 1,10-phenanthroline (phen)] have been prepared by oxidation of the corresponding Ir^{III} anions *cis*-$[Ir(L\text{-}L)Cl_4]^-$ with Cl_2. These complexes were characterized by IR, UV−Vis, NMR (^{31}P, ^{77}Se, and ^{125}Te) spectroscopy, and, for the complex $[Ir(phen)Cl_2]$, by X-ray diffraction. Electrochemical studies show that $[Ir(L\text{-}L)Cl_4]^-/[Ir(L\text{-}L)Cl_4]$ redox couple for all complexes is nearly reversible and the redox potentials of Ir^{III} complexes range from 0.88 to 1.22 V *vs.* $[FeCp_2]/[FeCp_2]^+$ which are more positive than those of *trans*-$[IrL_2Cl_4]$ analogues.

Neutral homoleptic organoiridium(IV) compound, $[Ir(mes)_4]$, was synthesized from the reaction of anhydrous $IrCl_3$ with four-fold of mesityllithium at room temperature.[25] The solid-state structure showed a distorted tetrahedral geometry, and the EPR spectrum at 77 K agrees with tetrahedral low-spin d^5 Ir complex with $g_{\|}$ = 2.437 and $g_{\perp}$ = 2.005. In addition, two, one-electron reversible waves were observed at −0.44 and

–1.12 V *vs.* $[FeCp_2]/[FeCp_2]^+$ in cyclic voltammetry. Chemical oxidation of the this compound was carried out by using AgOTf or $NOPF_6$ to generate diamagnetic tetrahedral Ir^V complexes $[Ir(mes)_4]OTf$ or $[Ir(mes)_4]PF_6$ from the same research group,[26] and $[Ir(mes)_4]OTf$ was characterized by ^1H NMR and X-ray diffraction spectroscopy.

Another example of isolable Ir^{IV} complex was prepared by C–C bond cleavage of biphenylene with $[Ir(cod)Cl_2]_2$ (cod = 1,5-cyclooctadiene), replacement of cod by PMe_3, and insertion of the BF group on an Ir–C bond of the metallocycle (Scheme 8).[27] It is worth noting that the complex $[Ir(PMe_3)_3(biph)Cl]$ can be oxidized quasi-reversibly to form an Ir^{IV} species $[Ir(PMe_3)_3(biph)Cl]^+$, which can be obtained by bulk electrolysis, but cannot be isolated as a crystalline form. Oxidation with $NOBF_4$ gives the unusual Ir^{IV} boryl compound $[Ir(PMe_3)_3(biphBF)Cl]^+$, which has been isolated and structurally characterized. The EPR spectroscopic data (g = 2.15 and 1.96) confirmed that the oxidation is metal-centered.

Scheme 8. Synthesis of boryl Ir^{IV} complex

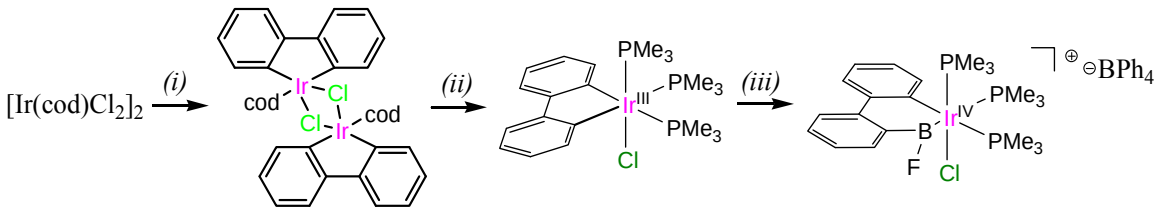

*(i)*Biphenyl, $C_{12}H_{10}$; *(ii)* 2 PMe_3; *(iii)* $NOBF_4$. $NaBPh_4$

For a broader exploration of the chemistry of Ir^{IV}, however, the availability of complexes with multidentate ligands based on organic heteroatom-donor frameworks would be of great advantage, as has been the case for other high-valent transition metal centers.[30,31] Although a series of stable complexes of the type $[Ir^{IV}X_4L_2]$; where X = Cl,

Br and L = N-, P-, or S-donor ligand; were described two decades ago, the corresponding complexes with more than two heteroatom donors could not be obtained.[32,33] Nevertheless, electrochemical studies of Ir^{III} complexes of phenylpyridine-derived [34,35] and corrolato ligands[36-38], $E_{1/2}$ = 0.07–0.91 V and 0.2 V *vs.* $[FeCp_2]/[FeCp_2]^+$, respectively, suggest that high-valent analogues may be within reach by proper design of coordinated ligands.

Moving up the periodic table from the third to second row, metal complexes with high oxidation state become even more difficult to achieve. Therefore, compounds containing rhodium in the +IV and +V oxidation state are more scarce. Although several organometallic rhodium(IV) compounds also have been reported,[39] some of the high-valent Rh complexes are proved to be misinterpreted. For example, one class of these complexes, the mononuclear or binuclear superoxorhodium(III) ions was initially misinterpreted as Rh^{IV} containing compounds, Claus Blue, resulted from the oxidation of Rh^{III}.[40] There are only a few cases of well-defined Rh^{IV} complexes described in the literatures (Scheme 9).[41-45] Unlike octahedral $[IrX_6]^{2-}$, where X = F, Br, Cl; only fluoride analogue for rhodium(IV) exists.

Scheme 9. Well-defined Rh^{IV} Complexes

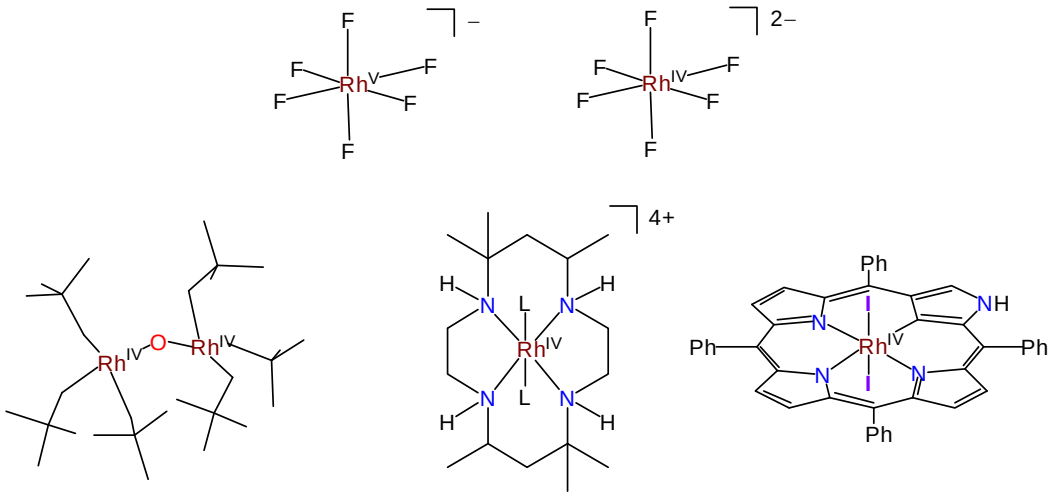

The diamagnetic dirhodium(IV) compound [{Rh(Me_3CCH_2)}$_2$(μ-O)] was synthesized by reaction of neopentyllithium or neopentylmagnesium bromide with $RhCl_3(THT)_3$ (THT = tetrahydrothiophen) in the presence of a source of oxygen atoms (O_2 or Me_3NO).[43] The ^1H and ^{13}C NMR spectra of this compound exhibit only neopentyl resonances, and ν_{RhO} was observed at 802 cm^{-1} in the IR spectrum. Moreover, the solid-state structure of the product was confirmed by X-ray diffraction.

The synthesis of N-confused tetraphenylporphyrin (NCTPP) rhodium(IV) complex was carried out by reaction of dirhodium(I) complex with iodine (Scheme 10).[45] The product was characterized by UV–Vis, ESIMS, EPR and X-ray diffraction spectroscopy.

Therefore, as shown in the Scheme 9, nitrogen-donor-based ligands should be suitable for stabilization of Rh^{IV} complexes.

Scheme 10. Synthesis of $[Rh^{IV}(NCTPP)]I_2$

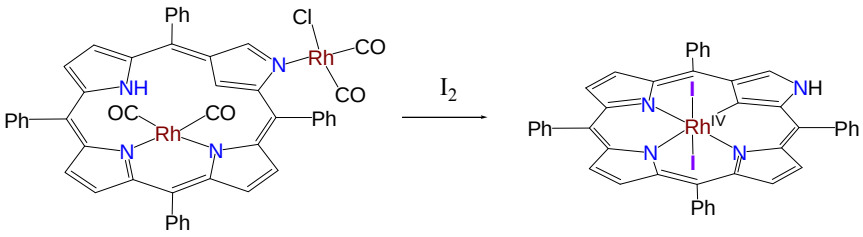

NCTPP = N-confused tetraphenylporphyrin

2.3 Mono-anionic Nitrogen Donor Ligands

Studies involving mid- to late-transition metal complexes of nitrogen donor ligands range from classical coordination chemistry to the application fields. Among all

the types of N donor ligand systems, monoanionic nitrogen-donor ligands represent an important class of supporting ligands and have been widely used in the coordination chemistry of transition metals to impart diverse properties and reactivity. Prominent examples include poly(1-pyrazolyl)borate,[46,47] β-diiminate,[48] aminotroponiminate,[49] amidinate[50,51] and triazenide[52] scaffolds (Scheme 11).

Scheme 11. Monoanionic Nitrogen-donor Ligands

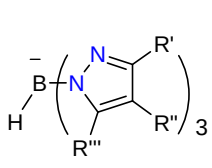

poly(1-pyrazolyl)borate

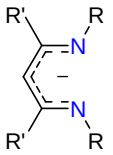

β-diiminate

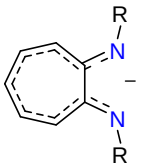

aminotroponiminate

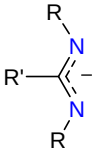

amidinate

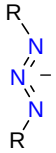

triazenide

Since guanidinates are conceptually related to the latter two systems, they may be expected to be similarly well-suited as supports for reactive metal centers. Complexes of guanidinates are known for many metals and metalloids, in particular, for early transition metals and lanthanides in mid- to high-valent oxidation states (Scheme 12).[53-59] For Ir and Rh, there are only a few complexes of these metal centers bearing guanidinato ligands have been reported. For example, $[Ir(H)_2\{PhNC(NHPh)NPh\}(PPh_3)_2]$,[60] $[Ir\{(^{i}Pr)NC(NMe_2)N(^{i}Pr)\}(cod)]$,[61] $[Rh\{(2,6\text{-}^{i}Pr_2C_6H_3)NC(NR_2)N(2,6\text{-}^{i}Pr_2C_6H_3)\}(cod)]$,[94] where R = isopropyl or cyclohexyl. The stabilization of high-valent metal complexes can be attributed to lone-pair donation from the nitrogen atom of the NR_2 group, which increases the electron density at the two donor atoms available for metal coordination and, thereby, makes this class of ligands stronger donors than the closely related ligands (Scheme 13). Thus, in resonance form I and III, the ligand is closely related to the amidinate form bearing an amino-substituent on the central carbon atom. Amidinates are themselves an electronically flexible ligand system displaying compatibility with

transition metals in a range of oxidation states.[63] However, the potential for a contribution from the iminium/diamide type resonance form II means that this flexibility is exceeded by guanidinates whose π-donor ability, and hence compatibility with electron-deficient metal ions, is augmented by any contribution from this resonance form. Guanidinates are therefore stronger donors (more basic) than amidinates. For a given metal, replacement of an amidinate by a guanidinate would be expected to increase the electron density on the metal and reduce its oxidation potential, *e.g.* $[Mo^{II}_2(\mu\text{-L})_4]$ (L = PhNC(NHPh)NPh or (4-MeC_6H_4)NC(H)N(4-MeC_6H_4),[87,88] and, thereby, makes this class of ligands stronger donors than the closely related amidinate and triazenide anions (Scheme 14).

Scheme 12. Structures of High-Valent Metal Complexes Supported by Guanidinato Ligands

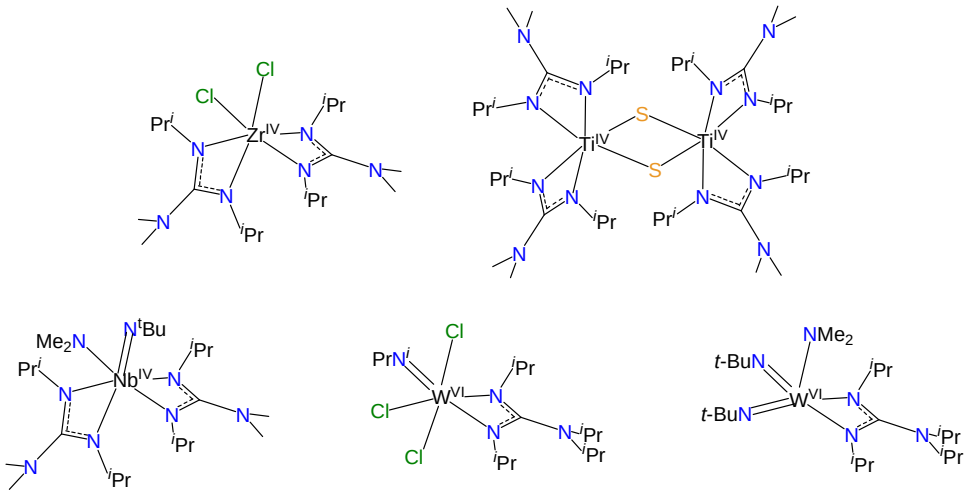

Scheme 13. Resonance Structures of the Guanidinate Monoanion

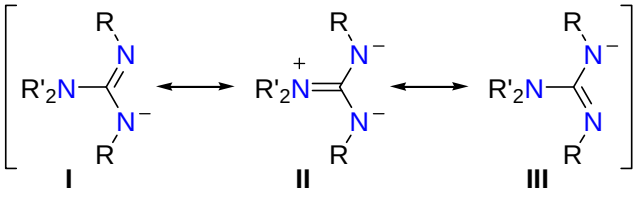

Scheme 14. Guanidinate, Amidinate, and Triazenide Anions

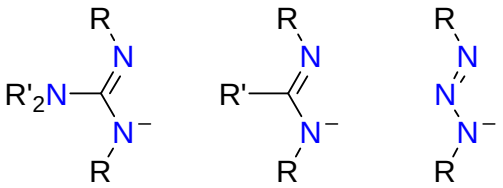

2.4 Conclusion

High-valent Ir and Rh complexes are capable of performing a variety of applications in chemistry. Because stable well-defined complexes of Ir and Rh in high oxidation states, *e.g.* +IV and +V, are very rare, systematic design and synthesis of such compounds will not only help us understand their spectroscopic and structural properties but also elucidate many reaction mechanisms, in which high-valent Ir and Rh species have been involved. The proper selection and design of supporting ligands is important to further develop this area of research. Intrigued by the reports which show the exceptional ability for stabilization of high-valent metal complexes by guanidinato ligands,[53-59] we decided to take advantage of the strongly electron-releasing character of *N*,*N*-dialkyl-*N*′,*N*″-diarylguanidinato ligands, $\{ArNC(NR_2)NAr\}^-$,[64] and to investigate their potential for the stabilization of high-valent iridium and rhodium (Chapter 4, 5, and 6).

CHAPTER 3

IRIDIUM(I) COMPLEXES SUPPORTED BY *N,N*-DIALKYL- *N′,N″*-DIARYLGUANIDINATO(1−) LIGANDS

3.1 Introduction

In this Chapter, the synthesis and characterization of Ir^{I} complexes of the strongly electron-donating *N,N*-dialkyl-*N′,N″*-dialkyldiarylguanidinato(1−) ligands will be described. The synthesis and characterization of the ligands **1a–c** and Ir^{I} complex [Ir{PhNC(NMe_2)NPh}$(coe)_2$] **2a** (coe = *cis*-cyclooctene) was published by our research group in 2008.[64] Two methods have been utilized for the synthesis of the neutral guanidines, and the corresponding lithium guanidinate salts were prepared by reacting methyllithium with free guanidines. Iridium(I) complexes supported by guanidinato ligands were synthesized by transmetallation of the lithium salts with [{Ir$(coe)_2$}$_2$(μ-Cl)$_2$], and characterized by nuclear magnetic resonance (NMR) spectroscopy, electron impact mass spectrometry (EIMS), and elemental analysis.

As determined by spectroscopic methods and single-crystal structure determination, the guanidinato(1−) ligands coordinate the low-valent d^8 Ir^{I} center in an *N,N′*-chelating binding mode. The bond lengths and angles of the intra-ligand structural features [Ir{PhNC(NMe_2)NPh}$(coe)_2$] show a significant contribution of the iminium/diamide resonance structure.

Complexes **2a–c** are air-sensitive and react readily with dioxygen and form an unstable blue intermediate. ESI(+)MS analysis of the intermediate and final product indicates formation of dinuclear Ir complexes and a bis(guanidinato) Ir complex. In addition, for **2a**, a trace amount of a tris(chelate) Ir^{III} complex was also observed by EIMS. Although these products could be observed by mass spectrometry, attempts to

isolate them were unsuccessful. However, when excess of the lithium guanidinate salt is present in solution, tris(guanidinato)iridium(III) complexes could be isolated. This result gives us valuable information for preparing and characterizing well-defined Ir^{III} and Rh^{III} complexes (Chapter 4, 5, and 6).

3.2 Experimental Section

Materials and General Procedures. All reagents and solvents were purchased from commercial sources and were used as received, unless noted otherwise. Diethyl ether, tetrahydrofuran, and toluene were deoxygenated by sparging with N_2 and purified by passage through two packed columns of molecular sieves under an N_2 pressure (MBraun solvent purification system). *n*-Pentane was dried over Na and distilled under N_2 prior to use.[65] Preparation and handling of air- and moisture-sensitive materials were carried out under an inert gas atmosphere by using either standard Schlenk and vacuum line techniques or a glovebox. Dioxygen was dried by passage through a short column of Drierite. Isotope-enriched $^{18}O_2$ (97% ^{18}O) was purchased from Cambridge Isotope Laboratories, Andover, MA, USA. $[\{Ir(coe)_2\}_2(\mu\text{-}Cl)_2]$ was synthesized according to a published procedure (coe = *cis*-cyclooctene).[66] Elemental analyses were performed by Atlantic Microlab, Inc., Norcross, GA, USA.

NMR spectra were recorded on a Bruker Avance MicroBay 300 or Avance DPX 300 spectrometer at ambient temperature. ^1H and ^{13}C chemical shifts are reported in parts per million (ppm) and were referenced to residual solvent peaks. Mass spectral data were acquired on a quadrupole ion trap ThermoFinnigan LCQ Deca mass spectrometer using an electrospray ionization source or on a single quadrupole ThermoFinnigan Voyager mass spectrometer using an electron impact ionization source (equipped with a solids probe). UV–Visible spectra were recorded on an HP 8453A diode array

spectrophotometer (Agilent Technologies) with samples maintained at low temperature using a cryostat from Unisoku Scientific Instruments, Japan.

***N*,*N*-Dimethyl-*N′*,*N″*-diphenylguanidine, PhN=C(NMe$_2$)NHPh (1a).** A total of 9.0 mL of a dimethylamine solution (2.0 M in THF; 18 mmol) was added to a solution of 2.01 g (8.80 mmol) of *N*,*N′*-diphenylthiourea in 15 mL of tetrahydrofuran at 0 °C. Over a period of 15 min, 2.73 g (8.77 mmol) of benzyltriethylammoniun permanganate[67] was added to the solution under stirring, resulting in the formation of a brown precipitate, and the mixture was stirred for an additional 15 min. The precipitate was separated by filtration through a celite pad and washed with tetrahydrofuran. The volatiles of the combined filtrates were removed under reduced pressure to afford a yellow oil. The guanidine was extracted from the oil with 30 mL of diethyl ether and, after evaporation of the solvent, isolated as a colorless powder. The product was recrystallized from hot hexanes and dried *in vacuo*. Yield: 1.49 g (71%). Anal. Calcd for $C_{15}H_{17}N_3$: C, 75.28; H, 7.16; N, 17.56. Found: C, 75.29; H, 7.06; N, 17.59. ^{1}H NMR (300 MHz, $CDCl_3$, δ): 7.25 (t, J = 7.5 Hz, 4H, Ar H), 6.99 (t, J = 7.4 Hz, 2H, Ar H), 6.86 (d, J = 8.5 Hz, 4H, Ar H), 5.5 (br s, 1H, NH), 2.91 (s, 6H, NCH_3). $^{13}C\{^1H\}$ NMR (75.5 MHz, $CDCl_3$, δ): 151.4, 129.2, 121.9, and 120.1 (Ar), 38.1 (NCH_3). EIMS (70 eV) m/z: $M^{+\bullet}$ calcd for $C_{15}H_{17}N_3$, 239.14; found, 239.1.

***N*,*N*-Diethyl-*N′*,*N″*-diphenylguanidine, PhN=C(NEt$_2$)NHPh (1b).** A total of 1.51 mL of diethylamine (1.07 g, 14.6 mmol) was added to a solution of 1.62 g (7.10 mmol) of *N*,*N′*-diphenylthiourea in 15 mL of tetrahydrofuran at 0 °C. Over a period of 15 min, 2.23 g (7.16 mmol) of benzyltriethylammoniun permanganate was added to the solution under stirring, resulting in the formation of a brown precipitate, and the mixture was stirred for an additional 15 min. The precipitate was separated by filtration through a celite pad and washed with tetrahydrofuran. The volatiles of the combined filtrates were removed under reduced pressure to afford a yellow oil. The guanidine was extracted from the oil with diethyl ether (2 x 50 mL) and, after evaporation of the solvent, isolated as a

colorless powder. The product was recrystallized from hot hexanes and dried *in vacuo*. Yield: 1.52 g (80%). Anal. Calcd for $C_{17}H_{21}N_3$: C, 76.37; H, 7.92; N, 15.72. Found: C, 76.07; H, 7.79; N, 15.66. ^{1}H NMR (300 MHz, $CDCl_3$, δ): 7.12 (t, J = 8.0 Hz, 4H, Ar H), 6.86–6.77 (m, 6H, Ar H), 5.31 (br s, 1H, NH), 3.23 (q, J = 7.1 Hz, 4H, NCH_2CH$_3$), 1.07 (t, J = 7.1 Hz, 6H, NCH$_2$CH_3). ^{13}C{^{1}H} NMR (75.5 MHz, $CDCl_3$, δ): 150.0, 129.1, 121.8, and 118.3 (Ar), 41.9 (N*C*H$_2$CH$_3$), 12.8 (NCH$_2$*C*H$_3$). EIMS (70 eV) *m*/*z*: $M^{+\bullet}$ calcd for $C_{17}H_{21}N_3$, 267.17; found, 267.0.

***N*,*N*-Dimethyl-*N*′,*N*″-bis(4-methylphenyl)guanidine, (4-MeC$_6$H$_4$)N=C(NMe$_2$)-NH(4-MeC$_6$H$_4$) (1c).** The procedure for the synthesis of the corresponding guanidinium iodide was adapted from a method previously described for other guanidinium iodides.[68] A solution of 0.50 g (1.95 mmol) of *N*,*N*′-bis(4-methylphenyl)thiourea and 1.22 mL (2.78 g, 19.5 mmol) of iodomethane in 12 mL of methanol was heated under reflux for 2 h. After the solution was cooled to room temperature, the volatiles, including unconsumed iodomethane, were removed under reduced pressure, affording *S*-methyl-*N*,*N*′- bis(4-methylphenyl)-isothiourea hydroiodide in quantitative yield (0.78 g). To a solution of this product in 5 mL of methanol was added 1.06 mL of a dimethylamine solution (5.6 M in EtOH; 5.94 mmol). The resulting solution was heated in a sealed flask for 7 h at 70 °C. (*Caution:* Due to the formation of methanethiol, which is a gas under the reaction conditions, the pressure in the flask may increase substantially. A shield should be used for protection.) The solution was then cooled to room temperature, and methanethiol was carefully removed in a stream of N_2. (MeSH was trapped by routing the gas stream through concentrated HNO_3.) Upon evaporation of the solvents, *N*,*N*-dimethyl-*N*′,*N*″-bis(4-methylphenyl)guanidinium iodide was obtained as a colorless solid (0.73 g).

This salt was dissolved in 20 mL of diethyl ether and treated with 50 mL of a saturated aqueous Na_2CO_3 solution. The biphasic mixture was vigorously stirred for 1 h, before the organic phase was separated and dried over $MgSO_4$ and the volatiles were removed under reduced pressure. The crude product was purified by column

chromatography on silica gel using a solution of 1% NEt_3 in diethyl ether as the eluent. Yield: 0.34 g (65%). Alternatively, the product could be recrystallized from hot hexanes and dried *in vacuo*. Anal. Calcd for $C_{17}H_{21}N_3$: C, 76.37; H, 7.92; N, 15.72. Found: C, 76.53; H, 8.07; N, 15.74. ^{1}H NMR (300 MHz, $CDCl_3$, δ): 7.05 (d, J = 8.4 Hz, 4H, Ar H), 6.79 (d, J = 8.4 Hz, 4H, Ar H), 5.44 (br, 1H, NH), 2.89 (s, 6H, NCH_3), 2.29 (s, 6H, $C_6H_4CH_3$). ^{13}C{^{1}H} NMR (75.5 MHz, $CDCl_3$, δ): 152.1, 131.4, 129.9, and 120.5 (Ar), 38.2 (NCH_3), 20.8 ($C_6H_4CH_3$). EIMS (70 eV) m/z: $M^{+\bullet}$ calcd for $C_{17}H_{21}N_3$, 267.17; found, 267.3.

General Procedure for the Synthesis of [Ir{ArNC(NR$_2$)NAr}(coe)$_2$]. In an N_2 atmosphere, a solution of 0.30 mmol of lithium guanidinate in 10 mL of diethyl ether was added to a suspension of 134 mg (0.150 mmol) of $[\{Ir(coe)_2\}_2(\mu\text{-}Cl)_2]$ in 5 mL of diethyl ether under stirring at 20 °C. The resulting solution was stirred for 3 h, during which its color slowly turned orange and a colorless precipitate formed. After filtration of the solution, the solvent was removed under reduced pressure. The residue was recrystallized from *n*-pentane by preparing a concentrated solution at 20 °C and storing it at –30 °C. Orange single crystals of X-ray diffraction quality were obtained within a day.

[Ir{PhNC(NMe$_2$)NPh}(coe)$_2$] (2a). Yield: 135 mg (69%). Anal. Calcd for $C_{31}H_{44}IrN_3$: C, 57.20; H, 6.81; N, 6.46. Found: C, 57.15; H, 6.80; N, 6.32. ^{1}H NMR (300 MHz, $CDCl_3$, δ): 7.20 (t, J = 7.8 Hz, 4H, Ar H), 6.95 (m, 6H, Ar H), 3.20 (br, 2H, =C*H*CH$_2$–), 2.57 (br, 2H, =C*H*CH$_2$–), 2.23 (s, 6H, NCH_3), 1.86–0.96 (m, 24H, =CHC*H*$_2$–). ^{13}C{^{1}H} NMR (75.5 MHz, $CDCl_3$, δ): 177.9 (CN_3), 148.5, 145.3, 128.5, 128.2, 127.7, 123.8, 123.4, and 122.3 (Ar), 54.2 and 50.0 (=*C*HCH$_2$–), 39.5 (NCH_3), 30.5, 28.9, 26.3, and 26.1 (=CH*C*H$_2$–). EIMS (70 eV) m/z: $M^{+\bullet}$ calcd for $C_{31}H_{44}IrN_3$, 651.32; found, 651.3. UV–Vis (toluene) λ_{max}, nm (ε): 385 (1000), 433 (900), 480 (sh, 300).

[Ir{PhNC(NEt$_2$)NPh}(coe)$_2$] (2b). Yield: 153 mg (75%). Anal. Calcd for $C_{33}H_{48}IrN_3$: C, 58.38; H, 7.13; N, 6.19. Found: C, 58.35; H, 7.13; N, 6.09. ^{1}H NMR (300 MHz, $CDCl_3$, δ): 7.21 (t, J = 7.8 Hz, 4H, Ar H), 6.96 (m, 6H, Ar H), 3.18 (br, 2H,

=C*H*CH_2–), 2.57 (m, 6H, =C*H*CH_2– and NC*H*$_2$$CH_3$), 1.86–0.96 (m, 24H, =CHC*H*$_2$–), 0.89 (t, *J* = 7.1 Hz, 6H, NCH_2C*H*$_3$). EIMS (70 eV) *m*/*z*: $M^{+\bullet}$ calcd for $C_{33}H_{48}IrN_3$, 679.35; found, 679.5. UV–Vis (toluene) λ_{max}, nm (ε): 384 (1000), 430 (900), 485 (sh, 330).

[Ir{(4-MeC_6H_4)N=C(NMe_2)NH(4-MeC_6H_4)}(coe)$_2$] (2c). Yield: 149 mg (73%). Anal. Calcd for $C_{33}H_{48}IrN_3$: C, 58.38; H, 7.13; N, 6.19. Found: C, 58.26; H, 6.97; N, 6.20. ^{1}H NMR (300 MHz, $CDCl_3$, δ): 7.03 (d, *J* = 8.0 Hz, 4H, Ar H), 6.90 (m, 4H, Ar H), 3.16 (br, 2H, =C*H*CH_2–), 2.51 (br, 2H, =C*H*CH_2–), 2.29 (s, 6H, NCH_3), 2.20 (s, 6H, $ArCH_3$),1.90–0.80 (m, 24H, =CHC*H*$_2$–). EIMS (70 eV) *m*/*z*: $M^{+\bullet}$ calcd for $C_{33}H_{48}IrN_3$, 679.35; found, 679.4. UV–Vis (toluene) λ_{max}, nm (ε): 385 (900), 430 (800), 490 (sh, 300).

Reactions of [Ir{ArNC(NR_2)NAr}(coe)$_2$] Complexes with O_2. A 1.25 mM solution of the [Ir{ArNC(NR_2)NAr}(coe)$_2$] complex ($1.25 \cdot 10^{-3}$ mmol) in 1 mL of toluene was placed in a 0.5-cm UV–Vis cuvette, precooled to –40 °C and purged with O_2 (15 s). The reactions were monitored by UV–Vis spectroscopy. The solutions of an intermediate and the decay product(s) were subjected to ESI and EI mass spectrometry. ESI(+)MS for **2a** + O_2 (*m*/*z*): 240.1, 667.1, 892.8, 1131.0. For the labeling experiment, 2 mL (~44 mmol) of $^{18}O_2$ (97% ^{18}O) was added to a solution of $1.25 \cdot 10^{-3}$ mmol of **2a** in 1 mL of toluene. ESI(+)MS for **2a** + $^{18}O_2$ (*m*/*z*): 240.1, 667.2, 894.9, 1135.2. ESI(+)MS for **2b** + O_2 (*m*/*z*): 268.2, 723.3, 949.1. ESI(+)MS for **2c** + O_2 (*m*/*z*): 268.1, 723.1. For each reaction, the observed peaks can be assigned to the following ions (LH = guanidine, ArN=C(NR_2)NHAr): $\{LH + H\}^+$, $\{Ir(L)_2 - 2H\}^+$, $\{Ir_2(L)_2(O)(OH)\}^+$, and $\{Ir_2(L)_3(O)(OH)\}^+$. EIMS for **2a** + O_2 (*m*/*z*): 907.4, $\{Ir(L)_3\}^{+\bullet}$.

X-ray Crystallographic Analysis. A single crystal **2a** was coated with Paratone N oil and mounted on a glass capillary for data collection at 150(2) K on a Nonius KappaCCD diffractometer using Mo *Kα* radiation (graphite monochromator). The temperature was controlled by an Oxford Cryostream Cooler (700 series, N_2 gas). Data collection, data reduction, and absorption correction were carried out following standard

CCD techniques using the software packages Collect and HKL-2000.[69,70] Final cell constants were calculated from 12448 reflections from the complete data set. The space group $P2_1/c$ was determined based on systematic absences and intensity statistics. The structure was solved by direct methods and refined by full-matrix least-squares minimization and difference Fourier methods (SHELXTL v.6.12).[71,72] All non-hydrogen atoms were refined with anisotropic displacement parameters. All hydrogen atoms were placed in ideal positions and refined as riding atoms with relative isotropic displacement parameters, with the exception of the alkene hydrogen atoms (=C*H*), which were located in the difference Fourier map and refined with a restrained C–H distance (1.00 Å) and relative isotropic displacement parameters (1.2 times the equivalent isotropic value of the bonded carbon atom). The final full-matrix least-squares refinement converged to $R1$ = 0.0339 and $wR2$ = 0.0526 (F^2, all data). Table 1 contains additional crystal and refinement information. Selected distances and angles are summarized in Tables 2 and 3.

3.3 Results and Discussion

3.3.1 Synthesis and Characterization of Ligands and Ir^I Complexes

The guanidines PhN=C(NMe_2)NHPh (**1a**),[73,74] PhN=C(NEt_2)NHPh (**1b**),[74-76] and (4-MeC_6H_4)N=C(NMe_2)NH(4-MeC_6H_4) (**1c**)[73] were briefly mentioned in the literature but were only sparsely characterized. In this study, two different methods were utilized for the synthesis of the four neutral guanidines and complete characterization is included. The neutral ligands were synthesized from the corresponding thioureas, ArHNC(S)NHAr, and the appropriate amines, HNR_2, according to literature methods for related compounds (Scheme 15).[68,75]

Table 1. Crystallographic data and structure refinement for [Ir{PhNC(NMe$_2$)NPh}(coe)$_2$], **2a**.

Empirical formula	$C_{31}H_{44}IrN_3$
Formula weight	650.89
Crystal habit, color	plate, orange
Crystal size	0.18 x 0.17 x 0.06 mm^3
Temperature, T	150(2) K
Wavelength, λ	0.71073 Å
Crystal system	monoclinic
Space group	$P2_1/c$
Unit cell dimensions	a = 10.1479(11) Å
	b = 24.521(3) Å
	c = 11.5504(13) Å
	β = 101.896(5)°
Volume, V	2812.4(6) Å^3
Z	4
Calculated density	1.537 Mg·m^{-3}
Absorption coefficient, μ	4.771 mm^{-1}
F(000)	1312
θ range for data collection	2.64 to 27.48°
Limiting indices	$-12 \le h \le 13$, $-31 \le k \le 31$, $-14 \le l \le 14$
Reflections collected / unique	22691 / 6430 [R(int) = 0.0342]
Completeness to θ	99.8% (θ = 27.48°)
Max. and min. transmission	0.7628 and 0.4805
Refinement method	Full-matrix least-squares on F^2
Data / restraints / parameters	6429 / 0 / 334
Goodness-of-fit on F^2	1.071
Final R indices [I>2sigma(I)]	R1 = 0.0240, wR2 = 0.0494
R indices (all data)	R1 = 0.0339, wR2 = 0.0526
Largest diff. peak and hole	1.930 and –1.367 e·Å^{-3}

Table 2. Selected interatomic distances (Å) and angles (°) for [Ir{PhNC(NMe_2)NPh}($coe)_2$], **2a**.[a]

Distances (Å)		Angles (°)	
Ir–N1	2.122(3)	N2–Ir–N1	63.12(10)
Ir–N2	2.118(3)	N1–Ir–C16	105.98(12)
Ir–C16	2.129(3)	N1–Ir–C17	98.12(12)
Ir–C17	2.137(3)	N1–Ir–C24	155.84(12)
Ir–C24	2.126(3)	N1–Ir–C25	156.98(12)
Ir–C25	2.135(3)	N2–Ir–C24	106.42(11)
		N2–Ir–C25	99.37(12)
N1–C1	1.347(4)	N2–Ir–C16	157.19(12)
N1–C2	1.427(4)	N2–Ir–C17	155.06(12)
N2–C1	1.335(4)		
N2–C8	1.423(4)	C16–Ir–C17	38.81(13)
N3–C1	1.361(4)	C24–Ir–C25	38.91(12)
N3–C14	1.457(5)	C24–Ir–C16	90.82(13)
N3–C15	1.450(5)	C16–Ir–C25	84.56(13)
C16–C17	1.417(5)	C24–Ir–C17	84.02(12)
C24–C25	1.419(5)	C25–Ir–C17	102.57(13)
		C1–N1–C2	119.5(3)
		C1–N1–Ir	92.30(18)
		C2–N1–Ir	134.5(2)
		C1–N2–C8	121.4(3)
		C1–N2–Ir	92.82(19)
		C8–N2–Ir	137.8(2)
		C1–N3–C14	120.3(3)
		C1–N3–C15	123.7(3)
		C15–N3–C14	116.0(3)
		N2–C1–N1	111.7(3)
		N1–C1–N3	122.3(3)
		N2–C1–N3	126.1(3)

[a] Numbers in parentheses are standard uncertainties in the last significant figures. Atoms are labeled as indicated in Figure 5.

Table 3. Selected interatomic distances (Å) and angles (°) for [Ir{PhNC(NMe$_2$)NPh}(coe)$_2$], **2a**.[a]

N1–C1–N2 / N1–Ir–N2	3.4(3)
N1–Ir–N2 / C16–Ir–C17	77.7(2)
N1–Ir–N2 / C24–Ir–C25	78.5(2)
C16–Ir–C17 / C24–Ir–C25	89.0(1)
C14–N3–C15 / N1–C1–N2	24.5(3)
(N1,C1,N2,N3) / (C2→C7)[b]	77.8(1)
(N1,C1,N2,N3) / (C8→C13)[b]	70.5(1)

[a] Numbers in parentheses are standard uncertainties in the last significant figures. Atoms are labeled as indicated in Figure 1. [b] Angle between the least-squares planes of the guanidinate atoms (N1, C1, N2, and N3) and the aryl ring atoms (*e.g.*, C2, C3, C4, C5, C6, and C7).

As for phenyl-substituted ligands **1a–b**, a one-pot reaction was utilized. On the other hand, the 4-methylphenyl-substituted ligand **1c** could only be prepared by the two-step route, which was proceeded by methylation of di-*p*-tolylthiourea with methyl iodide, amination with dimethylamine, and neutralization with sodium carbonate. As shown in Scheme 16, treatment with methyllithium and subsequent transmetallation using [{Ir(coe)$_2$}$_2$(μ-Cl)$_2$] under an inert atmosphere furnished the orange Ir^{I} complexes of the anionic guanidinates, [Ir{ArNC(NR$_2$)NAr}(coe)$_2$], **2a**–**c**. Complexes **2a**–**c** are well soluble in non-polar organic solvents such as toluene, diethyl ether, and *n*-pentane but only sparingly soluble in acetonitrile. Unlike featureless in the UV–Vis spectra for all guanidine ligands **1a–c** and their lithium guanidinate, **2a–c** exhibit three distinct absorption features around 380–490 nm. The ^{1}H NMR spectra of each of these complexes and the ^{13}C NMR spectrum of **2a** are consistent with a guanidinato-κ^2N,N' and two η^2-coe ligands coordinated to a d^8 Ir^{I} center in a square-planar environment (Figures 1–4). The broadness of the resonance signals at 3.2 and 2.6 and in the range of 1–2 ppm may be attributed to fluxional behavior of the coe ligands in solution. On the basis of the

molecular ion peaks observed by EIMS, **2a**–**c** were identified as mononuclear complexes. The molecular structure of **2a** was confirmed by X-ray crystallography.

Scheme 15. Synthesis of Neutral Guanidines **1a**–**c**

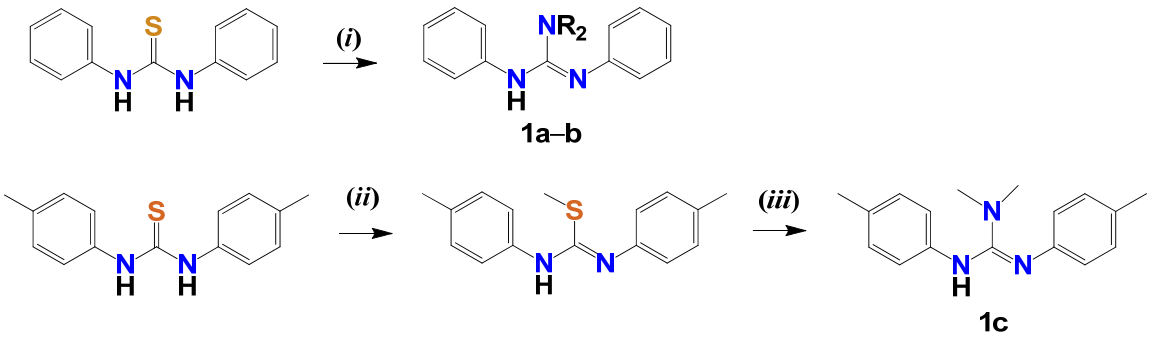

1a, R = Me; **1b**, R = Et

(*i*) R_2NH, NEt_3BzMnO_4, THF; (*ii*) MeI, MeOH, reflux; (*iii*) Me_2NH, MeOH, Na_2CO_3

Scheme 16. Synthesis of [Ir{$ArNC(NR_2)NAr$}$(coe)_2$] Complexes **2a**–**c**

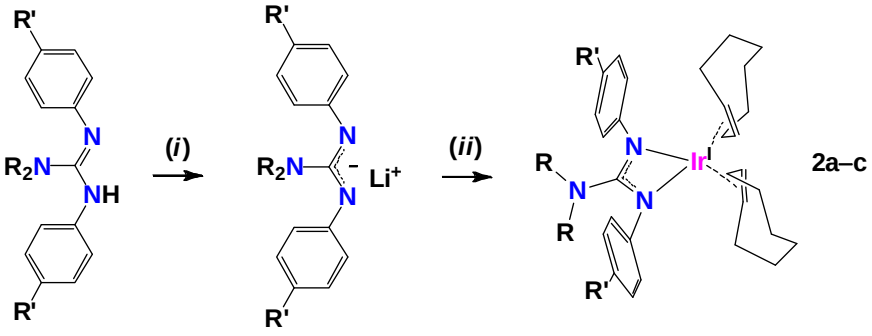

a, R = Me, R' = H; **b**, R = Et, R' = H; **c**, R = R' = Me

(*i*) MeLi, –40°C; (*ii*) 0.5 [{$Ir(coe)_2$}$_2$(μ-$Cl)_2$]

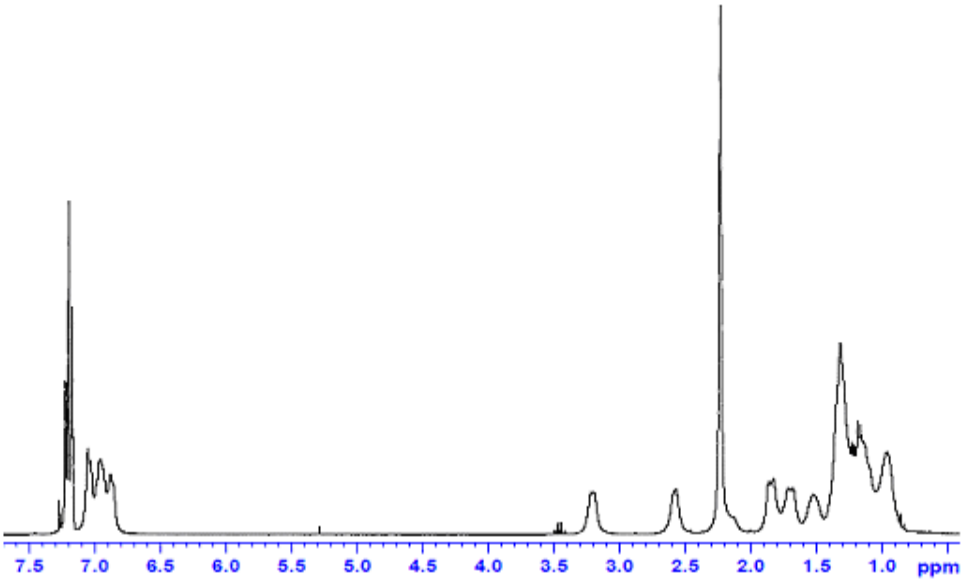

Figure 1. ^{1}H NMR spectrum of **2a** in $CDCl_3$.

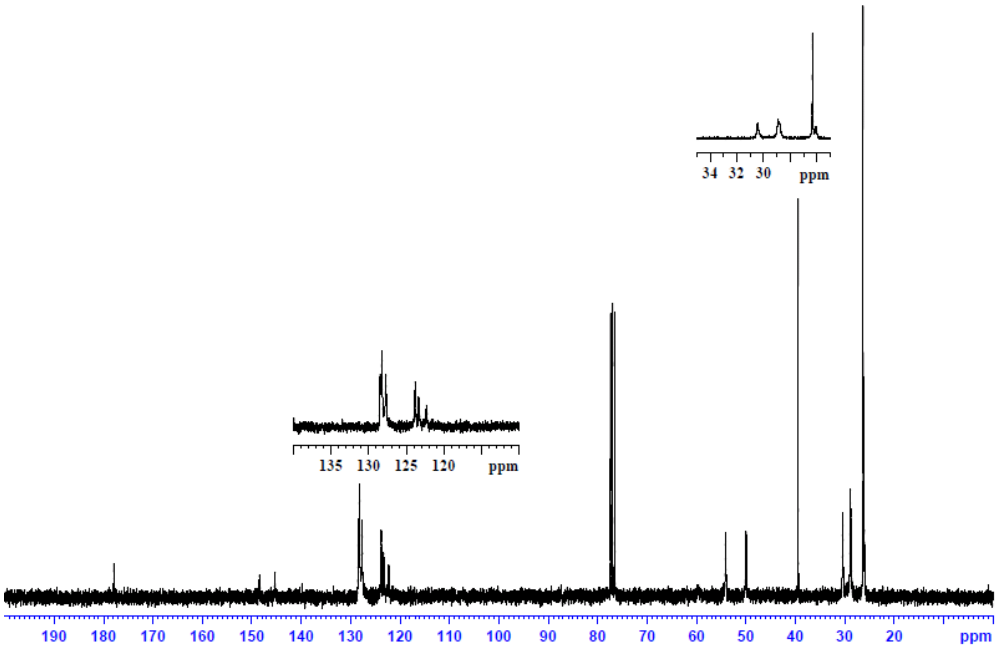

Figure 2. ^{13}C NMR spectrum of **2a** in $CDCl_3$.

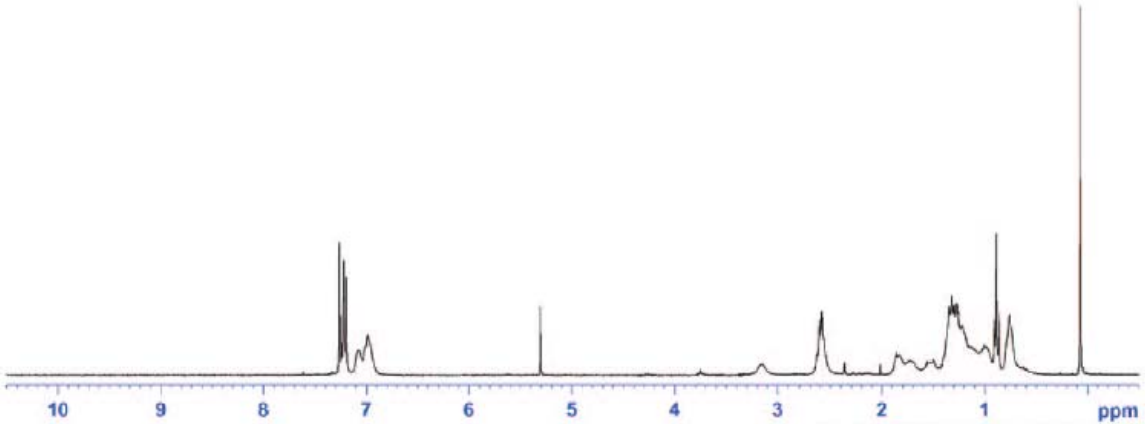

Figure 3. ^{1}H NMR spectrum of **2b** in $CDCl_3$.

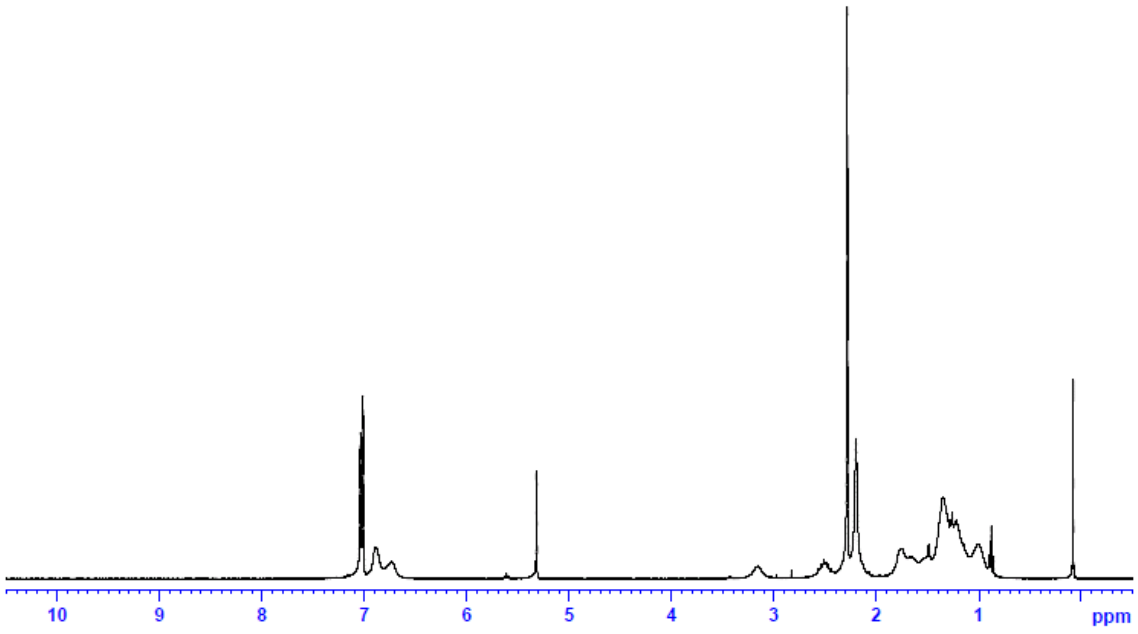

Figure 4. ^{1}H NMR spectrum of **2c** in $CDCl_3$.

*3.3.2 Crystal Structure of [Ir{PhNC(NMe$_2$)NPh}(coe)$_2$] (**2a**)*

Orange single crystals of **2a** were grown from concentrated *n*-pentane solution upon standing at −30 °C. The solid-state molecular structure of **2a** was determined from crystallographic analysis and confirm the mononuclear nature of **2a** (Figure 5 and Tables 1–3). For comparison, with amidinate ligands, both mononuclear and dinuclear complexes have been obtained.[77-79] The Ir–N and Ir–C distances are in the ranges of 2.118(3)–2.122(3) Å and 2.126(3)–2.137(3) Å, respectively, which agree well with values of related complexes.[78-81] Due to the acute bite angles of the chelating guanidinato ligands (N1–Ir–N2, 63.12(10)°), the metal center adopts a distorted square-planar coordination geometry. The structural analysis also reveals important intra-ligand parameters that provide insight into the bonding of the guanidinato ligands. Remarkably, the C–N distances in the planar CN_3 core are nearly identical, 1.335(4)–1.361(4) Å for **2a**. These parameters indicate a high degree of π electron delocalization over the CN_3 core, implicating a significant contribution of the iminium/diamide resonance structure (Scheme 13 in Chapter 2, Structure II). In accord with the sp^2 hybridization expected for efficient lone-pair donation into the CN_3 unit, the N3 atom adopts a trigonal-planar geometry with bond angle sums of 360(3)°. In contrast, the N1 and N2 atoms are more pyramidalized with bond angle sums of 346.3(2) and 352.0(2)°. Although the C14–N3–C15 and N1–C1–N2 planes are slightly twisted with respect to each other (24.5(3)°), presumably due to minor steric interactions between the NR_2 alkyl and the NAr aryl groups, the conjugation of N3 and C1 *p* orbitals is apparently not disrupted.

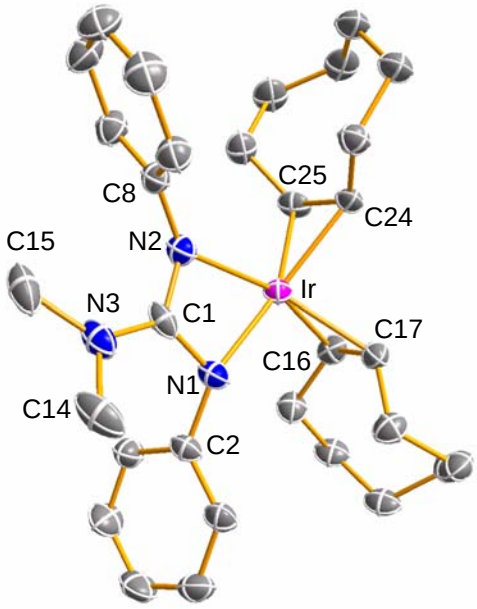

Figure 5. Molecular structure of **2a** showing the atomic numbering scheme. Displacement ellipsoids are drawn at the 50% probability level; hydrogen atoms have been omitted for clarity; color key: pink = Ir, blue = N, gray = C.

The structural parameters of Ir^{I} complexes with the same type of guanidinato ligand but different alkenes were compared. The Ir–N and Ir–C distances for **2a** are slightly longer than those the Ir^{I}(cod) complexes [Ir{PhNC(NEt_2)NPh}(cod)] and [Ir{(2,6-$Me_2C_6H_3$)NC(NMe_2)N(2,6-$Me_2C_6H_3$)}(cod)] (cod = 1,5-cyclooctadiene, Figure 6).[64] For example, the Ir–N and Ir–C distances for these two complexes are in the range of 2.069(2)–2.099(2) Å and 2.095(3)–2.122(3) Å, respectively. This could be due to the lability of the monodentate cyclooctene ligand compared to stronger binding of the bidentate 1,5-cyclooctadiene ligand. The intra-ligand parameters of **2a** and those Ir cod complexes are comparable. For instance, C–N distances in the planar CN_3 core of each complex are nearly identical (1.335(4)–1.361(4)). The bite angles of the chelating guanidinato ligands (N1–Ir–N2 = 63.68(9)°and 63.72(9)°), and the twist angles of C–N3–C and N1–C1–N2 (25.6(1)°and 18.7(3)° are also similar.

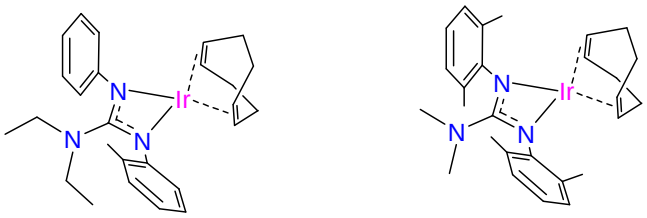

Figure 6. The structures of [Ir{PhNC(NEt$_2$)NPh}(cod)] and [Ir{(2,6-Me$_2$C$_6$H$_3$)NC(NMe$_2$)N(2,6-Me$_2$C$_6$H$_3$)}(cod)].

The Ir–C$_{coe}$ distances of **2a** (2.126(3)–2.137(3) Å) are also comparable to other Ir^{I}(coe)$_2$ complexes (Figure 7). For instance, the Ir–C$_{coe}$ distances for complexes [Ir(η^6-C$_6$H$_6$)(coe)$_2$]PF$_6$, [Ir(η^6-C$_{14}$H$_{10}$)(coe)$_2$]PF$_6$, [Ir(η^6-C$_{20}$H$_{10}$)(coe)$_2$]PF$_6$,[82] [Ir{S$_2$C(NMe$_2$)}(coe)$_2$],[83] [Ir(N{(^{i}Pr)$_2$PS}$_2$)(coe)$_2$], and [Ir(N{(Ph)$_2$PO}$_2$)(coe)$_2$][84] are in the ranges of 2.128–2.173, 2.145–2.162, 2.127–2.164, 2.143–2.155, 2.148–2.163, and 2.180–2.112 Å, respectively. The cyclooctene ligands in the Ir^{I}(coe)$_2$ complexes including **2c** exhibit a crown conformation.

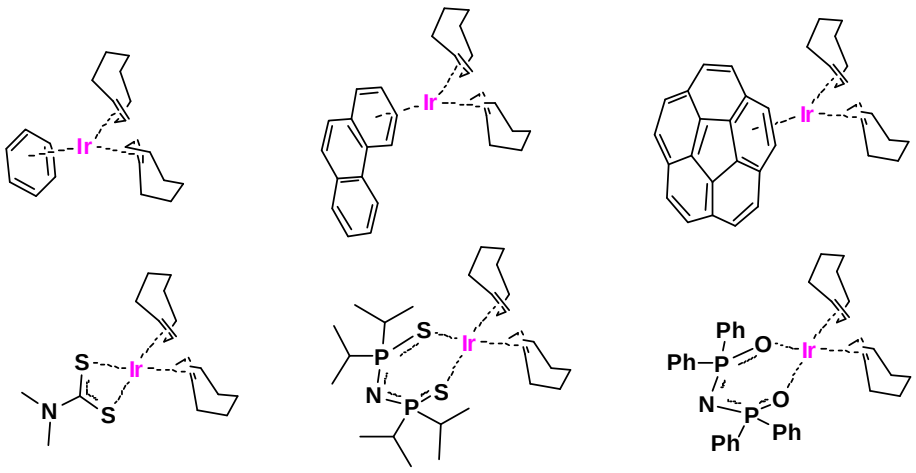

Figure 7. The structures of [Ir(η^6-C$_6$H$_6$)(coe)$_2$]PF$_6$, [Ir(η^6-C$_{14}$H$_{10}$)(coe)$_2$]PF$_6$, [Ir(η^6-C$_{20}$H$_{10}$)(coe)$_2$]PF$_6$, [Ir{S$_2$C(NMe$_2$)}(coe)$_2$], [Ir(N{(Pr^i)$_2$PS}$_2$)(coe)$_2$], and [Ir(N{(Ph)$_2$PO}$_2$)(coe)$_2$].

The intra-ligand structural features of **2a** are unusual, because complexes of guanidinato(1–) ligands typically display more localized bonding with a longer C–N bond to the non-coordinated nitrogen atom and shorter ones to the metal-coordinated nitrogen atoms.[60,85-94] Thus, the bonding in those guanidinate systems is best described by a relatively larger contribution of the amine/amidinate resonance structures (Scheme 13 in Chapter 2, Structure I and III). On the other hand, the greater extent of delocalization observed for **2a** is present in complexes of Ti^{IV},[95,96] Zr^{IV},[97] and Nb^{V}.[98] It has been argued that significant involvement of the lone pair of the NR_2 nitrogen atom is due to the ligands' coordination to an electron-deficient metal center. In this context, the observations made here for low-valent d^8 Ir^{I} complexes may seem surprising. Presumably, the π-acceptor alkene ligand enhances the electron-releasing character of the guanidinato ligand and thus facilitates participation of the NR_2 lone pair in CN_3 π bonding.

3.3.3 O_2 Reactivity

In solution, complexes **2a–c** react readily with dioxygen, as indicated by the disappearance of their characteristic absorption features in the UV–Vis region and appearance of a new band at *ca.* 660 nm (Figures 8–10). For example, at –40 °C, the formation time of a blue intermediate (λ_{max} = 660 nm) for **2a** in toluene solution with O_2 is *ca.* 35 min (30 min, λ_{max} = 660 nm for **2b**, Figure 9; 20 min, λ_{max} = 660 nm for **2c**, Figures 10). The blue species is unstable and decays gradually to a green species (λ_{max} = 620 nm) over time. The intermediate and final product were characterized by ^{1}H NMR spectroscopy and mass spectrometry (Table 4). In the ^{1}H NMR spectra, broad resonances were observed, which indicate mixture of products; possibly oligomerization of complexes could occur during oxidation. Oligomerization of complexes may be a result from dissociation of cyclooctene which was detected in the reaction of **2a** with O_2 by ^{1}H NMR spectroscopy. In ESI(+)MS, one bis(guanidinato) or oxygen-containing complex

(*m/z* = 667, $\{Ir(L)_2 - 2\ H\}^+$ or $\{\mathbf{2a} + O\}^+$) and two dinuclear Ir complexes (*m/z* = 893, $\{Ir_2(L)_2(O)(OH)\}^+$) and *m/z* = 1131, $\{Ir_2(L)_3(O)(OH)\}^+$) were detected. In order to identify the species shown at *m/z* = 667 whether oxygen atom was involved in this ion, an isotope experiment was conducted by the reaction of **2a** with $^{18}O_2$. No *m/z* shift was observed when comparing the ESI mass spectra of **2a** + $^{16}O_2$ to that of **2a** + $^{18}O_2$. Therefore, the peak shown at *m/z* = 667 must be due to the $\{Ir(L)_2 - 2\ H\}^+$ ion. To confirm this assignment, **2b–c** were also reacted with O_2, and characterized by ESI(+)MS. Both resulted in an ion shown at *m/z* = 723 ($\{Ir(L)_2 - 2H\}^+$) in the ESI(+)MS, which is indicative of the bis(guanidinato)iridium complex. In addition, when the solution of the reaction of **2a** + O_2 was subjected to EI mass spectrometry, one weak intensity peak shown at *m/z* = 907 suggested that the tris(guanidinato)iridium complex $[Ir^{III}(L)_3]$ was formed in this reaction. Although bis(guanidinato) and two dinuclear Ir complexes were observed in the ESI(+)MS and the trace amount of tris(guanidinato) was found in the EIMS, attempts to purify and isolate a well-defined product were unsuccessful.

Table 4. Mass-to-charge ratios (*m/z*) obtained from ESI(+)MS for the reactions of **2a–c** with O_2.[a]

Reaction	*m/z*(calc. value)
2a + O_2	240.1(240.2), 667.1(667.2), 892.8(893.2), 1131.0(1131.3)
2a + $^{18}O_2$	240.1(240.2), 667.2(667.2), 892.9(893.2), 1131.2(1131.3)
2a + O_2 (EI MS)	907.4(907.4)
2b + O_2	268.2(268.2), 723.3(723.3), 949.1(949.3)
2c + O_2	268.1(268.2), 723.1(723.3), 949.1(949.3)

[a] In toluene.

The formation of bis(guanidinato) and tris(guanidinato) Ir complexes suggests reorganization of the Ir complex (dissociation of ligand from metal complex) is required to form stable products. In order to increase the yields of the bis(guanidinato) or tris(guanidinato) Ir complexes, the oxidations were carried out in the presence of excess lithium guanidinates. Although no difference in the mass spectrometry was observed when carrying out the reaction in the presence of 1 equiv of lithium guanidinate, the significant increase of intensity of the peak at *m/z* = 907 found in the EIMS for the reaction done in the presence of 10 equiv of lithium guanidinate suggests that the yield of tris(guanidinato) Ir complex was improved. The formation of the tris(guanidinato) Ir complex was confirmed by ^{1}H NMR spectroscopy. This observation shows that [Ir{ArNC(NR$_2$)NAr}(coe)$_2$] complexes can serve as precursors for preparing tris(guanidinato) complexes.

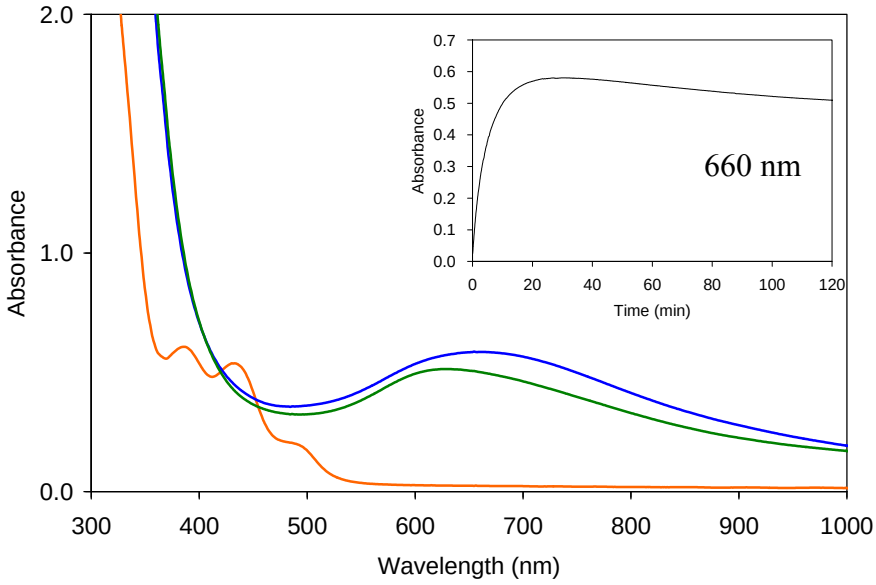

Figure 8. UV–Vis spectrum of 1.25 mM **2a** (orange) in toluene, the intermediate (blue) of the reaction with O_2, and the decay product (green). Inset: Time course of the reaction of **2a** (—, black; λ, 660 nm). Pathlength = 0.5 cm.

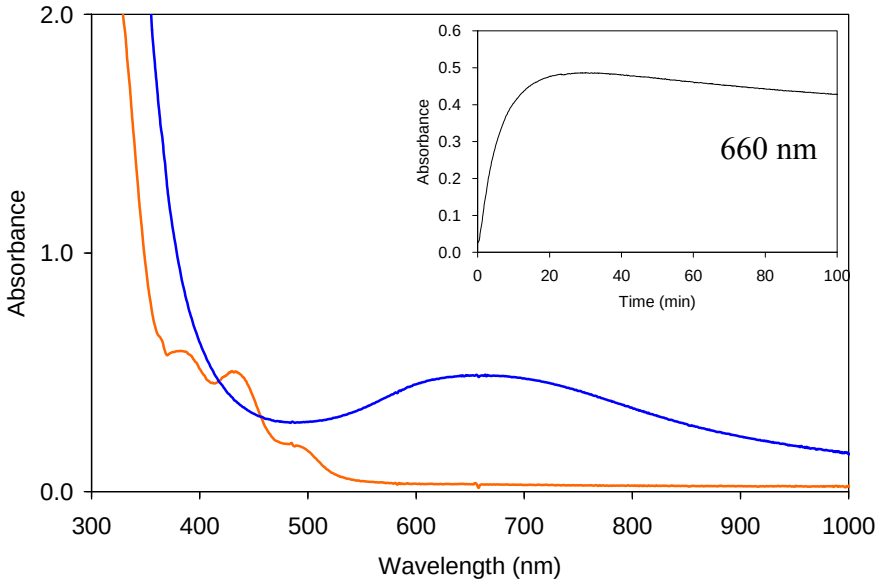

Figure 9. UV–Vis spectrum of 1.25 mM **2b** (orange) in toluene and the intermediate (blue) of the reaction with O_2. Inset: Time course of the reaction of **2b** (—, black; λ, 660 nm). Pathlength = 0.5 cm.

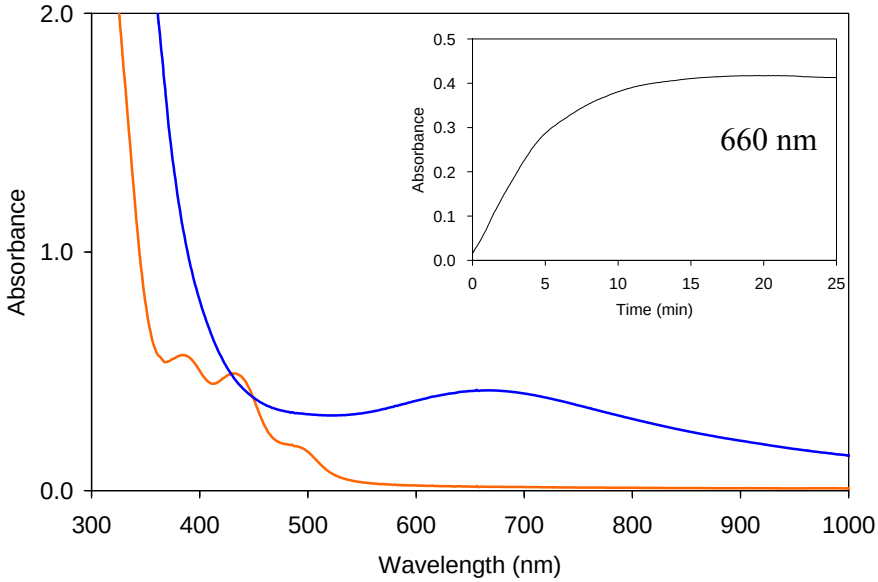

Figure 10. UV–Vis spectrum of 1.25 mM **2c** (orange) in toluene and the intermediate (blue) of the reaction with O_2. Inset: Time course of the reaction of **2c** (—, black; λ, 660 nm). Pathlength = 0.5 cm.

3.4 Conclusion

The neutral guanidines were synthesized and used for the preparation of mononuclear $[Ir(L)(coe)_2]$ complexes via deprotonation and transmetallation under an inert atmosphere. The solid state structure of **2a** shows the extent of delocalization in the CN_3 core of the guanidinato ligand. The rare complexes of a low-valent Ir center coordinated to bidentate guanidinato(1–) ligands were prepared and characterized. While the $[Ir(ArNC(NR_2)NAr)(coe)_2]$ complexes reacted readily with O_2, investigation is needed to gain further insight into the blue intermediate. The $[Ir(ArNC(NR_2)NAr)(coe)_2]$ complexes, containing a more labile alkene ligand, were found to be useful precursors for the synthesis of tris(guanidinato) complexes of Ir^{III}. The latter could be isolated from the reaction with O_2 in the presence of added lithium guanidinates.

CHAPTER 4

TRIS(GUANIDINATO) COMPLEXES OF IRIDIUM(III) AND IRIDIUM(IV)

4.1 Introduction

Electron-rich tris(guanidinato) complexes of Ir^{III}, [Ir{ArNC(NR$_2$)NAr}$_3$] (where R = Me or Et; Ar = Ph or 4-MeC_6H_4), were synthesized from the corresponding lithium ganidinato ligands and Ir^{I} precursors [Ir{ArNC(NR$_2$)NAr}(C_8H_{14})$_2$] and [{Ir(coe)$_2$}$_2$(μ-Cl)$_2$] (C_8H_{14} = *cis*-cyclooctene), are air-sensitive, and can be electrochemically oxidized in two one-electron transfer steps. The first electron transfer is reversible and occurs at much lower potentials than typical for Ir^{III}. Chemical oxidation by [$FeCp_2$]PF_6 afforded isolable, paramagnetic Ir^{IV} compounds, [Ir{ArNC(NR2)NAr}$_3$]PF_6, which were characterized by analytical and spectroscopic methods and a single-crystal structure determination, demonstrating that Ir^{IV} is accessible in a nitrogen-donor ligand environment. A part of the resuts in this Chapter has been published in 2009.[99]

4.2 Experimental Section

Materials. All reagents and solvents were purchased from commercial sources and were used as received, unless noted otherwise. Acetonitrile, dichloromethane, diethyl ether, tetrahydrofuran, and toluene were deoxygenated by sparging with N_2 and purified by passage through two packed columns of molecular sieves under an N_2 pressure (MBraun solvent purification system). *n*-Pentane was dried over Na and distilled under N_2 prior to use.[65] Preparation and handling of air- and moisture-sensitive materials were carried out under an inert gas atmosphere by using either standard Schlenk and vacuum

line techniques or a glovebox. Dioxygen was dried by passage through a short column of Drierite. [{Ir(coe)$_2$}$_2$(μ-Cl)$_2$], the guanidines PhN=C(NMe$_2$)NHPh (**1a**), PhN=C(NEt$_2$)NHPh (**1b**) and (4-MeC$_6$H$_4$)N=C(NMe$_2$)NH(4-MeC$_6$H$_4$) (**1c**) and the Ir^{I} complex [Ir{PhNC(NMe$_2$)NPh}(coe)$_2$] (**2a**) (coe = *cis*-cyclooctene) are synthesized according to published procedures previously.[64,66] The complexes [Ir{PhNC(NEt$_2$)NPh}(coe)$_2$] (**2b**) and [Ir{(4-MeC$_6$H$_4$)NC(NMe$_2$)N(4-MeC$_6$H$_4$)}(coe)$_2$] (**2c**) are prepared analogously to **2a**. The guanidine ligand (4-MeC$_6$H$_4$)N=C(NEt$_2$)NH(4-MeC$_6$H$_4$) (**1d**)[100] was prepared by the same procedure as for **1c**. Elemental analyses were performed by Atlantic Microlab, Inc., Norcross, GA, USA.

Physical Methods. NMR spectra were recorded on a Bruker Avance DRX 400 spectrometer at ambient temperature. ^{1}H chemical shifts are reported in parts per million (ppm) and were referenced to residual solvent peaks. Mid- and near-IR spectra were recorded on a Bruker Vertex 70 Fourier-transform IR spectrometer. Samples for the mid-IR range were prepared by grinding the solid compound with KBr and pressing the mixture into a disk. For the near-IR range, 0.1 mM solutions of the compounds in CDCl$_3$ were used. Mass spectral data were acquired on a quadrupole ion trap ThermoFinnigan LCQ Deca mass spectrometer using an electrospray ionization source or on a double-focusing magnetic-sector Micromass, Inc., Autospec mass spectrometer using an electron impact ionization source (equipped with a solids probe). UV–Visible spectra were recorded on an HP 8454a diode array spectrophotometer (Agilent Technologies). Cyclic voltammetry (CV) and differential pulse voltammetry (DPV) measurements were carried out with a CH Instruments potentiostat (Model 620C Electrochemical Analyzer) and a standard three-electrode configuration consisting of a Pt disc working electrode, a Pt wire counter electrode and an Ag/AgNO$_3$ reference electrode (0.01 M AgNO$_3$ in MeCN; supporting electrolyte, 0.1 M NBu$_4$ClO$_4$). The voltammograms were recorded on solutions of the analyte (0.1 mM) and the supporting electrolyte (0.1 M NBu$_4$ClO$_4$) in CH$_2$Cl$_2$ under an Ar atmosphere at 293 K (*Caution:* Mixtures of perchlorate salts and

metal complexes are potentially explosive and should be handled with care.) Typical measurement parameters were scan rate of 0.05 to 0.5 $V \cdot s^{-1}$ for CV and a potential increment of 4 mV, an amplitude of 50 mV, and a pulse period of 0.2 s for DPV. Potentials are reported referenced to an external $[FeCp_2]/[FeCp_2]^+$ redox system, which can be converted to the SCE scale by adding 0.48 V (SCE, aqueous saturated calomel electrode).[11,101] Potentials relative to SCE can be converted to the NHE scale by adding 0.24 V (NHE, normal hydrogen electrode).[102] Continuous-wave (CW) EPR spectra were recorded at 77 K on a Bruker EMX-61 spectrometer equipped with a liquid N_2 cold-finger Dewar flask. Typical EPR spectral parameters were an X-band microwave frequency of 9.29 GHz, a modulation frequency of 100 kHz, a modulation amplitude of 10 G, and a microwave power of 3.2 mW (sample concentration, 1 mM in CH_2Cl_2).

General Procedure for the Synthesis of [Ir{ArNC(NR$_2$)NAr}$_3$] Complexes (Method 1). In a typical procedure, 1.2 mmol of the *N*,*N*-dialkyl-*N*′,*N*″-diarylguanidine was dissolved in 15 mL of degassed diethyl ether. The solution was cooled to –40 °C and 1.1 equiv of methyllithium (1.6 M in Et_2O) was added under stirring. The resulting solution was allowed to warm to 20 °C and stirred for 1 h. Upon removal of the volatiles under reduced pressure, the Li^+ salt of the *N*,*N*-dialkyl-*N*′,*N*″-diarylguanidinate anion, $Li\{ArNC(NR_2)NAr\} \cdot Et_2O$, was isolated as a colorless powder and stored under rigorous exclusion of moisture. The powder could also be recrystallized from a concentrated *n*-pentane solution at –30 °C to afford a microcrystalline solid.

A solution of 0.30 mmol of lithium guanidinate and 0.10 mmol of $[Ir\{ArNC(NR_2)NAr\}(coe)_2]$ in 10 mL of toluene was continuously purged with O_2 under stirring at 20 °C. The orange solution turned into a dark brown mixture. After 10 min, the volatiles were removed under reduced pressure. Because the $[Ir\{ArNC(NR_2)NAr\}_3]$ complexes react slowly with O_2, the remaining steps were carried out in an N_2 atmosphere. The product was extracted from the residue with 30 mL of *n*-pentane. Upon storing this solution at 20 °C, a yellow precipitate was obtained within several days,

which was separated by filtration and washed with 5 mL of acetonitrile. The residue was recrystallized from a saturated solution in dichloromethane by slow evaporation of the solvent at 20 °C and dried *in vacuo*. (It is assumed that **3a**–**c** were obtained as racemic mixtures of Δ-and Λ-enantiomers.)

[Ir{PhNC(NMe$_2$)NPh}$_3$] (3a). Yield: 49 mg (54%). Anal. Calcd for $C_{45}H_{48}IrN_9$: C, 59.58; H, 5.33; N, 13.90. Found: C, 59.54; H, 5.42; N, 14.04. ^{1}H NMR (400 MHz, $CDCl_3$, δ): 6.94 (t, J = 7.8 Hz, 12H, Ar H), 6.78 (t, J = 7.4 Hz, 6H, Ar H), 6.62 (d, J = 7.8 Hz, 12H, Ar H), 2.44 (s, 18H, NCH_3). EIMS (70 eV) m/z: $M^{+\bullet}$ calcd for $C_{45}H_{48}IrN_9$, 907.37; found, 907.4. UV–Vis (CH_2Cl_2) λ_{max}, nm (ε): 305 (60000), 362 (25000).

[Ir{PhNC(NEt$_2$)NPh}$_3$] (3b). Yield: 41 mg (41%). Anal. Calcd for $C_{51}H_{60}IrN_9$: C, 61.79; H, 6.10; N, 12.72. Found: C, 61.45; H, 6.04; N, 12.28. ^{1}H NMR (400 MHz, $CDCl_3$, δ): 6.94 (t, J = 7.7 Hz, 12H, Ar H), 6.81–6.72 (m, 18H, Ar H), 2.93 (m, 6H, NCH_3CH_3), 2.64 (m, 6H, NCH_2CH_3), 0.73 (t, J = 7.1 Hz, 18H, NCH_2CH_3). EIMS (70 eV) m/z: $M^{+\bullet}$ calcd for $C_{51}H_{60}IrN_9$, 991.46; found, 991.5. UV–Vis (CH_2Cl_2) λ_{max}, nm (ε): 305 (60000), 363 (25000).

[Ir{(4-MeC$_6$H$_4$)NC(NMe$_2$)N(4-MeC$_6$H$_4$)}$_3$] (3c). Yield: 43 mg (43%). Anal. Calcd for $C_{51}H_{60}IrN_9$: C, 61.79; H, 6.10; N, 12.72. Found: C, 61.62; H, 6.19; N, 12.42. ^{1}H NMR (400 MHz, $CDCl_3$, δ): 6.74 (d, J = 8.2 Hz, 12H, Ar H), 6.54 (d, J = 8.2 Hz, 12H, Ar H), 2.41 (s, 18H, NCH_3), 2.20 (s, 18H, $C_6H_4CH_3$). EIMS (70 eV) m/z: $M^{+\bullet}$ calcd for $C_{51}H_{60}IrN_9$, 991.46; found, 991.5. UV–Vis (CH_2Cl_2) λ_{max}, nm (ε): 305 (49000), 365 (25000).

General Procedure for the Synthesis of [Ir{ArNC(NR$_2$)NAr}$_3$] Complexes (Method 2). A solution of 0.40 mmol of lithium guanidinate and 0.05 mmol of [Ir{ArNC(NR$_2$)NAr}(coe)$_2$] in 5 mL of toluene was stirred at 20 °C for 30 min. Subsequently, the solution mixture was purged with O_2 under stirring at 20 °C for 10 min. The orange solution turned into a dark brown mixture. The volatiles were removed under reduced pressure. Because the [Ir{ArNC(NR$_2$)NAr}$_3$] complexes react slowly with

O_2, the remaining steps were carried out in an N_2 atmosphere. The product was extracted from the residue with 30 mL of *n*-pentane. Upon storing this solution at 20 °C, a yellow precipitate was obtained within several days, which was separated by filtration and washed with 5 mL of acetonitrile. This product can be recrystallized from a saturated solution in dichloromethane by slow evaporation of the solvent at 20 °C, but recrystallization is not required to obtain pure product.

The yields for **2a**, **2b**, and **2c** were 29 mg (32%), 35 mg (35%), and 34 mg (34%), respectively. The UV−Vis and ^{1}H NMR spectra of the products are identical to that of products synthesized by previous method.

[Ir{(4-MeC$_6$H$_4$)NC(NEt$_2$)N(4-MeC$_6$H$_4$)}$_3$] (3d). Yield: 34 mg (32%). Anal. calcd for $C_{57}H_{72}IrN_9$: C, 63.66; H, 6.75; N, 11.72. Found: C, 63.25; H, 6.73; N, 11.82. ^{1}H NMR (300 MHz, $CDCl_3$, δ): 6.80 (d, J = 7.4 Hz, 12H, Ar H), 6.45 (br, 12H, Ar H), 2.96 (m, J = 6.9 Hz, 6H, NCH_2CH$_3$), 2.66 (m, J = 6.9 Hz, 6H, NCH_2CH$_3$), 2.38 (s, 18H, $C_6H_4CH_3$), 0.73 (t, J = 6.9 Hz, 18H, NCH$_2$CH_3). EIMS (70 eV) *m/z*: $M^{+\cdot}$ calcd for $C_{57}H_{72}IrN_9$, 1075.55; found, 1075.2. UV−Vis (CH_2Cl_2) λ_{max}, nm (ε): 307 (54000), 363 (27000).

General Procedure for the Synthesis of [Ir{ArNC(NR$_2$)NAr}$_3$]PF$_6$. In an N_2 atmosphere, a solution of 6.6 mg (0.020 mmol) of ferrocenium hexafluorophosphate in 1 mL of acetonitrile was added to a suspension of 0.020 mmol of [Ir{ArNC(NR$_2$)NAr}$_3$] **3a–d** in 20 mL of dichloromethane at 20 °C. The reaction mixture immediately turned into a clear, dark violet solution, which was stirred for 1 h. The solution was concentrated to a volume of 2 mL, and 8 mL of diethyl ether was added, causing the formation of a violet precipitate. The precipitate was separated by filtration and dissolved in 10 mL of acetonitrile. This solution was filtered to remove any trace amount of unreacted [Ir{ArNC(NR$_2$)NAr}$_3$]. Upon evaporation of the solvent, the product was isolated as a solid and recrystallized by vapor diffusion of *n*-pentane into a dichloromethane solution at –30 °C. Dark violet to black single crystals of X-ray diffraction quality were typically

obtained within several days. (It is assumed that **4a**–**d** were obtained as racemic mixtures of Δ-and Λ-enantiomers.)

[Ir{PhNC(NMe$_2$)NPh}$_3$]PF$_6$ (4a). Yield: 19.8 mg (94%). Anal. Calcd for $C_{45}H_{48}F_6IrN_9P$: C, 51.37; H, 4.60; N, 11.98. Found: C, 51.66; H, 4.64; N, 11.77. ESI(+)MS (*m*/*z*): M^+ calcd for $C_{45}H_{48}IrN_9$, 907.37; found, 907.2. UV–Vis (CH_2Cl_2) λ_{max}, nm (ε): 284 (64000), ~300 (sh, 59000), ~540 (2800), 696 (3100).

[Ir{PhNC(NEt$_2$)NPh}$_3$]PF$_6$ (4b). Yield: 21.3 mg (94%). Anal. Calcd for $C_{51}H_{60}F_6IrN_9P$: C, 53.91; H, 5.32; N, 11.09. Found: C, 53.73; H, 5.25; N, 10.91. ESI(+)MS (*m*/*z*): M^+ calcd for $C_{51}H_{60}IrN_9$, 991.46; found, 991.3. UV–Vis (CH_2Cl_2) λ_{max}, nm (ε): 284 (62000), 300 (59000), ~540 (2300), 692 (3000).

[Ir{(4-MeC$_6$H$_4$)NC(NMe$_2$)N(4-MeC$_6$H$_4$)}$_3$]PF$_6$ (4c). Yield: 20.9 mg (92%). Anal. Calcd for $C_{51}H_{60}F_6IrN_9P$: C, 53.91; H, 5.32; N, 11.09. Found: C, 54.14; H, 5.29; N, 11.15. ESI(+)MS (*m*/*z*): M^+ calcd for $C_{51}H_{60}IrN_9$, 991.46; found, 991.2. UV–Vis (CH_2Cl_2) λ_{max}, nm (ε): 285 (58000), ~300 (sh, 56000), ~565 (2900), 713 (3100).

[Ir{(4-MeC$_6$H$_4$)NC(NEt$_2$)N(4-MeC$_6$H$_4$)}$_3$]PF$_6$ (4d). Yield: 23 mg (94%). Anal. calcd for $C_{57}H_{72}F_6IrN_9P$: C, 56.10; H, 5.95; N, 10.33. Found: C, 56.46; H, 6.05; N, 10.09. ESI(+)MS (*m*/*z*): M^+ calcd for $C_{57}H_{72}IrN_9$, 1075.55; found, 1075.5. UV–Vis (CH_2Cl_2) λ_{max}, nm (ε): 300 (49000), ~565 (2700), 709 (3100).

X-ray Crystallographic Analysis. A single crystal of **4a** was coated with Paratone N oil and mounted on a glass capillary for data collection at 190(2) K on a Nonius KappaCCD diffractometer using Mo *Kα* radiation (graphite monochromator). The temperature was controlled by an Oxford Cryostream Cooler (700 series, N_2 gas). Data collection, data reduction, and absorption correction were carried out following standard CCD techniques using the software packages Collect and HKL-2000.[69,70] Final cell constants were calculated from 20595 reflections from the complete data set. The chiral space group *I*23 was determined based on systematic absences and intensity statistics. The structure was solved by direct methods and refined by full-matrix least-squares

minimization and difference Fourier methods (SHELXTL v.6.12).[71,72] All non-hydrogen atoms were refined with anisotropic displacement parameters. All hydrogen atoms were placed in ideal positions and refined as riding atoms with relative isotropic displacement parameters. Inversion of the structure yielded the correct absolute structure, as indicated by the Flack x parameter and improvements in *R* indices; the unit cell thus contains the Δ-enantiomer of **4a**. (Note: The largest ratio of the final least-squares parameter shift to the final standard uncertainty was larger than usual, because the Flack x parameter was negative and reset to 0 by the program.) The final full-matrix least-squares refinement *R* indices were $R1 = 0.0403$ and $wR2 = 0.0674$ (F^2, all data). Table 5 contains additional crystal and refinement information. Selected distances and angles are summarized in Tables 6 and 7.

Table 5. Crystallographic data and structure refinement for $[Ir\{PhNC(NMe_2)NPh\}_3]PF_6$, **4a**.

Empirical formula	$C_{45}H_{48}F_6IrN_9P$
Formula weight	1052.09
Crystal habit, color	prism, black
Crystal size	0.23 x 0.14 x 0.11 mm^3
Temperature, T	190(2) K
Wavelength, λ	0.71073 Å
Crystal system	cubic
Space group	$I23$
Unit cell dimensions	a = 20.745(3) Å
Volume, V	8928(2) $Å^3$
Z	8
Calculated density	1.566 $Mg \cdot m^{-3}$
Absorption coefficient, ε	3.095 mm^{-1}
$F(000)$	4216
θ range for data collection	3.11 to 27.86°
Limiting indices	$-26 \le h \le 27$, $-27 \le k \le 27$, $-27 \le l \le 27$
Reflections collected / unique	39519 / 3559 [R(int) = 0.0865]
Completeness to	99.8% (θ = 27.86°)
Max. and min. transmission	0.7370 and 0.5299
Refinement method	Full-matrix least-squares on F^2
Data / restraints / parameters	3559 / 0 / 208
Goodness-of-fit on F^2	1.126
Final R indices [I>2sigma(I)]	$R1$ = 0.0312, $wR2$ = 0.0639
R indices (all data)	$R1$ = 0.0403, $wR2$ = 0.0674
Absolute structure parameter	0.000(8)
Largest diff. peak and hole	1.517 and –1.056 $e \cdot Å^{-3}$

Table 6. Selected interatomic distances (Å) and angles (°) for $[Ir\{PhNC(NMe_2)NPh\}_3]PF_6$, **4a**.[a]

Distances (Å)		Angles (°)	
Ir–N1	2.040(3)	N1–Ir–N2	63.92(14)
Ir–N2	2.064(3)	N1#1–Ir-N1	103.89(11)
		N1-Ir–N2#1	165.25(13)
		N1-Ir–N2#2	87.76(13)
		N2#1–Ir-N2	105.71(11)
N1–C1	1.337(5)	C1–N1–C2	128.5(4)
N1–C2	1.409(5)	C1–N1–Ir	95.3(3)
N2–C1	1.361(5)	C2–N1–Ir	131.3(3)
N2–C8	1.399(5)	C1–N2–C8	126.8(3)
N3–C1	1.349(6)	C1–N2–Ir	93.5(2)
N3–C14	1.458(6)	C8–N2–Ir	131.3(3)
N3–C15	1.454(6)	C1–N3–C14	121.3(4)
		C1–N3–C15	121.5(4)
		C15–N3–C14	116.9(4)
		N1–C1–N2	107.3(3)
		N1–C1–N3	126.5(4)
		N3–C1–N2	126.3(4)
P1–F1	1.576(5)	F1#1–P1–F1	90.0
P2–F2	1.580(4)	F2–P2–F3	90.21(13)
P2–F3	1.599(3)	F2–P2–F3#6	89.79(13)
		F2#6–P2–F2	180.0
		F3#6–P2–F3	90.1(3)
		F3#7–P2–F3	89.9(3)
		F3#8–P2–F3	179.6(3)

[a] Numbers in parentheses are standard uncertainties in the last significant figures. Atoms are labeled as indicated in Figure 12. Symmetry operations: #1, y, z, x; #2, z, x, y; #6, –x+1, –y+2, z; #7, x, –y+2, –z+2; #8, –x+1, y, –z+2.

Table 7. Selected dihedral angles (°) for $[Ir\{PhNC(NMe_2)NPh\}_3]PF_6$, **4a**.[a]

N1–C1–N2 / N1–Ir–N2	0.3(3)
C14–N3–C15 / N1–C1–N2	34.7(3)
(N1,C1,N2,N3) / (C2→C7)[b]	46.8(1)
(N1,C1,N2,N3) / (C8→C13)[b]	37.3(2)

[a] Numbers in parentheses are standard uncertainties in the last significant figures. Atoms are labeled as indicated in Figure 12.[b] Angle between the least-squares planes of the guanidinate atoms (N1, C1, N2, and N3) and the aryl ring atoms (*e.g.*, C2, C3, C4, C5, C6, and C7).

4.3 Results and Discussion

4.3.1 Synthesis of Iridium(III) Complexes

The Ir^{III} complexes $[Ir\{ArNC(NR_2)NAr\}_3]$; where R = Me, Ar = Ph **(3a)**; R = Et, Ar = Ph **(3b)**; R = Me, Ar = 4-MeC_6H_4 **(3c)**; R = Et, Ar = 4-MeC_6H_4 **(3d)**; were synthesized by the reaction of the corresponding $[Ir\{ArNC(NR_2)NAr\}(coe)_2]$ complex with the appropriate lithium guanidinate and O_2.[99] When **2a** was reacted with O_2 in the absence of lithium guanidinate in toluene solution, the color of the solution turned blue/green, and a trace amount of tris(chelate)iridium(III) complexes was observed by EIMS. Because the formation of this complex required two additional equiv of guanidinate, the reaction was carried out in the presence of an excess of lithium guanidinate in order to increase the yield of tris(chelate)iridium(III) complex. After separation of by-products, the Ir^{III} complexes were obtained in yields of 40-50%. Upon purging with O_2, the formation of precipitates, some kind of lithium salts, was observed, and the dissociation of cyclooctene was noticed and observed by ^1H NMR spectroscopy. Therefore the formation of tris(guanidinato)iridium(III) complexes was potentially formed through the following steps: oxidation of O_2 with Ir center to form metal-oxygen product, dissociation of cyclooctene, formation of lithium salts and tris(guanidinato)iridium(III). It is known in the literature that coordinated olefins are

prone to dissociate when Ir^{I} and Rh^{I} alkene complexes get oxidized to higher oxidation states,[103] which weaken the affinity of olefins to Ir and Rh centers. Finally, in order to satisfy octahedron geometry, guanidinates would occupy the vacancy of the coordination site of Ir.Alternatively, **3a–d**, where R = Et, Ar = 4-MeC_6H_4 **(3d)**, could also be synthesized directly from [{Ir(coe)$_2$}$_2$(μ-Cl)$_2$], with the appropriate lithium guanidinates and dioxygen, as shown in Scheme 17. While the yields were lower than those of using [Ir{ArNC(NR_2)NAr}(coe)$_2$] as the starting materials, the overall yields were still comparable to the two-step method.

We also attempted to synthesize the tris(guanidinato)iridium(III) complex with a more sterically demanding ligand, {(2,6-$Me_2C_6H_3$)NC(NMe_2)N(2,6-$Me_2C_6H_3$)}$^-$, but no such compounds could not be prepared by either method. Apparently, the two methyl groups in ortho position cause steric hindrance and preclude coordination of three of these ligands to the Ir center. In fact, no tris(chelate) complex of this ligand has been described. Attempted synthesis of tris(guanidinato)iridium(III) complexes from $IrCl_3$ in ethoxyether or [Ir{ArNC(NR_2)NAr}(coe)$_2$] in toluene with neutral guanidines under reflux was also explored, but the yield was very insignificant (< 3%).

Scheme 17. Synthesis of Ir^{III} Compounds **3a**–**d**.

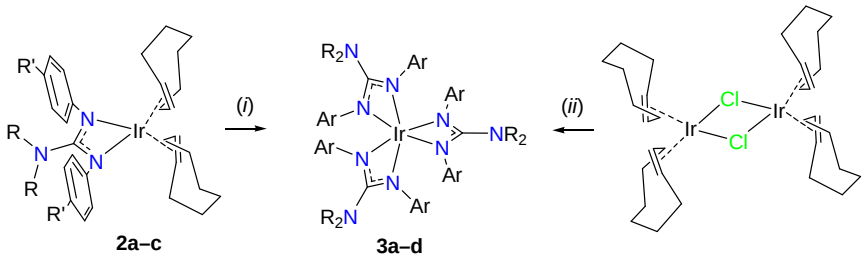

a, R = Me, R' = H; **b**, R = Et, R' = H; **c**, R = R' = Me; Ar = 4-C_6H_4R'; **d**, R = Et, R' = Me; Ar = 4-C_6H_4R';

(*i*) 3 equiv of Li{ArNC(NR_2)NAr}, O_2; (*ii*) 8 equiv of Li{ArNC(NR_2)NAr}, O_2

Complexes **3a–d** are soluble in the chlorinated solvent CH_2Cl_2, $CHCl_3$, CCl_4, but the solubility is low, and they are insoluble in other common organic solvents. They were characterized by elemental analysis, EIMS, ^{1}H NMR and UV–Vis spectroscopy.

4.3.2 Spectroscopic Characterization of Iridium(III) Complexes

The ^{1}H NMR spectra of all complexes displayed a single set of resonances of ligands which indicate that the symmetric N,N'-chelating binding mode is retained in solution and the complexes are consistent with coordination to a low-spin d^6 Ir^{III} center in the expected D_3 symmetric environment for **3a** and **3c** (Figures 22–25). In addition to aryl and methyl proton resonances, **3b** and **3d** exhibited two distinct muliplets for the protons of the diastereotopic methylene groups of the diethylamino group indicating C_3 symmetry for these two complexes in solution. The chemical shifts of the Ir^{III} complexes are shifted upfield by (*ca.* 0.5 ppm for NMe_2 and *ca.* 0.3–0.7 ppm for NEt_2) compared to those of all groups of protons in the corresponding neutral guanidines.[64] Unfortunately, the decent ^{13}C NMR spectra could not be obtained due to the poor solubility.

4.3.3 Electrochemical Characterization of Iridium(III) Complexes

For **3a–d**, the cyclic voltammograms (CVs) and differential pulse voltammograms (DPVs) all showed that these complexes can be oxidized at unusually low potentials. The CV and DPV results are in good agreement, and no reduction processes for all complexes were observed (Figure 11 for **3a**, and Figures 26–28 for **3b–d**).

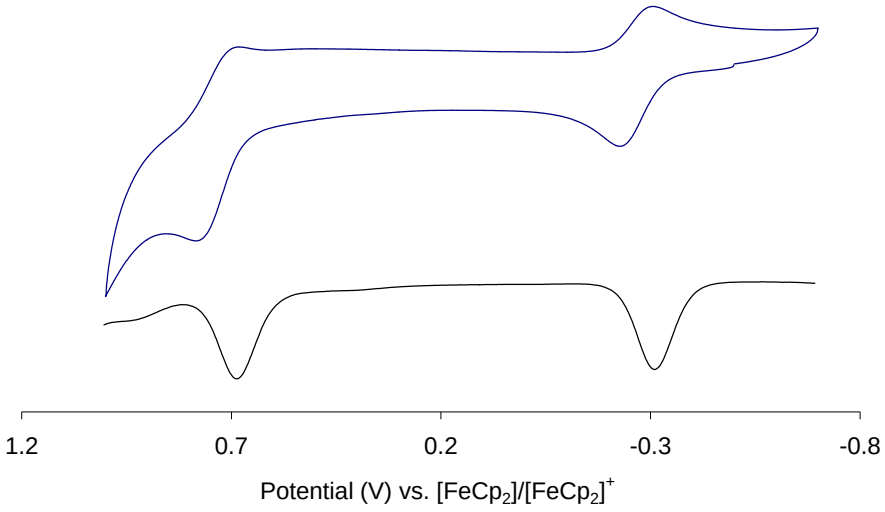

Figure 11. Cyclic and DPV voltammograms of 0.1 mM **3a** in CH_2Cl_2 (0.1 M NBu_4ClO_4) at scan rates of 0.1 $V \cdot s^{-1}$.

The cyclic voltammogram of **3a**, for example, displays two distinct one-electron redox events at potentials of –0.27 and 0.73 V [$E_{1/2} = (E_{pa} + E_{pc})/2$] with respect to the $[FeCp_2]/[FeCp_2]^+$ redox couple (Figure 12). The first electron transfer is a reversible, diffusion-controlled process, whose ΔE_p values do not differ significantly for scan rates ranging from 0.05 to 0.5 $V \cdot s^{-1}$ ($\Delta E_p = E_{pa} - E_{pc}$). Because both free guanidine, $PhN{=}C(NMe_2)NHPh$, and lithium guanidinate, $Li\{PhNC(NMe_2)NPh\}$, are irreversibly oxidized at much more positive potentials (≈ 0.66 and 0.49 V, respectively), the first redox event in **3a** may be assigned to a metal-centered electron-transfer process. The second step is quasi-reversible and may be attributable to either a metal-centered or a ligand-centered process. Similar voltammograms as for **3a** were obtained for **3b**, **3c**, and **3d**, but the first redox step occurred at lower potentials, *i.e.*, –0.33 V for **3b**, –0.41 V for **3c**, and –0.43 V for **3d**, in line with the increasing electron donation from the guanidinato ligand[13] to the Ir center (**3a** < **3b** < **3c** < **3d**).

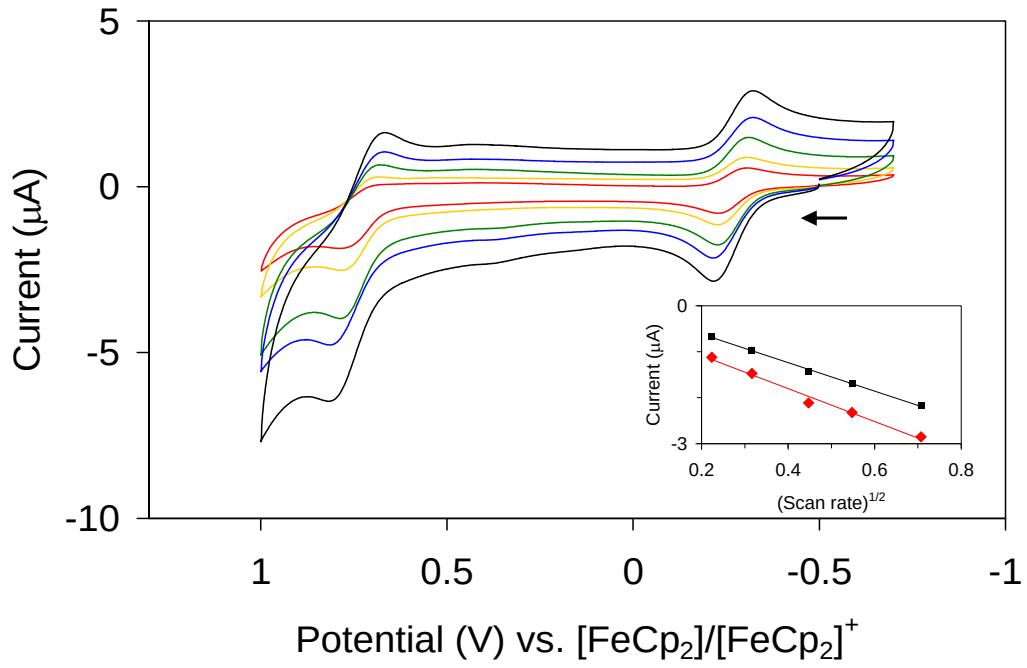

Figure 12. Cyclic voltammograms of 0.1 mM **3a** in CH_2Cl_2 (0.1 M NBu_4ClO_4) at scan rates of 0.05, 0.1, 0.2, 0.3, and 0.5 $V \cdot s^{-1}$. Inset: Plot of anodic peak current, i_{pa}, *versus* square root of scan rate for the first (■, black; $R^2 = 0.9982$) and second oxidation (◆, red; $R^2 = 0.9861$).

By comparison, the Ir^{III}/Ir^{IV} redox potentials of **3a**–**d** are significantly less positive than those of many other Ir^{III} complexes (≥ 0.21 V *vs.* $[FeCp_2]/[FeCp_2]^+$).[32,33,106] Even complexes with very electron-rich ligand sets such as cyclometalated tris(2-pyridylphenyl),[105-107] corrolato[36] and tris(dithiocarbamato) complexes (Figure 13),[108] which all provide a trianionic environment around the Ir center akin to the tris(guanidinato) complexes **3a**–**d**, exhibit higher potentials (0.07–0.91 V *vs.* $[FeCp_2]/[FeCp_2]^+$) (Table 8).

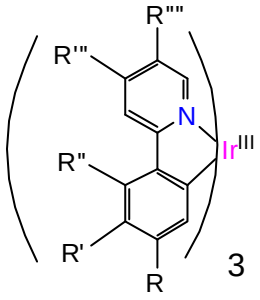

Ir-tris(2-pyridylphenyl)

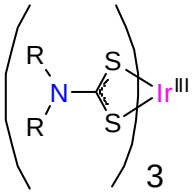

Ir-tris(dithiocarbamato)

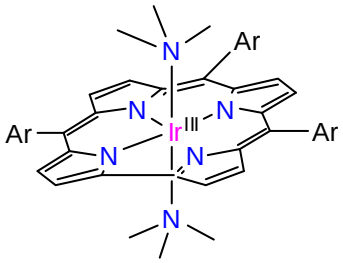

Ir-corrolato

Figure 13. Structure of Ir^{III} complexes with tris(2-pyridylphenyl), tris(dithiocarbamato), and corrolato ligand environment

Table 8. Redox potential of complexes **3a–d**, and cycloiridated tris(2-pyridylphenyl), corrolato and tris(dithiocarbamato) complexes

Complex	First redox	Second redox
3d	–0.43	0.64
3c	–0.41	0.55
3b	–0.33	0.79
3a	–0.27	0.72
$[Ir(R\text{-}ppy)_3]$	0.07–0.91	
$[Ir(R\text{-}dtc)_3]$	0.28–0.52	
$[Ir(tpfc)(NMe_3)_2]$	0.20	

[a] vs. $[FeCp_2]^{0/+}$

The effectiveness of electron-donating character from methyl substitution in *para* position of the benzene rings is higher than that of the extension of the alkyl substituents of the NR_2 group. The cyclic voltammogram shows that the second step is quasi-reversible and may be attributable to a metal-centered process (Ir^{IV}/Ir^{V}) or ligand-based

process ($Ir^{IV}/Ir^{IV+\bullet}$). If it is the Ir^{IV}/Ir^{V} process, the second redox potentials should also follow the same trend as discussed in the first redox event (**3a** > **3b** > **3c** > **3d**). However, the second redox potential follows the trend **3b** > **3a** > **3d** > **3c** which indicates the alkyl substituents in NR_2 groups may play less important role than substituents in para position of the aryl substituents in stabilization of Ir^{V} complexes. However, such doubly-oxidized species cannot be concluded whether it is a metal-center ($[[Ir^{V}L_3]$) or ligand-center ($[Ir^{IV}(L)_2(L^{\bullet+})]^{+}$) oxidation product at this point.

If comparing the two kinds of alkyl substituents, the steric interactions between the ethyl and the aryl groups would be greater than that of methyl groups, which cause the greater twisted C–N–C and N–C–N planes in the guanidinate. Therefore, with more distorted geometry, the conjugation of the C–NEt_2 *p* orbitals would be disrupted causing a decrease in π electron donation from the backbone nitrogen. Therefore the redox potentials for complexes bearing diethylamino groups may be higher than for complexes bearing dimethylamino group of guanidinato ligands.

4.3.4 Synthesis of Iridium(IV) Complexes

Chemical oxidation of **3a** in dichloromethane solution with $[FeCp_2]PF_6$ produced $[Ir\{PhNC(NMe_2)NPh\}_3]PF_6$, **4a** (Scheme 18), with absorption bands in the Vis–near-IR region [λ_{max} = 540 (ε = 2800 $M^{-1}\cdot cm^{-1}$) and 696 nm (3100)]. Except for $[FeCp_2]PF_6$, another inorganic oxidizing agent, AgOTf, was also used (Scheme 18). After adding these oxidants, the color of solution changed instantaneously from pale yellow to dark purple and associated with the formation of metallic silver precipitate when using AgOTf. The Ir^{IV} complexes were characterized by elemental analysis, ESI–MS, and UV–Vis spectroscopy.

In addition to inorganic oxidants, **3a** ($E_{1/2}$ = –0.27 V) could be oxidized by an organic oxidant, TCNE (tetracyanoethylene, $E_{1/2}$ = –0.27 V), but not TCNQ (tetracyanoquinodimethane, $E_{1/2}$ = –0.30 V).

The stability of **4a** at 20 °C and 40 °C was examined. Only 48% decay in solution at 20 °C in four weeks suggests that the Ir^{IV} complexes are relatively stable. It is worth noting that **4a** is stable at 40 °C for *ca.* 1 h.

Intrigued by the formation of stable Ir^{IV} complexes, the one pot synthesis from $[\{Ir(coe)_2\}_2(\mu\text{-}Cl)_2]$ or $[Ir\{ArNC(NR_2)NAr\}(coe)_2]$ was considered and executed. Theoretically, the Ir^{IV} complexes could be prepared by directly mixing $[\{Ir(coe)_2\}_2(\mu\text{-}Cl)_2]$ or $[Ir\{ArNC(NR_2)NAr\}(coe)_2]$ and the excess of corresponding lithium guanidiantes and oxidants, $[FeCp_2]PF_6$ or AgOTf. Unfortunately, instead of formation the desired Ir^{IV} complexes, the intractable products were observed in the mass spectroscopy.

Scheme 18. Synthesis of Ir^{IV} Compounds **4a**–**d**.

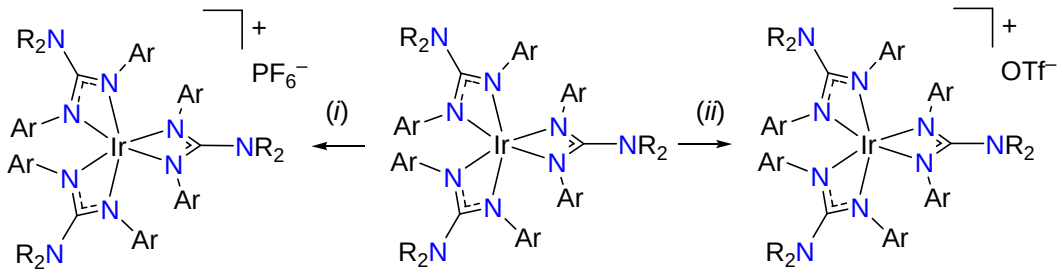

a, R = Me; Ar = Ph; **b**, R = Et; Ar = Ph; **c**, R = Me; Ar = 4-MeC_6H_4; **d**, R = Et; Ar = 4-MeC_6H_4

(*i*) 1 equiv of $[FeCp_2]PF_6$, (*ii*) 1 equiv of AgOTf

4.3.5 Spectroscopic Characterization of Iridium(IV) Complexes

As shown in Figure 14, incremental addition of $[FeCp_2]PF_6$ demonstrated that one equivalent is required for maximal formation of **4a**, and the isosbestic point in this conversion indicates that **4a** was formed directly from **3a**. On a larger scale, **4a**–**d** were generated and isolated as dark violet solids in nearly quantitative yields and analytically pure form. The complex cations, $[Ir\{ArNC(NR_2)NAr\}_3]^+$, were identified by ESI–MS. As expected for odd-electron species, the ^1H NMR spectra of **4a**–**d** are featureless.

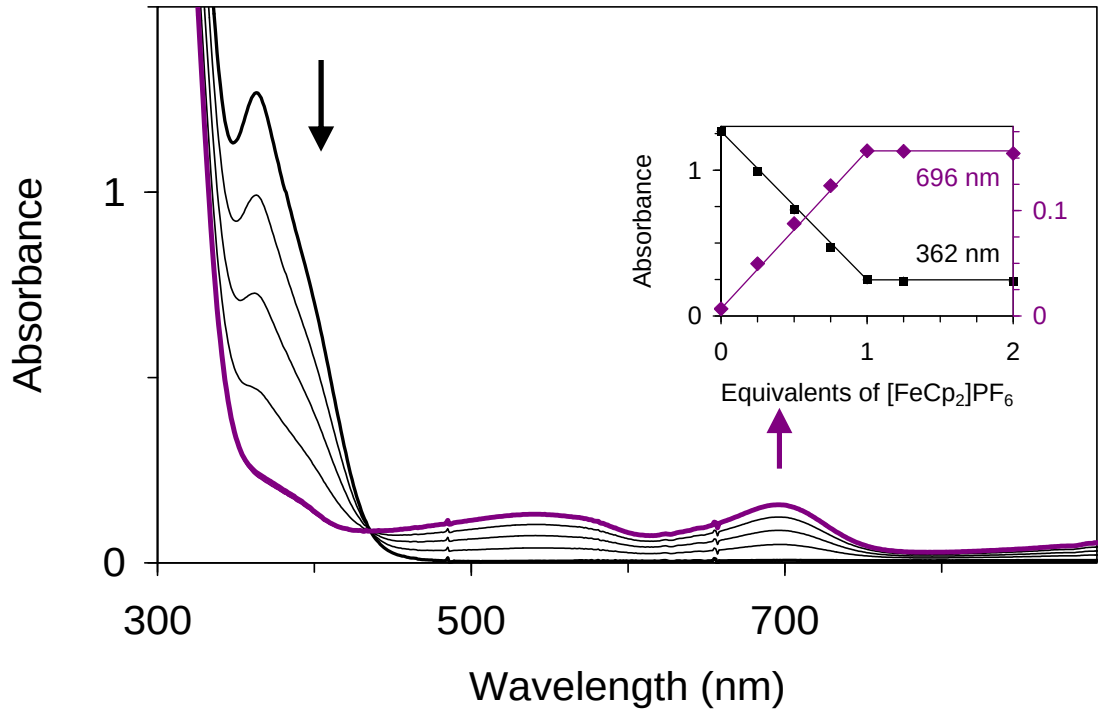

Figure 14. Oxidation of 0.1 mM **3a** (—, black) to **4a** (—, violet) in CH_2Cl_2 by addition of $[FeCp_2]PF_6$ in increments of 0.25 equiv as monitored by electronic absorption spectroscopy (pathlength, 0.5 cm). Inset: Corresponding changes of the absorbance at 362 (■, black) and 696 nm (◆, violet). Two little spikes at *ca.* 490 and 660 nm are instrumental glitches.

The electronic spectra of the Ir^{III} and Ir^{IV} complexes were recorded in dichloromethane solution in the range of 200–1100 nm (Figure 15). Ir^{III} complexes **2a–d**

show large transitions at 305 and 362–367 nm, which could be attributed to LMCT transition. **3a–d** exhibits similar features of multiple transitions in the UV–Visible and near-IR regions: 284–285, 300–310, 540–565, 692–713, and > 1000 nm. The transitions at 284–310 having large extinction coefficients are probably due to ligand-based π-π* transitions. The transitions which displayed at the visible regions 540–565 and 692–713 nm with the extinction coefficient of about 2500–3000 $cm^{-1}M^{-1}$ are too intense to be considered as *d-d* transitions. It is reasonable to assume these transitions are correlated to the electron excited from the filled ligand π orbitals to the metal *d* orbitals (Table 9). The near-IR spectra exhibit one band at 8700 cm^{-1} and two shoulders at 6400 and 5200 cm^{-1} (Figure 16).

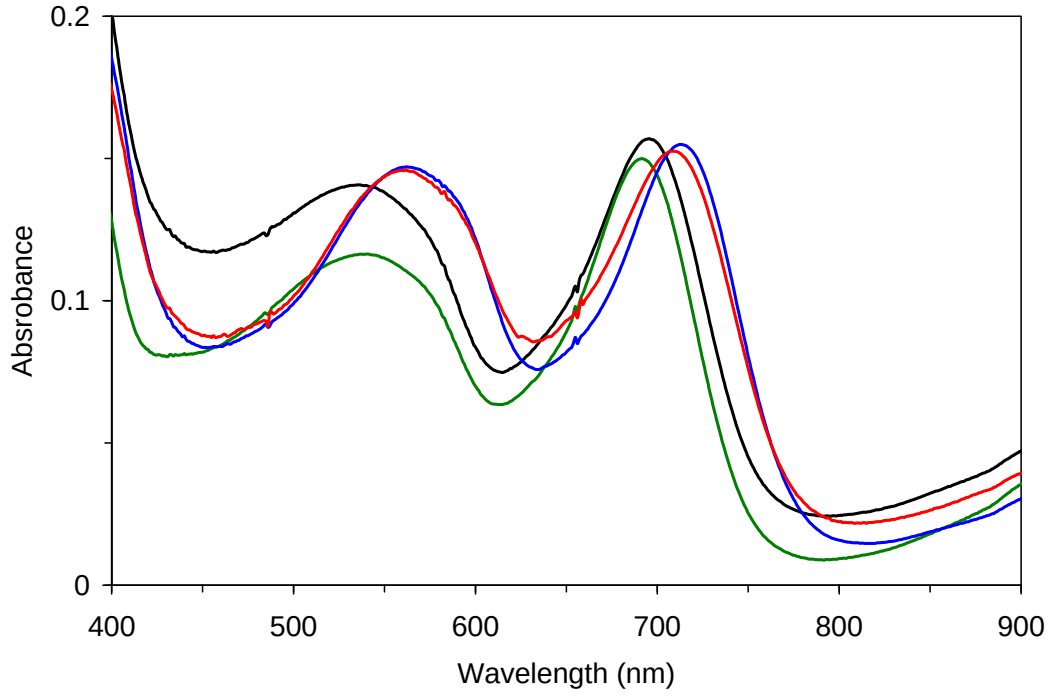

Figure 15. UV–Vis spectra of 0.1 mM of **4a** (—, black), **4b** (—, green), **4c** (—, blue), and **4d** (—, red) in CH_2Cl_2. Pathlength = 0.5 cm.

Table 9. Absorption maxima in the UV–Vis spectra of **3a–d** and **4a–d** complexes.

Ir^{III} complex	λ_{max} (nm)	Ir^{IV} complex	λ_{max} (nm)
3a	305, 362	**4a**	≈540, 696
3b	305, 363	**4b**	≈540, 692
3c	305, 365	**4c**	≈565, 713
3d	307, 367	**4d**	≈565, 706

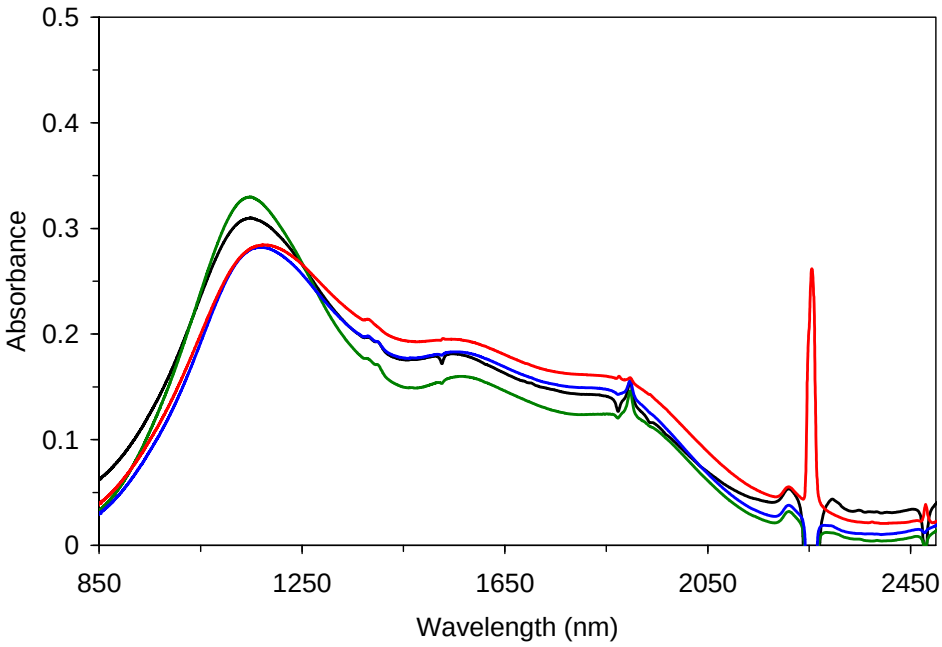

Figure 16. Near-IR spectra of 0.1 mM **4a** (—, black), **4b** (—, green), **4c** (—, blue), and **4d** (—, red) in $CDCl_3$. Pathlength = 1.0 cm. The peaks in the spectra near 1900 and 2250 cm^{-1} are due to solvent (Figure 29) absorbance in this region

For all the Ir^{IV} complexes, a distinct transition in the near-IR region was observed, and the NIR spectra were investigated (As expected, Ir^{III} complexes do not show any feature in NIR spectra, Figure 30). As shown in Figure 16, these transitions which displayed at the regions 1150 for **4a** and **4b** and 1170 nm for **4c** and **4d** with the

extinction coefficient of about 2800–3300 $cm^{-1}M^{-1}$ are too intense to be considered as *d–d* transitions. It is reasonable to assume these transitions are correlated to the charge transfer (MLCT or LMCT).

Compared to the redox potential, the trend was found that **2a–d** with stronger electron-donating substituents have higher λ_{max} than those with weaker electron-donating substituents (**2a** < **2b** < **2c** < **2d**) (Figure 17).

Moreover, the same trend (**3b** < **3a** < **3d** < **3c)** was observed in Ir^{IV}/Ir^{V} oxidation potentials and the visible regions, 692–713 nm, of the **3a–d** (Figure 17). Although the transition at 540 nm for **3a–b** is not distinguishable (likewise, 565 nm for **3c–d**), the trend, **3a–d < 3c–d**, is still noticeable.

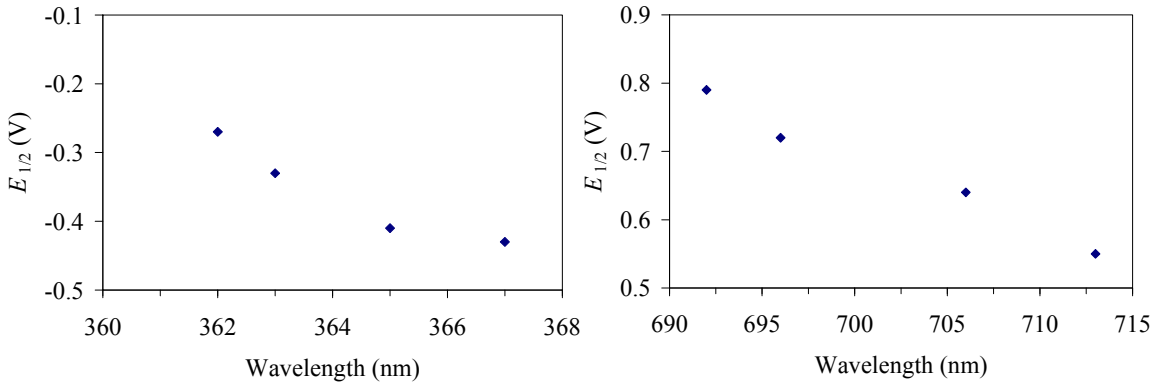

Figure 17. Plot of $E_{1/2}$ *vs.* λ_{max}. $E_{1/2}$ of Ir^{III}/Ir^{IV} *vs.* λ_{max} of **3a–d** (left), and $E_{1/2}$ of Ir^{IV}/Ir^{V} *vs.* λ_{max} of **4a–d** (right).

We mainly focus on the bands that are in the range of 1400–1600 cm^{-1} of IR spectra, where two of the three guanidinato ν_{CN} are expected to be observed. These bands of **3a–d** and **4a–d** with their tentative assignments are given in Table 10. It was found that the complexes with the same dialkylamino substituent exhibit comparable spectra, *e.g.* the dimethylamino complexes **3a** and **3c** are similar, and the diethylamino complexes **4b** and **4d** are similar. They are also similar to the corresponding $[Ir(L)(CO)_2]$ complexes

(L = guanidinato ligand).[100] In addition to ν_{CN} of the guanidinato core, the arene CC stretching and the alkyl CH deformation vibrations could also be observed in this region. The arene CC stretching vibrations appear at *ca.* 1500 and 1570–1590 cm^{-1}. The alkyl CH deformation vibrations fall in the region < 1480 cm^{-1}. Comparing Ir^{III} complexes **3a–d** to Ir^{IV} complexes **4a–d**, some changes were observed (Figure 18 and Figures 31–33). For instance, the group of bands at *ca.* 1430 cm^{-1} shifted to *ca.* 1380 cm^{-1}, and the band shown at *ca.* 1600 cm^{-1} moved to *ca.* 1570 cm^{-1}. These shifts could reflect the changes in intraligand bonding or in relative contributions of resonance structures as described in Chapter 2 (Scheme 13).

Table 10. CN and CC stretching frequencies from IR spectra of Ir^{III} and Ir^{IV} complexes

Ir^{III} complexes	$\nu_{CN} + \nu_{CC}$	ν_{CC}	ν_{CN}
3a	1594, 1575, 1553	1485	1447(sh), 1427, 1412
3b	1593, 1573, 1530	1489	1431, 1421
3c	1609, 1567, 1552	1504	1446, 1422, 1414
3d	1608, 1569, 1531	1503	1441, 1410(sh)
Ir^{IV} complexes	$\nu_{CN} + \nu_{CC}$	ν_{CC}	ν_{CN}
4a	1591, 1581, 1571	1484	1420, 1391, 1379
4b	1591, 1579, 1536	1484	1416, 1380
4c	1574, 1556	1503	1422, 1407, 1390
4d	1569(sh), 1535	1503	1415, 1381

4.3.6 Crystal Structures of Iridium(IV) Complexes

A crystallographic analysis on a single crystal of **4a**, grown by vapor diffusion of *n*-pentane into a dichloromethane solution at –30 °C, confirmed the formation of $[Ir\{PhNC(NMe_2)NPh\}_3]PF_6$ (Figure 19). Crystal and structure refinement data for **4a** are summarized in Table 5. Selected bond lengths and angles are given in Tables 6 and 7.

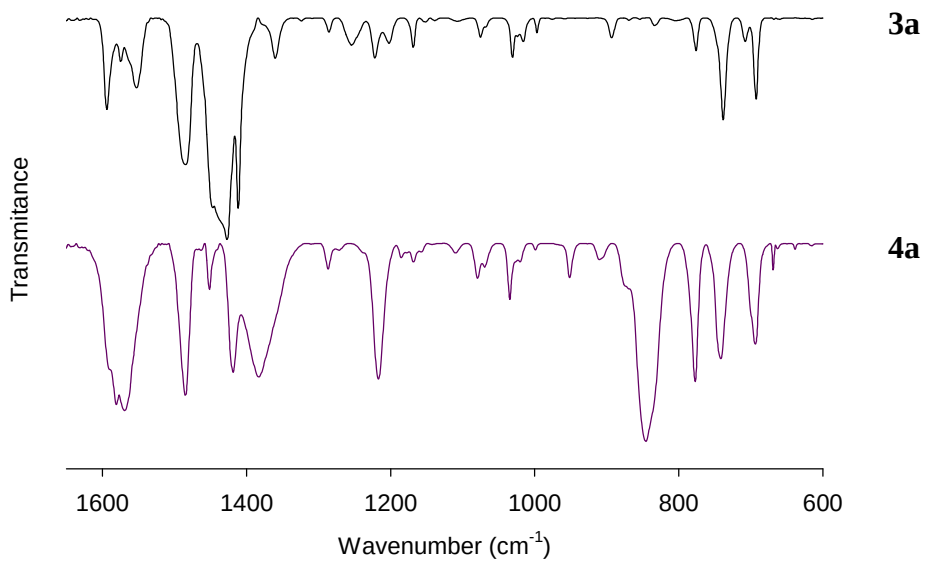

Figure 18. IR spectra of **3a** and **4a** in the range of 600–1650 nm.

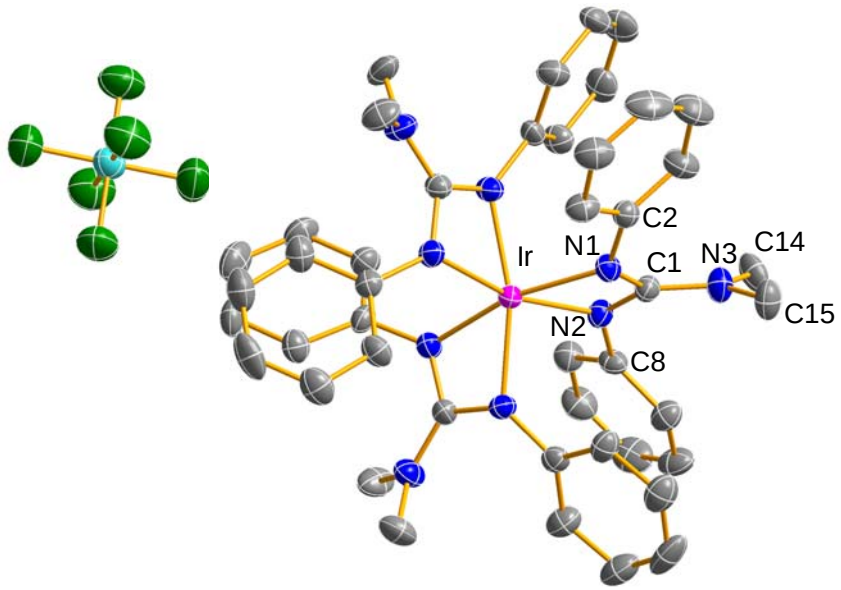

Figure 19. Molecular structure of the complex **4a**; displacement ellipsoids are drawn at the 50% probability level; hydrogen atoms have been omitted for clarity; color key: pink = Ir, blue = N, gray = C, teal = P, green = F.

According to the single crystal X-ray analysis, **4a** is monomeric in the solid state. The iridium center in **4a** is coordinated to six nitrogen atoms of the three chelating η^2-guanidinato ligands. The Ir–N distances of 2.040(3) and 2.064(3) Å agree well with those in $[IrCl_4(phen)]$.[33] The intra-ligand C–N and C–C distances are comparable to those of related guanidinato complexes of Ir^I and Ir^{III}.[60,64]

In contrast, the C–C distances in Ir^{III} semiquinonato and aminophenolato complexes display bond alternation, clearly indicating ligand radical character (Figure 20).[109,110] The crystal structure thus provides evidence for the assignment of **4a** as an Ir^{IV} rather than an Ir^{III}–ligand-radical species. In agreement with this assignment, the 77 K EPR spectrum of **4a** in frozen solution is consistent with the presence of a low-spin d^5 Ir^{IV} center. The EPR spectrum exhibits a large *g* anisotropy (g = 2.38 and 1.87) and a broad line width (peak-to-peak separation ≈ 300 G), indicative of localization of the unpaired electron predominantly in a metal-based orbital (Figure 21).

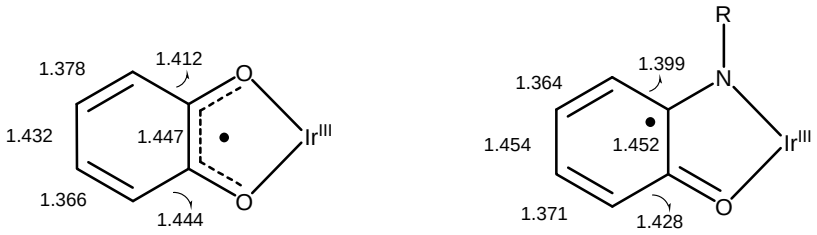

Figure 20. Structures of Ir^{III}–ligand-radical compounds

4.4 Conclusion

In summary, we have prepared and characterized rare examples of air-sensitive coordinatively saturated Ir^{III} complexes. Oxidation of these compounds led to the isolation of stable tris(guanidinato)iridium(IV) complexes, in which the Ir center is

exclusively coordinated by nitrogen-donor ligands. These results underscore the exceptional ability of the *N*,*N*-dialkyl-*N*′,*N*″-diarylguanidinate anions to stabilize transition metals in high oxidation states and suggest them as excellent ancillary ligands for new high-valent Ir complexes that may be tailored to effect useful transformations.

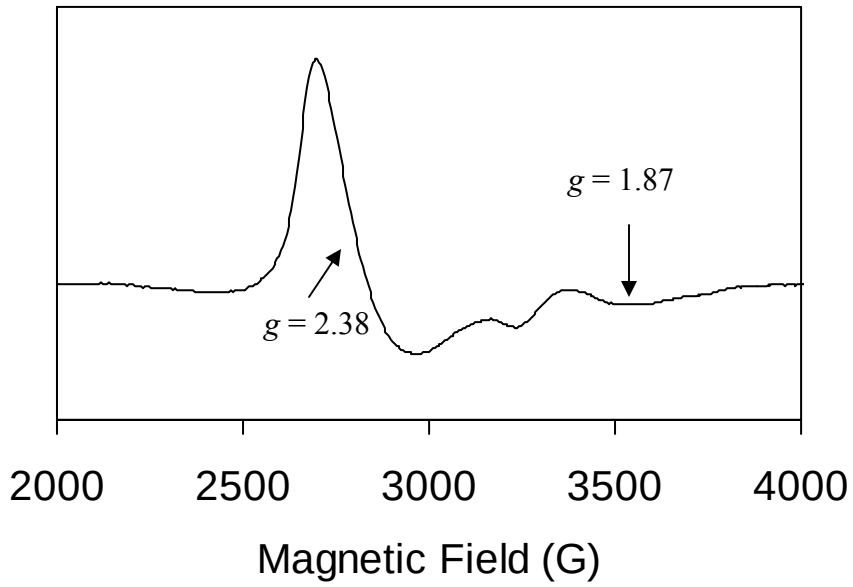

Figure 21. EPR spectrum of **4a** at 77 K

4.5 Supplemental Materials

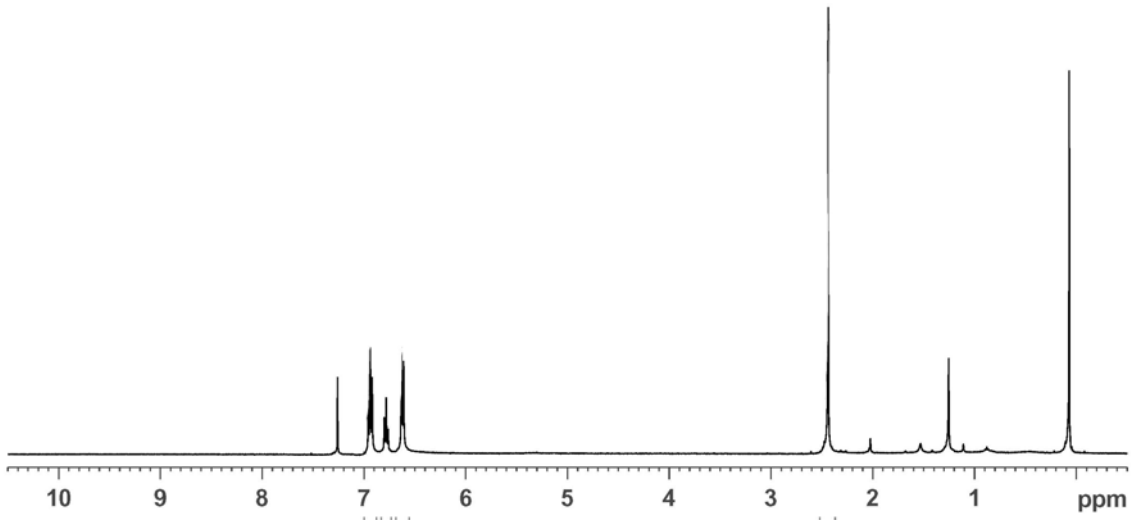

Figure 22. ^{1}H NMR spectrum of **3a**.

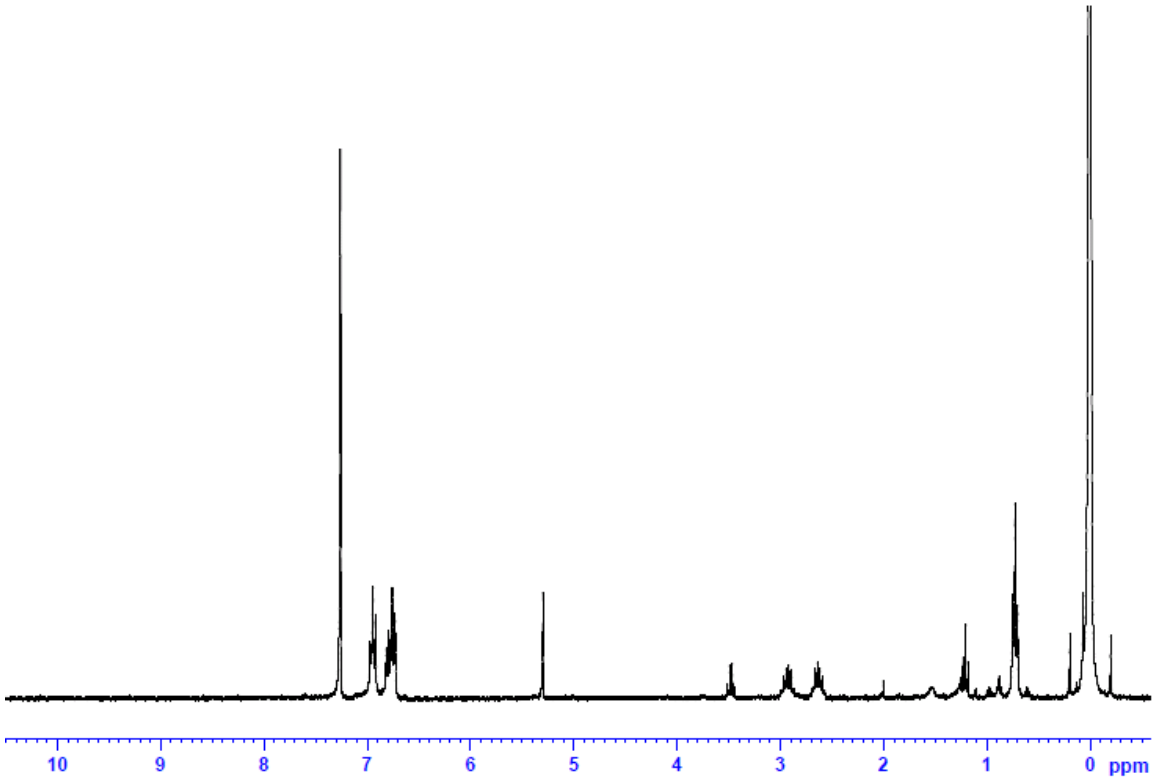

Figure 23. ^{1}H NMR spectrum of **3b**.

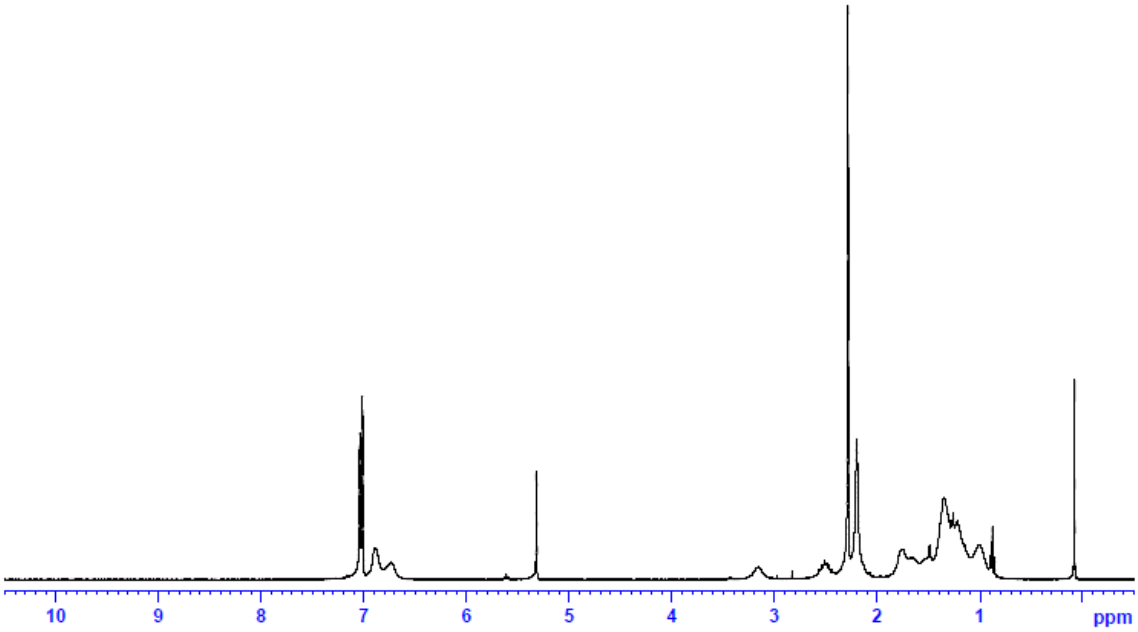

Figure 24. ^{1}H NMR spectrum of **3c**.

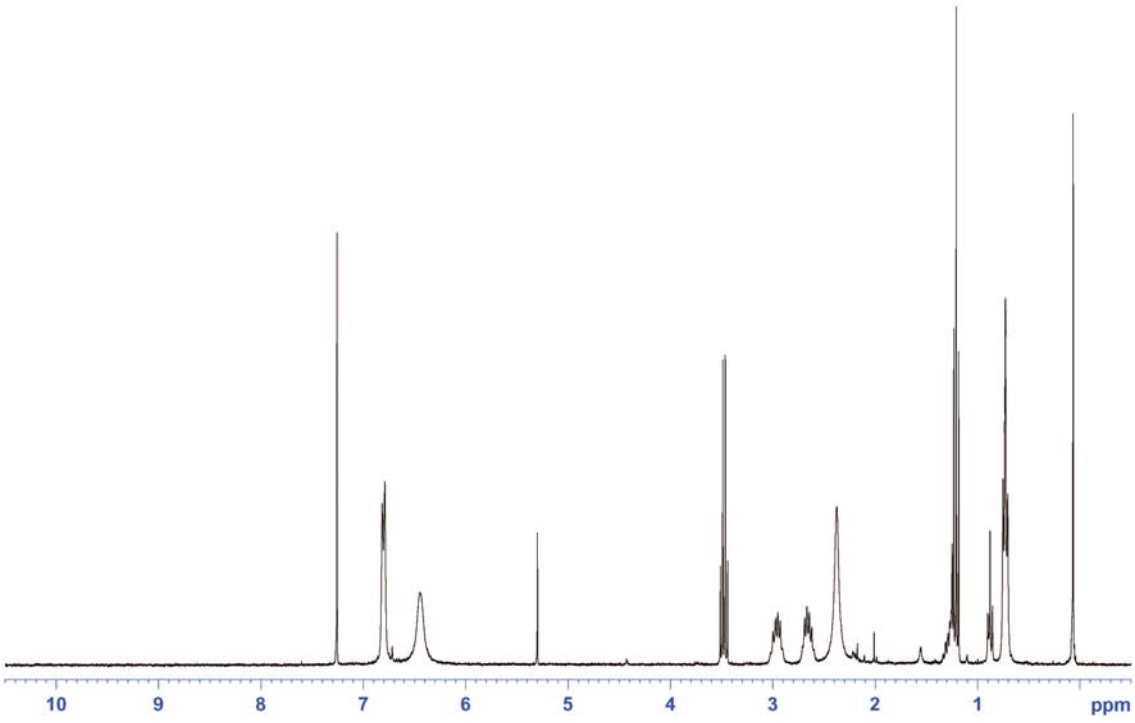

Figure 25. ^{1}H NMR spectrum of **3d**.

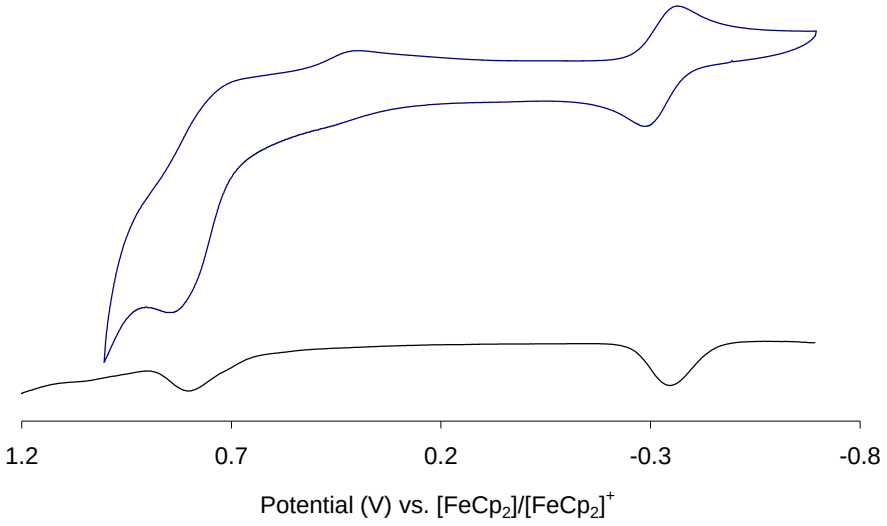

Figure 26. Cyclic and DPV voltammograms of 0.1 mM **3b** in CH_2Cl_2 (0.1 M NBu_4ClO_4) at scan rates of 0.1 $V \cdot s^{-1}$.

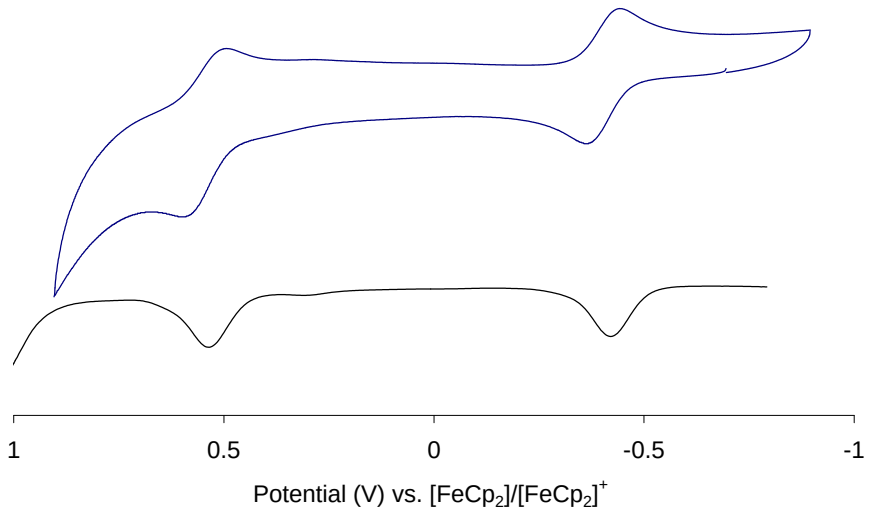

Figure 27. Cyclic and DPV voltammograms of 0.1 mM **3c** in CH_2Cl_2 (0.1 M NBu_4ClO_4) at scan rates of 0.1 $V \cdot s^{-1}$.

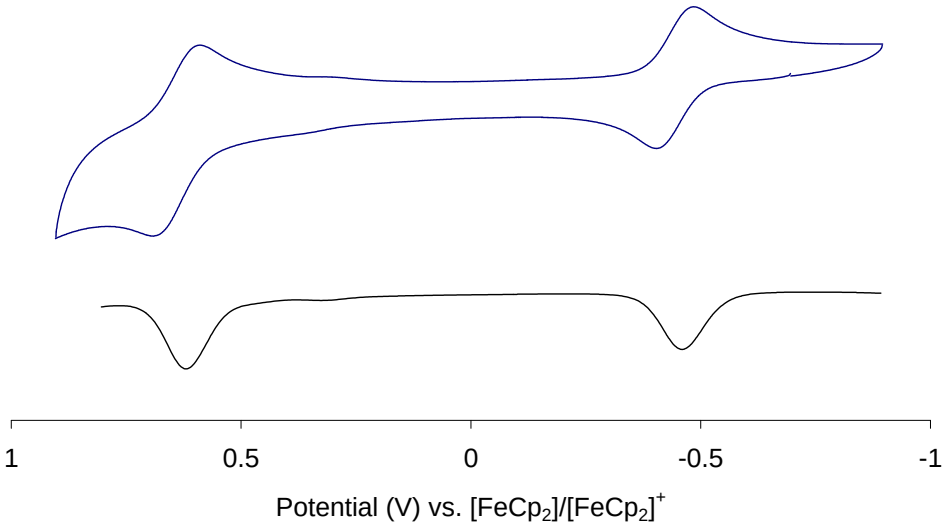

Figure 28. Cyclic and DPV voltammograms of 0.1 mM **3d** in CH_2Cl_2 (0.1 M NBu_4ClO_4) at scan rates of 0.1 $V \cdot s^{-1}$.

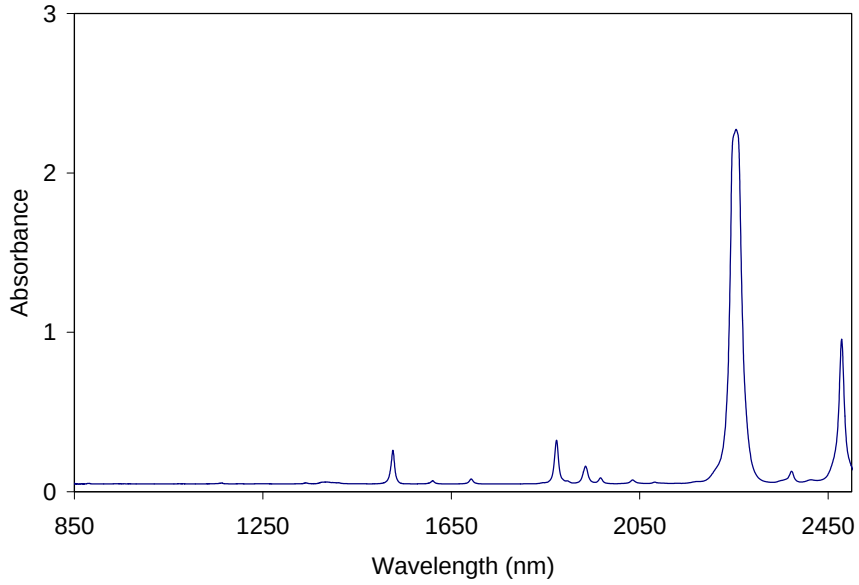

Figure 29. Near-IR spectrum of $CDCl_3$.

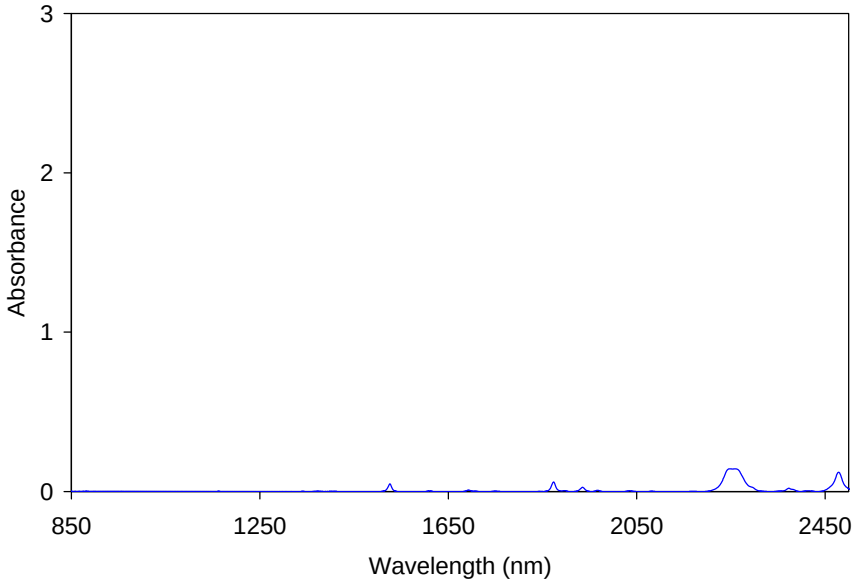

Figure 30. Near-IR spectrum of **3a**.

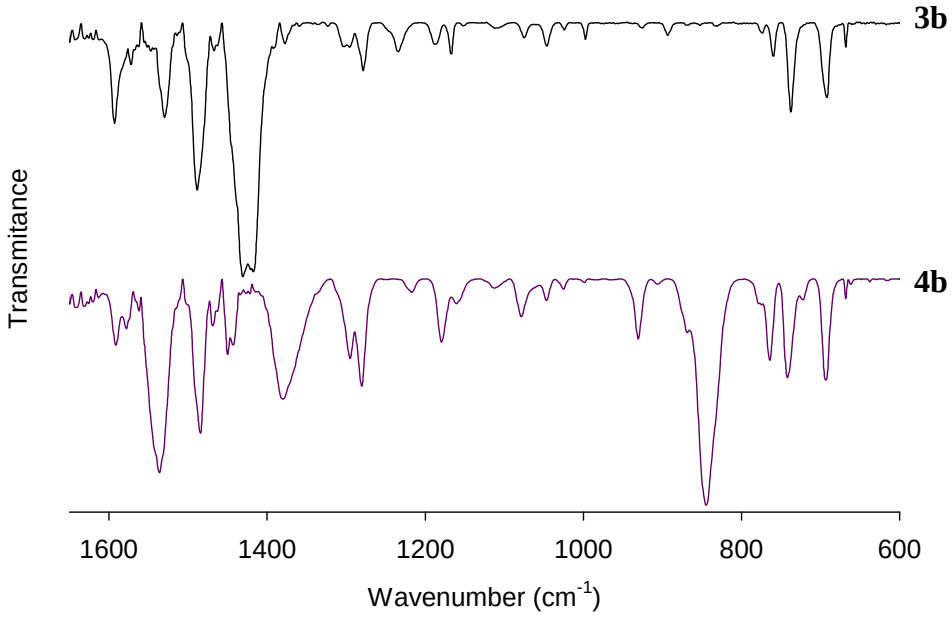

Figure 31. IR spectrum of **3b** and **4b**.

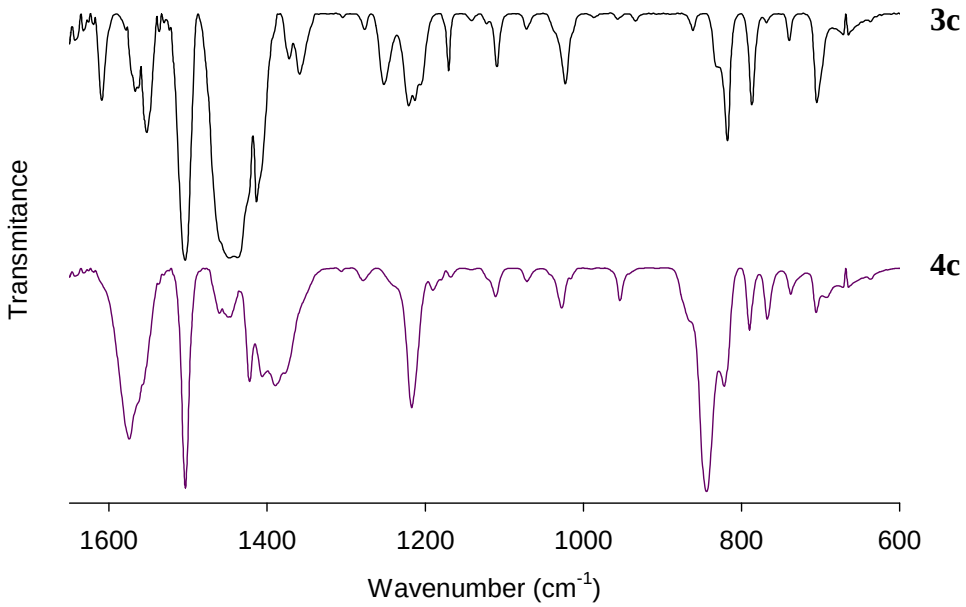

Figure 32. IR spectrum of **3c** and **4c**.

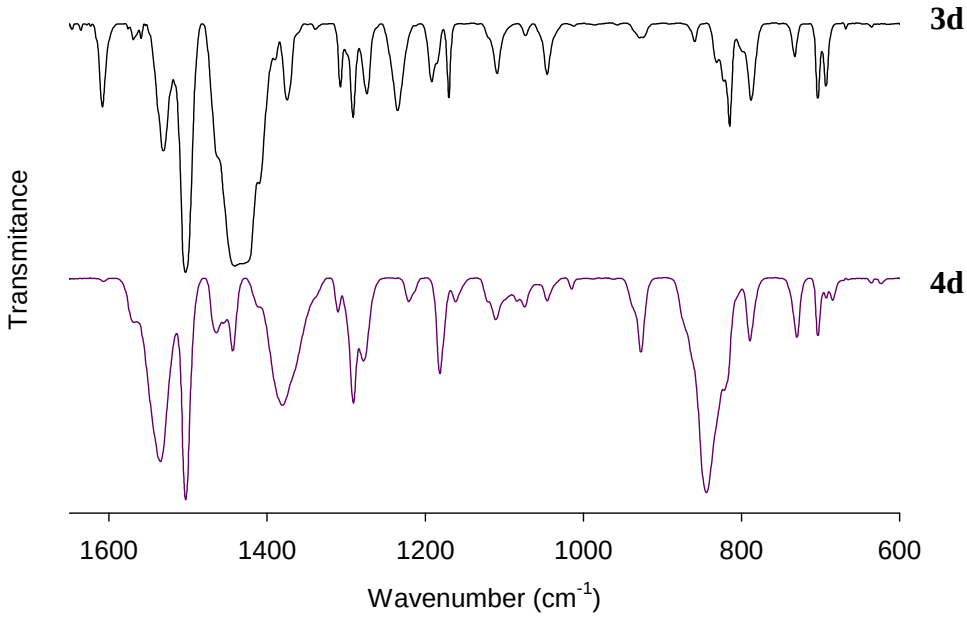

Figure 33. IR spectrum of **3d** and **4d**.

CHAPTER 5

TRIS(GUANIDINATO) COMPLEXES OF RHODIUM(III) AND RHODIUM(IV)

5.1 Introduction

Electron-rich tris(guanidinato) complexes of Rh^{III}, $[Rh\{ArNC(NR_2)NAr\}_3]$ (where R = Me or Et; Ar = Ph, 4-MeC_6H_4 or 4-$MeOC_6H_4$), were synthesized directly from $[\{Rh(coe)_2\}_2(\mu\text{-}Cl)_2]$ and the respective lithium guanidinato precursors, are air-sensitive, and can be electrochemically oxidized in two one-electron transfer steps. The first electron transfer is reversible and occurs at much lower potentials than typical for Rh^{III}. The Rh^{III} compound $[Rh\{(4\text{-}MeOC_6H_4)NC(NMe_2)N(4\text{-}MeOC_6H_4)\}_3]$ was characterized by analytical and spectroscopic methods and a single-crystal structure determination. Chemical oxidation by ferrocinum afforded unstable, paramagnetic Rh^{IV} compounds, $[Rh\{ArNC(NR_2)NAr\}_3]PF_6$, which were characterized by analytical and spectroscopic methods.

5.2 Experimental Section

Materials. All reagents and solvents were purchased from commercial sources and were used as received, unless noted otherwise. Acetonitrile, dichloromethane, diethyl ether, tetrahydrofuran, and toluene were deoxygenated by sparging with N_2 and purified by passage through two packed columns of molecular sieves under an N_2 pressure (MBraun solvent purification system). *n*-Pentane was dried over Na and distilled under N_2 prior to use.[65] Preparation and handling of air- and moisture-sensitive materials were carried out under an inert gas atmosphere by using either standard Schlenk and vacuum line techniques or a glovebox. Dioxygen was dried by passage through a short column of

Drierite. $[\{Rh(coe)_2\}_2(\mu\text{-}Cl)_2]$,[66,111] $[Rh\{PhNC(Me)NPh\}_3]$,[112] $[Rh\{PhNNNAr\}_3]$,[112] and $[Fe(\eta\text{-}C_5H_4COMe)Cp]PF_6$[113] were synthesized according to a published procedure (coe = *cis*-cyclooctene). The ^1H NMR spectra of $Rh\{PhNC(Me)NPh\}_3]$ and $[Rh\{PhNNNAr\}_3]$ matched published ones. Elemental analyses were performed by Atlantic Microlab, Inc., Norcross, GA, USA.

Physical Methods. NMR spectra were recorded on a Bruker Avance DRX 400 spectrometer at ambient temperature. ^1H and ^{13}C chemical shifts are reported in parts per million (ppm) and were referenced to residual solvent peaks. Mid- and near-IR spectra were recorded on a Bruker Vertex 70 Fourier-transform IR spectrometer. Samples for the mid-IR range were prepared by grinding the solid compound with KBr and pressing the mixture into a disk. For the near-IR range, 0.1 mM solutions of the compounds in $CDCl_3$ were used. Mass spectral data were acquired on a quadrupole ion trap ThermoFinnigan LCQ Deca mass spectrometer using an electrospray ionization source or on a double-focusing magnetic-sector Micromass, Inc., Autospec mass spectrometer using an electron impact ionization source (equipped with a solids probe). UV–Visible spectra were recorded on an HP 8453A diode array spectrophotometer (Agilent Technologies) with samples maintained at low temperature using a cryostat from Unisoku Scientific Instruments, Japan. Cyclic voltammetry (CV) and differential pulse voltammetry (DPV) measurements were carried out with a CH Instruments potentiostat (Model 620C Electrochemical Analyzer) and a standard three-electrode configuration consisting of a Pt disc working electrode, a Pt wire counter electrode and an $Ag/AgNO_3$ reference electrode (0.01 M $AgNO_3$ in MeCN; supporting electrolyte, 0.1 M NBu_4ClO_4). The voltammograms were recorded on solutions of the analyte (0.1 mM) and the supporting electrolyte (0.1 M NBu_4ClO_4) in CH_2Cl_2 under an Ar atmosphere at 293 K (*Caution:* Mixtures of perchlorate salts and metal complexes are potentially explosive and should be handled with care.) Typical measurement parameters were scan rate of 0.05 to 0.5 $V \cdot s^{-1}$ for CV and a potential increment of 4 mV, an amplitude of 50 mV, and a pulse

period of 0.2 s for DPV. Potentials are reported referenced to an external $[FeCp_2]/[FeCp_2]^+$ redox system, which can be converted to the SCE scale by adding 0.48 V (SCE, aqueous saturated calomel electrode).[11,101] Potentials relative to SCE can be converted to the NHE scale by adding 0.24 V (NHE, normal hydrogen electrode).[100]

***N,N'*-Bis(4-methoxyphenyl)thiourea, $(4\text{-}MeOC_6H_4NH)_2C{=}S$.** The procedure for the synthesis was adapted from a method previously described for other diarylthioureas.[65] A solution of 2.8 mL (6.1 g, 50 mmol) of carbon disulfide, 0.44 g (13 mmol) of elemental sulfur and 6.2 g (50 mmol) of 4-methoxyaniline in 200 mL ethanol was heated under reflux for 16 h, during which a pale purple solid was formed. After the reaction mixture was cooled to room temperature, the solid was separated by filitration, washed three times with 50 mL of diethyl ether and dried *in vacuo*. Yield: 7.1 g (49%).

$(4\text{-}MeOC_6H_4)N{=}C(NMe_2)NH(4\text{-}MeOC_6H_4)$ (1e). A solution of 2.9 g (10 mol) of *N,N'*-bis(4-methoxyphenyl)thiourea and 6.3 mL (14 g, 10 mmol) of iodomethane in 60 mL methanol was heated under reflux for 2 h. After the solution was cooled to room temperature, the volatiles, including unconsumed iodomethane, were removed under reduced pressure, affording *S*-methyl-*N,N'*-bis(4-methoxyphenyl)isothiourea hydroiodide in quantitative yield (4.2 g). To a solution of this product in 25 mL of methanol was added 5.4 mL of a dimethylamine solution (5.6 M in EtOH; 30.5 mmol). The resulting solution was heated in a sealed flask for 7 h at 70 °C. (*Caution:* Due to the formation of methanethiol, which is a gas under the reaction conditions, the pressure in the flask may increase substantially. A shield should be used for protection.) The solution was then cooled to room temperature and methanthiol was carefully removed in a stream of N_2. (MeSH was trapped by routing the gas stream through concentrated HNO_3.) Upon evaporation of the solvents, *N,N'*-dimethyl-*N',N''*-bis(4-methoxyphenyl)guanidinium iodide was obtained as a pale yellow solid (4.1 g).

The salt was dissolved in 60 mL of diethyl ether and treated with 150 mL of a saturated aqueous Na_2CO_3 solution. The biphasic mixture was vigorously stirred for 1 h,

before the organic phase was separated and the volatiles were removed under reduced pressure. The crude residue was then subjected to column chromatography on silica gel using a 5% NEt_3 of acetone solution as the eluent to yield the white solid 1.95 g (65%). Anal. calcd for $C_{17}H_{21}N_3O_2$: C, 68.20; H, 7.07; N, 14.04. Anal. Calcd for $C_{17}H_{21}N_3O_2$: C, 68.20; H, 7.07; N, 14.04. Found: C, 67.73; H, 7.11; N, 13.75. ^{1}H NMR (300 MHz, $CDCl_3$, δ): 6.84–6.76 (m, 8H, Ar H), 4.82 (s, 1H, NH), 3.74 (s, 6H, $C_6H_4OCH_3$), 2.83 (s, 6H, NCH_3). $^{13}C\{^1H\}$ NMR (75.5 MHz, $CDCl_3$, δ): 155.2, 153.0, 122.1, and 114.8 (Ar), 55.6 ($C_6H_4OCH_3$), 38.3 (NCH_3). EIMS (70 eV) *m*/*z*: $M^{+\bullet}$ calcd for $C_{17}H_{21}N_3O_2$, 299.2; found, 299.4.

(4-MeOC$_6$H$_4$)N=C(NEt$_2$)NH(4-MeOC$_6$H$_4$)$_2$ (1f). A solution of 2.9 g (10 mol) of *N,N'*-bis(4-methoxyphenyl)thiourea and 6.3 mL (14 g, 10 mmol) of iodomethane in 60 mL methanol was heated under reflux for 2 h. After the solution was cooled to room temperature, the volatiles, including unconsumed iodomethane, were removed under reduced pressure, affording *S*-methyl-*N,N'*-bis(4-methoxyphenyl)isothiourea hydroiodide in quantitative yield (4.2 g). To a solution of this product in 25 mL of methanol was added 1.7 mL of a dimethylamine solution (5.6 M in EtOH; 9.52 mmol). The resulting solution was heated in a sealed flask for 7 h at 70 °C. (*Caution:* Due to the formation of methanethiol, which is a gas under the reaction conditions, the pressure in the flask may increase substantially. A shield should be used for protection.) The solution was then cooled to room temperature and methanthiol was carefully removed in a stream of N_2. (MeSH was trapped by routing the gas stream through concentrated HNO_3.) Upon evaporation of the solvents, *N,N'*-dimethyl-*N',N''*-bis(4-methoxyphenyl)guanidinium iodide was obtained as a pale yellow solid (3.3 g).

The salt was dissolved in 60 mL of diethyl ether and treated with 150 mL of a saturated aqueous Na_2CO_3 solution. The biphasic mixture was vigorously stirred for 1 h, before the organic phase was separated and the volatiles were removed under reduced pressure. The crude residue was then subjected to column chromatography on silica gel

using a 5% triethylamine of acetone solution as the eluent to yield the white solid 2.2 g (67%). Anal. calcd for $C_{19}H_{25}N_3O_2$: C, 69.70; H, 7.70; N, 12.83.

General Procedure for the Synthesis of [Rh{ArNC(NR$_2$)NAr}$_3$] Complexes. A solution of 0.40 mmol of lithium guanidinate and 0.05 mmol of $[\{Rh^I(coe)_2\}(\mu\text{-Cl})]_2$ in 5 mL of toluene was stirred at 20 °C for 30 min. Subsequently, the solution mixture was purged with O_2 under stirring at 20 °C for 10 min. The orange solution turned into a dark brown mixture. The volatiles were removed under reduced pressure. Because the [Rh{ArNC(NR$_2$)NAr}$_3$] complexes react slowly with O_2, the remaining steps were carried out in an N_2 atmosphere. The product was extracted from the residue with 30 mL of *n*-pentane. Upon storing this solution at 20 °C, a yellow precipitate was obtained within several days, which was separated by filtration and washed with 5 mL of acetonitrile. This product can be recrystallized from a saturated solution in dichloromethane by slow evaporation of the solvent at 20 °C, but recrystallization is not required to obtain pure product.

[Rh{PhNC(NMe$_2$)NPh}$_3$] (5a). Yield: 29 mg (35%). Yellow microcrystallines were obtained from slow evaporation of dilute dichloromethane solution. Anal. calcd for $C_{45}H_{48}N_9Rh$: C, 66.09; H, 5.92; N, 15.41. Found: C, 65.36; H, 5.71; N, 15.20. ^{1}H NMR (300 MHz, $CDCl_3$, δ): 6.96 (t, *J* = 7.8 Hz, 12H, Ar H), 6.78 (t, *J* = 7.4 Hz, 6H, Ar H), 6.59 (d, *J* = 7.8 Hz, 12H, Ar H), 2.34 (s, 18H, NCH_3). EIMS (70 eV) *m/z*: $M^{+\cdot}$ calcd for $C_{45}H_{48}N_9Rh$, 817.31; found, 817.2. UV−Vis (CH_2Cl_2) λ_{max}, nm (ε): 221 (59000), ~273 (36000), 336 (49000).

[Rh{PhNC(NEt$_2$)NPh}$_3$] (5b). Yield: 35 mg (39%). Yellow microcrystallines were obtained from slow evaporation of dilute dichloromethane solution. Anal. calcd for $C_{51}H_{60}N_9Rh$: C, 67.91; H, 6.70; N, 13.98. Found: C, 67.58; H, 6.31; N, 13.72. ^{1}H NMR (300 MHz, $CDCl_3$, δ): 6.96 (t, *J* = 7.7 Hz, 12H, Ar H), 6.79 (t, *J* = 7.4 Hz, 6H, Ar H), 6.70 (d, *J* = 7.8 Hz, 12H, Ar H), 2.88 (m, 6H, NC*H*$_2$CH$_3$), 2.60 (m, 6H, NC*H*$_2$CH$_3$), 0.68

(t, J = 7.1 Hz, 18H, NCH_2CH_3). EIMS (70 eV) *m/z*: $M^{+\cdot}$ calcd for $C_{51}H_{60}N_9Rh$, 901.40; found, 901.3. UV–Vis (CH_2Cl_2) λ_{max}, nm (ε): 220 (58000), ~275 (38000), 340 (54000).

[Rh{(4-MeC$_6$H$_4$)NC(NMe$_2$)N(4-MeC$_6$H$_4$)}$_3$] (5c). Yield: 34 mg (38%). Yellow microcrystallines were obtained from slow evaporation of dilute dichloromethane solution. Anal. calcd for $C_{51}H_{60}N_9Rh$: C, 67.91; H, 6.70; N, 13.98. Found: C, 67.51; H, 6.67; N, 13.83. ^{1}H NMR (300 MHz, $CDCl_3$, δ): 6.75 (d, J = 8.4 Hz, 12H, Ar H), 6.51 (d, J = 8.2 Hz, 12H, Ar H), 2.32 (s, 18H, NCH_3), 2.20 (s, 18H, $ArCH_3$). EIMS (70 eV) *m/z*: $M^{+\cdot}$ calcd for $C_{51}H_{60}N_9Rh$, 901.40; found, 901.3. UV–Vis (CH_2Cl_2) λ_{max}, nm (ε): 220 (53000), 275 (38000), 338 (40000).

[Rh{(4-MeC$_6$H$_4$)NC(NEt$_2$)N(4-MeC$_6$H$_4$)}$_3$] (5d). Yield: 34 mg (34%). Yellow microcrystallines were obtained from slow evaporation of dilute dichloromethane solution. Anal. calcd for $C_{57}H_{72}N_9Rh$: C, 69.42; H, 7.36; N, 12.78. Found: C, 69.16; H, 7.36; N, 12.57. ^{1}H NMR (300 MHz, $CDCl_3$, δ): 6.76 (d, J = 8.2 Hz, 12H, Ar H), 6.61 (d, J = 8.3 Hz, 12H, Ar H), 2.89 (m, 6H, NCH_2CH_3), 2.58 (m, 6H, NCH_2CH_3), 2.19 (s, 18H, $ArCH_3$), 0.67 (t, J = 7.1 Hz, 18H, NCH_2CH_3). ^{13}C{^{1}H} NMR (75 MHz, $CDCl_3$, δ): 159.6 (*C*N3), 144.2, 128.6, 128.0, and 123.3 (Ar), 40.7 (NCH_2CH_3), 20.9 ($ArCH_3$), 12.3 (NCH_2CH_3). EIMS (70 eV) *m/z*: $M^{+\cdot}$ calcd for $C_{57}H_{72}N_9Rh$, 985.50; found, 985.4. UV–Vis (CH_2Cl_2) λ_{max}, nm (ε): 219 (53000), ~276 (35000), 342 (44000).

[Rh{(4-MeOC$_6$H$_4$)NC(NMe$_2$)N(4-MeOC$_6$H$_4$)}$_3$] (5e). Yield: 37 mg (37%). Yellow microcrystallines were obtained from slow evaporation of dilute dichloromethane solution. Anal. calcd for $C_{51}H_{60}N_9O_6Rh$: C, 61.38; H, 6.06; N, 12.63. Found: C, 62.01; H, 6.16; N, 12.92. ^{1}H NMR (300 MHz, $CDCl_3$, δ): 6.56 (m, 24H, Ar H), 3.73 (s, 18H, OCH_3), 2.33 (s, 18H, NCH_3). ^{13}C{^{1}H} NMR (75.5 MHz, $CDCl_3$, δ): 161.5 (*C*N3), 153.3, 140.3, 124.0, and 113.0 (Ar), 55.6 (OCH_3), 37.7 (NCH_3). EIMS (70 eV) *m/z*: $M^{+\cdot}$ calcd for $C_{51}H_{60}N_9O_6Rh$, 997.37; found, 997.3. UV–Vis (CH_2Cl_2) λ_{max}, nm (ε): 220 (57000), ~280 (48000), ~309 (49000).

[Rh{(4-MeOC$_6$H$_4$)NC(NEt$_2$)N(4-MeOC$_6$H$_4$)}$_3$] (5f). Yield: 35 mg (32%). Yellow microcrystallines were obtained from slow evaporation of dilute dichloromethane solution. Anal. calcd for $C_{57}H_{72}N_9O_6Rh$: C, 63.26; H, 6.71; N, 11.65. Found: C, 64.04; H, 7.00; N, 12.05. ^{1}H NMR (300 MHz, $CDCl_3$, δ): 6.66 (d, *J* = 8.9 Hz, 12H, Ar H), 6.57 (d, *J* = 9.0 Hz, 12H, Ar H), 3.72 (s, 18 H, OCH_3), 2.89 (m, 6H, NCH_2CH_3), 2.60 (m, 6H, NCH_2CH_3), 0.67 (t, *J* = 7.0 Hz, 18H, NCH_2CH_3). $^{13}C\{^1H\}$ NMR (75 MHz, $CDCl_3$, *δ*): 159.6 (*C*N3), 153.2, 140.4, 124.0, and 113.9 (Ar), 55.5 (OCH_3), 40.7 (NCH_2CH_3), 12.7 (NCH_2CH_3). EIMS (70 eV) *m/z*: $M^{+\cdot}$ calcd for $C_{57}H_{72}N_9O_6Rh$, 1081.47; found, 1081.4. UV–Vis (CH_2Cl_2) λ_{max}, nm (ε): 220 (67000), ~280 (47000), ~316 (56000).

General Procedure for the Synthesis of [Rh{(4-MeOC$_6$H$_4$)NC(NR$_2$)N(4-MeOC$_6$H$_4$)}$_3$]PF$_6$. In an N_2 atmosphere, a solution of 6.6 mg (0.020 mmol) of ferrocenium hexafluorophosphate in 1 mL of acetonitrile was added to a solution of 0.020 mmol of [Rh{(4-OMeC$_6$H$_4$)NC(NR$_2$)N(4-OMeC$_6$H$_4$)}$_3$] in 5 mL of dichloromethane at –30 °C. The reaction mixture immediately turned into a dark green solution, which was stirred for 1 h. The solution was concentrated to a volume of 2 mL, and 8 mL of diethyl ether was added, causing the formation of a green precipitate. The precipitate was separated by filtration and dissolved in 10 mL of acetonitrile. This solution was filtered to remove any trace amount of unreacted [Rh{(4-OMeC$_6$H$_4$)NC(NMe$_2$)N(4-OMeC$_6$H$_4$)}$_3$]. Upon evaporation of the solvent, the product was isolated as a solid and recrystallized by vapor diffusion of *n*-pentane into a dichloromethane solution at –30 °C. Dark green to black single crystals of X-ray diffraction quality were typically obtained within several days. (It is assumed that **5a–f** were obtained as racemic mixtures of Δ-and Λ-enantiomers.)

[Rh{PhNC(NMe$_2$)NPh}$_3$]PF$_6$ (6a). ESI(+)MS (*m/z*): M^+ calcd for $C_{45}H_{48}N_9Rh$, 817.31; found, 817.72. UV–Vis (CH_2Cl_2) λ_{max}, nm: 652, 927.

[Rh{PhNC(NEt$_2$)NPh}$_3$]PF$_6$ (6b). ESI(+)MS (*m/z*): M^+ calcd for $C_{51}H_{60}N_9Rh$, 901.40; found, 901.17. UV–Vis (CH_2Cl_2) λ_{max}, nm: 653, 927.

[Rh{(4-MeC$_6$H$_4$)NC(NMe$_2$)N(4-MeC$_6$H$_4$)}$_3$]PF$_6$ (6c). ESI(+)MS (*m*/*z*): M^+ calcd for $C_{51}H_{60}N_9Rh$, 901.4; found, 901.3. UV–Vis (CH_2Cl_2) λ_{max}, nm: 677, 937.

[Rh{(4-MeC$_6$H$_4$)NC(NEt$_2$)N(4-MeC$_6$H$_4$)}$_3$]PF$_6$ (6d). ESI(+)MS (*m*/*z*): M^+ calcd for $C_{57}H_{72}N_9Rh$, 985.50; found, 985.2. UV–Vis (CH_2Cl_2) λ_{max}, nm: 678, 935.

[Rh{(4-OMeC$_6$H$_4$)NC(NMe$_2$)N(4-MeOC$_6$H$_4$)}$_3$]PF$_6$ (6e). Yield: 19 mg (83%). ESI(+)MS (*m*/*z*): M^+ calcd for $C_{51}H_{60}N_9O_6Rh$, 997.37; found, 997.40. UV–Vis (CH_2Cl_2) λ_{max}, nm (ε): 717 (6400), 970 (3600).

[Rh{(4-OMeC$_6$H$_4$)NC(NEt$_2$)N(4-MeOC$_6$H$_4$)}$_3$]PF$_6$ (6f). Yield: 22 mg (89%). ESI(+)MS (*m*/*z*): M^+ calcd for $C_{57}H_{72}N_9O_6Rh$, 1081.47; found, 1081.16. UV–Vis (CH_2Cl_2) λ_{max}, nm (ε): 722 (6400), 966 (3800).

Stock solution of [Fe(η-C$_5$H$_4$COMe)Cp]PF$_6$. 5 mM of [Fe(η-C_5H_4COMe)Cp]PF_6[113] (9.3 mg, 0.025 mmol) in 5 mL MeCN was prepared. The solution must be kept under exclusion of moisture.

X-ray Crystallographic Analysis. A single crystal of **5e** was coated with Paratone N oil and mounted on a glass capillary for data collection at 150(2) K on a Nonius KappaCCD diffractometer using Mo *Kα* radiation (graphite monochromator). The temperature was controlled by an Oxford Cryostream Cooler (700 series, N_2 gas). Data collection, data reduction, and absorption correction were carried out following standard CCD techniques using the software packages Collect and HKL-2000.[69,70] Final cell constants were calculated from 12400 reflections from the complete data set. The space group *P*–1 was determined based on systematic absences and intensity statistics. The structure was solved by direct methods and refined by full-matrix least-squares minimization and difference Fourier methods (SHELXTL v.6.12).[71,72] All non-hydrogen atoms were refined with anisotropic displacement parameters. All hydrogen atoms were placed in ideal positions and refined as riding atoms with relative isotropic displacement parameters. The final full-matrix least-squares refinement *R* indices were *R*1 = 0.0744

and $wR2$ = 0.1065 (F^2, all data). Table 11 contains additional crystal and refinement information. Selected distances and angles are summarized in Tables 12 and 13.

5.3 Results and Discussion

5.3.1 Synthesis of Rhodium(III) Complexes

In this chapter, two new stronger electron-releasing guanidinato ligands, **1e** and **1f**, will be introduced. Since di-(*p*-methoxyphenyl)thiourea is not commercial available, it was synthesized by reaction of *p*-methoxyaniline with carbon disulfide according to a procedure from literature.[114] The Rh^{III} complexes [Rh{ArNC(NR_2)NAr}$_3$]; where R = Me, Ar = Ph **(5a)**; R = Et, Ar = Ph **(5b)**; R = Me, Ar = 4-MeC_6H_4 **(5c)**; R = Et, Ar = 4-MeC_6H_4 **(5d)**; R = Me, Ar = 4-$MeOC_6H_4$ **(5e)**; R = Et, Ar = 4-$MeOC_6H_4$ **(5f)**; were synthesized by the one-pot method which involved mixing [{Rh(coe)$_2$}$_2$(μ-Cl)$_2$] with the appropriate lithium guanidinates and dioxygen according to literature methods (Scheme 19).[99] The yields were similar to those of their Ir^{III} counterparts. While *p*-methoxyphenyl derivatives could not be synthesized for Ir, this was successful for Rh (**5e** and **5f**). The presence of methoxy substituents led to a dramatic improvement of the soulability in CH_2Cl_2. The Rh^{III} complexes were characterized by elemental analysis, EI–MS, ^{1}H NMR and UV−Vis spectroscopy. The ^{1}H resonance of the Rh^{III} complexes are shifted upfield compared to those of all groups of protons in the corresponding neutral guanidines. In addition, compared to Ir complexes, the NR_2 protons are more upfield shifted.

Table 11. Crystallographic data and structure refinement for [Rh{(4-$MeOC_6H_4$)NC(NMe_2)N(4-$MeOC_6H_4$)}$_3$], **5e**.

Empirical formula	$C_{51}H_{60}N_9O_6Rh$
Formula weight	997.99
Crystal habit, color	rod, orange yellow
Crystal size	0.24 x 0.09 x 0.07 mm^3
Temperature, T	150(2) K
Wavelength, λ	0.71073 Å
Crystal system	triclinic
Space group	P–1
Unit cell dimensions	a = 13.6403(15) Å
	b = 13.8538(15) Å
	c = 16.2334(17) Å
	α = 66.115(5)°
	β = 78.793(5)°
	γ = 60.767(5)°
Volume, V	2447.7(5) $Å^3$
Z	2
Calculated density	1.354 $Mg \cdot m^{-3}$
Absorption coefficient, μ	0.407 mm^{-1}
F(000)	1044
θ range for data collection	2.94 to 29.07°
Limiting indices	$-18 \le h \le 18$, $-18 \le k \le 18$, $-22 \le l \le 22$
Reflections collected / unique	23366 / 13040 [R(int) = 0.0388]
Completeness to θ	99.6% (θ = 29.07°)
Max. and min. transmission	0.9720 and 0.9086
Refinement method	Full-matrix least-squares on F^2
Data / restraints / parameters	13040 / 80 / 690
Goodness-of-fit on F^2	1.032
Final R indices [I>2sigma(I)]	R1 = 0.0442, wR2 = 0.0950
R indices (all data)	R1 = 0.0744, wR2 = 0.1065
Largest diff. peak and hole	1.224 and –0.742 $e \cdot Å^{-3}$

Table 12. Selected interatomic distances (Å) and angles (°) for [Rh{(4-$MeOC_6H_4$)NC(NMe_2)N(4-$MeOC_6H_4$)}$_3$], **5e**.

Distances (Å)		Angles (°)		Angles (°)	
Rh–N1	2.057(2)	N1–Rh–N2	64.21(8)	C18–N4–C19	128.6(2)
Rh–N2	2.071(2)	N4–Rh–N1	105.19(8)	C18–N4–Rh	93.65(15)
Rh–N4	2.050(2)	N1–Rh–N5	164.58(7)	C19–N4–Rh	132.97(17)
Rh–N5	2.062(2)	N1–Rh–N7	103.58(8)	C18–N5–C26	127.4(2)
Rh–N7	2.0629(19)	N1–Rh–N8	90.81(8)	C18–N5–Rh	92.85(15)
Rh–N8	2.066(2)	N4–Rh–N2	91.31(8)	C26–N5–Rh	126.19(16)
N1–C1	1.339(3)	N5–Rh–N2	103.56(8)	C18–N6–C33	121.6(2)
N1–C2	1.397(3)	N7–Rh–N2	164.71(8)	C18–N6–C34	121.1(2)
N2–C1	1.352(3)	N8–Rh–N2	105.56(8)	C34–N6–C33	117.0(2)
N2–C9	1.405(3)	N4–Rh–N5	64.20(8)	N4–C18–N5	109.0(2)
N3–C1	1.366(3)	N4–Rh–N7	101.19(8)	N4–C18–N6	125.5(2)
N3–C16	1.456(3)	N4–Rh–N8	160.71(8)	N5–C18–N6	125.5(2)
N3–C17	1.450(3)	N5–Rh–N7	89.91(8)		
N4–C18	1.338(3)	N5–Rh–N8	101.98(8)	C35–N7–C36	128.8(2)
N4–C19	1.400(3)	N7–Rh–N8	63.87(8)	C35–N7–Rh	93.54(14)
N5–C18	1.347(3)			C36–N7–Rh	131.56(16)
N5–C26	1.406(3)	C1–N1–C2	128.8(2)	C35–N8–C43A	131.4(4)
N6–C18	1.366(3)	C1–N1–Rh	93.73(15)	C35–N8–C43B	117.6(6)
N6–C33	1.451(3)	C2–N1–Rh	131.50(16)	C35–N8–Rh	93.23(14)
N6–C34	1.447(3)	C1–N2–C9	124.4(2)	C43A–N8–Rh	131.9(5)
N7–C35	1.336(3)	C1–N2–Rh	92.75(14)	C43B–N8–Rh	136.0(8)
N7–C36	1.398(3)	C9–N2–Rh	127.79(16)	C35–N9–C50	121.2(2)
N8–C35	1.341(3)	C1–N3–C16	121.5(2)	C35–N9–C51	121.2(2)
N8–C43A	1.387(7)	C1–N3–C17	121.9(2)	C51–N9–C50	117.6(2)
N8–C43B	1.451(11)	C17–N3–C16	115.9(2)	N7–C35–N8	109.4(2)
N9–C35	1.372(3)	N1–C1–N2	109.2(2)	N7–C35–N9	125.3(2)
N9–C50	1.445(3)	N1–C1–N3	125.2(2)	N8–C35–N9	125.3(2)
N9–C51	1.444(4)	N2–C1–N3	125.6(2)		

[a] Numbers in parentheses are standard uncertainties in the last significant figures. Atoms are labeled as indicated in Figure 14.

Table 13. Selected dihedral angles (°) for [Rh{(4-$MeOC_6H_4$)NC(NMe_2)N(4-$MeOC_6H_4$)}$_3$], **5e**.[a]

N1–C1–N2 / N1–Ir–N2	3.3(5)
C14–N3–C15 / N1–C1–N2	30.0(5)
(N1,C1,N2,N3) / (C2→C7)[b]	41.5(1)
(N1,C1,N2,N3) / (C9→C14)[b]	51.9(1)
N4–C18–N5 / N4–Rh–N5	6.3(2)
C33–N6–C34 / N4–C18–N5	32.8(2)
(N4,C18,N5,N6) / (C19→C24)[b]	39.3(1)
(N4,C18,N5,N6) / (C26→C31)[b]	48.7(1)
N7–C35–N8 / N7–Rh–N8	0.2(2)
C50–N9–C51 / N7–C35–N8	37.2(2)
(N7,C35,N8,N9) / (C36→C41)[b]	37.1(1)
(N7,C35,N8,N9) / (C43A→C48A)[b]	39.3(2)

[a] Numbers in parentheses are standard uncertainties in the last significant figures. Atoms are labeled as indicated in Figure 14. [b] Angle between the least-squares planes of the guanidinate atoms (*e.g.*, N1, C1, N2, and N3) and the aryl ring atoms (*e.g.*, C2, C3, C4, C5, C6, and C7).

Scheme 19. Synthesis of Rh^{III} Compounds **5a**–**f**

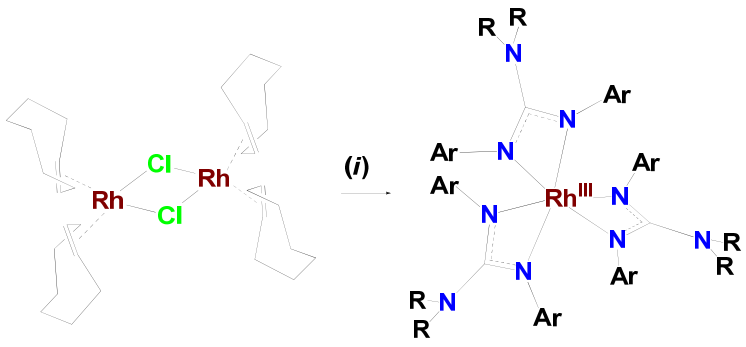

a, R = Me, Ar = Ph; **b**, R = Et, Ar = Ph; **c**, R = Me; Ar = 4-C_6H_4Me; **d**, R = Et, Ar = 4-C_6H_4Me; **e**, R = Me; Ar = 4-C_6H_4OMe; **f**, R = Et, Ar = 4-C_6H_4OMe.

(*i*) 8 equiv of Li{$ArNC(NR_2)NAr$}, O_2

5.3.2 Spectroscopic Characterization of Rhodium(III) Complexes

Complexes **5a–d** only sparsely dissolve in chlorinated solvents such as CH_2Cl_2, $CHCl_3$, and are insoluble in other common organic solvents, while complexes **5e–f** are very soluble in CH_2Cl_2. They were characterized by elemental analysis, EI–MS, ^{1}H NMR and UV–Vis spectroscopy. As was the case for Ir^{III}, the ^{1}H NMR spectra of the Rh^{III} complexes displayed a single set of resonances, indicating that the symmetric N,N'-chelating binding mode is retained in solution and consistent with coordination to a low-spin d^6 Rh^{III} center in the expected D_3 symmetric environment (Figures 37–42). Compounds **5a**–**f** were isolated as racemic mixtures (Δ- and Λ-enantiomers), and their molecular composition was established by analytical and spectroscopic methods.). In addition to aryl and methyl proton resonances, **3b** and **3d** exhibited two distinct muliplets for the protons of the diastereotopic methylene groups of the diethylamino group indicating C_3 symmetry for these two complexes in solution. The resonances of Rh^{III} complexes are shifted upfield compared to in the corresponding neutral guanidines. Owing to the methoxy group, the solubility for **5e** and **5f** increases dramatically so that ^{13}C NMR can be obtained for these two compounds.

5.3.3 Crystal Structures of Rhodium(III) Complexes

A crystallographic analysis on a single crystal of **5e**, grown by vapor diffusion of *n*-pentane into a dichloromethane solution at –30 °C, confirmed the formation of [Rh{(4-MeC_6H_4)NC(NMe_2)N(4-MeC_6H_4)}$_3$] (Figure 22). Crystal and structure refinement data for **5e** are summarized in Table 11. Selected bond lengths and angles are given in Tables 12 and 13.

According to the single crystal X-ray analysis, **5e** is monomeric in the solid state. The rhodium center in **5e** is coordinated to six nitrogen atoms of the three chelating κ^2-

guanidinato ligands. The Rh–N distances of 2.065(2) and 2.057(2) Å agree well with those in [Rh{PhNNNPh}$_3$] and [Rh{PhNC(Me)NPh}$_3$].[112] The intra-ligand C–N and C–C distances are comparable to those of related guanidinato complexes of Rh^{I}.[60] Due to the acute bite angle of the chelating guanidinato ligand (N–Rh–N, 63.89(8)–64.21(8)°), the metal center adopts a distorted octahedron coordination geometry. The structural analysis also reveals important intra-ligand parameters that provide insight into the bonding of the guanidinato ligands. The C–N distances in the planar CN_3 core of **5e** are nearly identical, 1.336(3)–1.372(3) Å. These parameters indicate a high degree of π electron delocalization over the CN_3 core, implicating a significant contribution of the iminium/diamide resonance structure (Scheme 13 in Chapter 2, Structure II). In accord with the sp^2 hybridization expected for efficient lone-pair donation into the CN_3 unit, the N3 (or N6, N9) atom adopts a trigonal-planar geometry with bond angle sums of 360(2)°. In contrast, the N1 (or N4, N7) and N2 (or N5, N8) atoms are more pyramidalized with bond angle sums of 344.9(2)–355.2(2)°.

The intra-ligand structural features of **5e** are unusual, because complexes of guanidinato(1–) ligands typically display more localized bonding with a longer C–N bond to the non-coordinated nitrogen atom and shorter ones to the metal-coordinated nitrogen atoms[60,85-94] Thus, the bonding in those guanidinate systems is best described by a relatively larger contribution of the amine/amidinate resonance structures (Scheme 13 in Chapter 2, Structure I and III). On the other hand, the greater extent of delocalization observed for **2a** is also present in complexes of Ti^{IV},[95,96] Zr^{IV},[97] and Nb^{V}.[98]

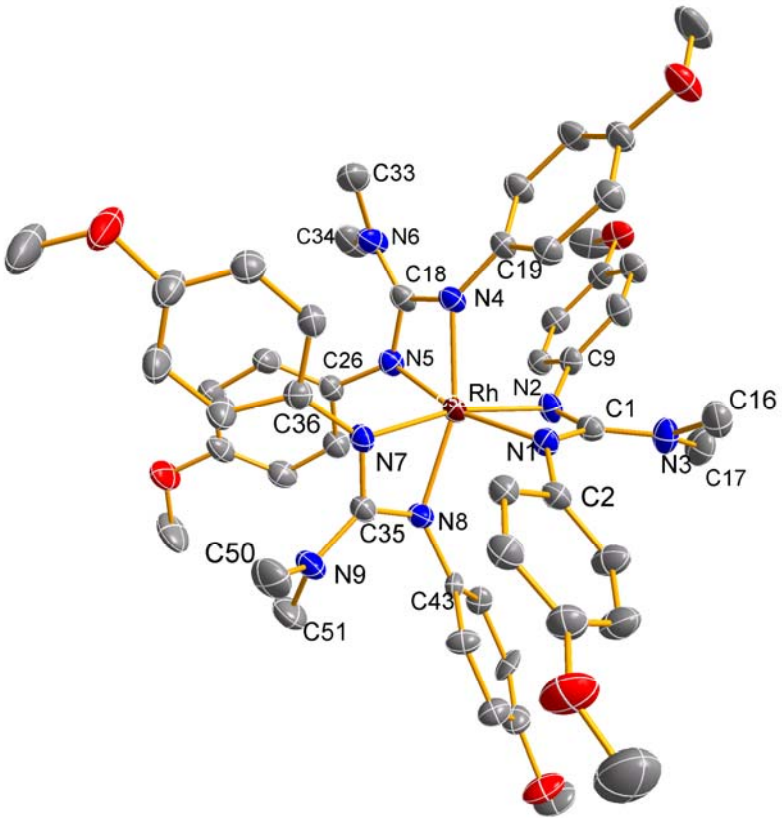

Figure 34. Molecular structure of the complex **5e**; displacement ellipsoids are drawn at the 50% probability level; hydrogen atoms have been omitted for clarity; color key: dark red = Rh, blue = N, gray = C, red = O.

5.3.4 Electrochemical Characterization of Rhodium(III) Complexes

For Rh^{III} complexes, **5a–f**, the cyclic voltammograms (CVs) and differential pulse voltammograms (DPVs) all showed that these complexes can be oxidized at unusually low potentials. The CV and DPV results are in good agreement, and no reduction processes for any complexes were observed (Figures 43–48). Electrochemical measurements for **5a–d** exhibited two one-electron oxidation processes, and three one-electron oxidation processes were found for **5e–f**. Previous studies on the Ir^{III} complexes have shown that the first redox event is reversible and the second event is quasi-reversible process. For **5a**, the reversibility of the first redox event varies with scan

window (Figure 23). For the full scan window (–2 to 2 V), two redox events were exhibited, where the first one is quasi-reversible and the second one is irreversible. However, when the scan window was narrowed down to the first redox region (–0.3 to 0.4 V), reversibility was observed. This could result from the EC mechanism. Moreover, the trends of the first redox potentials follow the electron-donating strength from the guanidinato ligand to the metal centers.

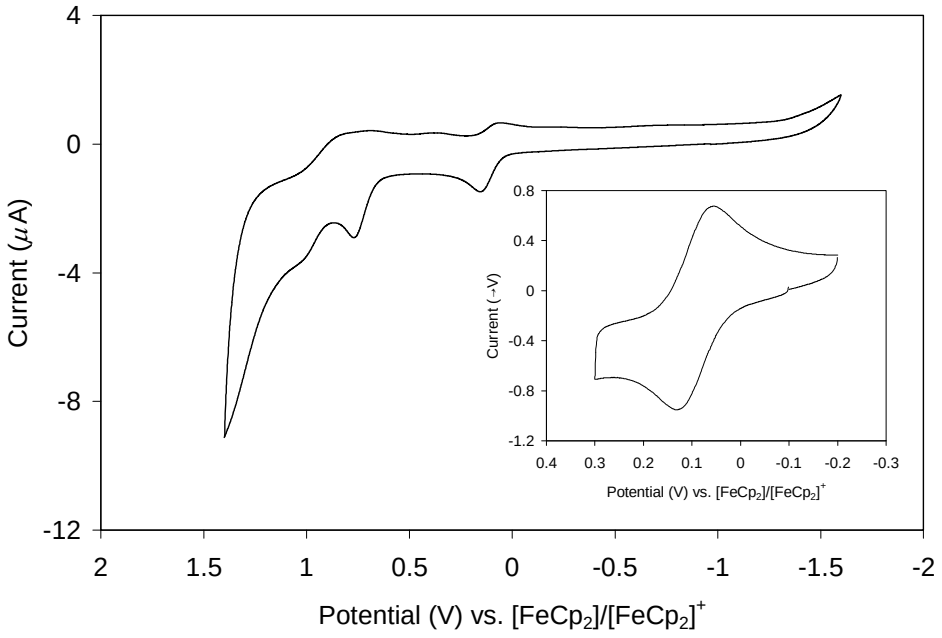

Figure 35. Cyclic voltammograms of 0.1 mM **5a** in CH_2Cl_2 (0.1 M NBu_4ClO_4) at scan rates of 0.1 $V \cdot s^{-1}$ from –2 to 2 V. Inset: Scan window from –0.3 to 0.4 V.

Compared to Ir^{III} counterparts, the first redox process of **5a–d** exhibited at higher potential (Table 14). Interestingly, if compared the electron-donating strength of both methyl and methoxy substituents in *para* position of the benzene rings and the extension of the alkyl substituents of the NR_2 group, the former has much stronger influences in terms of redox potentials than the latter. Whether the second redox events are metal or ligand based is not known at this time. The voltammograms of complexes **5e** and **5f** show three redox steps, and the irreversible electron transfer is attributable to a ligand-centered

process.

Table 14. $E_{1/2}$ of 0.1 mM M(III) Guanidinato Complexes in CH_2Cl_2 at a Scan Rate at 0.1 V/s.[a]

Ir^{IV}	Redox potential (V)	Rh^{IV}	Redox potential (V)
4a	–0.27	**6a**	0.09
4b	–0.33	**6b**	0.06
4c	–0.41	**6c**	–0.05
4d	–0.43	**6d**	–0.06
		6e	–0.12
		6f	–0.13

[a] *vs.* $[FeCp_2]/[FeCp_2]^+$

By comparison, the Rh^{III}/Rh^{IV} redox potentials of **5a**–**f** are significantly less positive than those of many other Rh^{III} complexes (Table 15) (≥ 0.53 V *vs.* $[FeCp_2]/[FeCp_2]^+$). Compared to the oxidation potential of this series of Rh^{III} analogues, replacement of an amidinate by a guanidinate would be expected to increase the electron density on the metal and reduce its oxidation potential, and, thereby, makes this class of ligands stronger donors than the closely related amidinate and triazenide anions. In addition to oxidation potential, the voltammogram of **5a** analogues, $[Rh\{PhNC(Me)NPh\}_3]$ and $[Rh(PhNNNPh)_3]$, exhibit irreversibility.

Table 15. E_{pa} of 0.1 mM **5a**, $[Rh\{PhNC(Me)NPh\}_3]$,and $[Rh(PhNNNPh)_3]$ in CH_2Cl_2 at a Scan Rate at 0.1 V/s.[a]

5a	0.13
$[Rh\{PhNC(Me)NPh\}_3]$	0.53
$[Rh(PhNNNPh)_3]$	0.89

[a] *vs.* $[FeCp_2]/[FeCp_2]^+$

5.3.5 Synthesis of Rhodium(IV) Complexes

Similar to Ir^{III} counterparts, the oxidation of **5a–f** was studied by using ferrocenium derivatives or AgOTf. Chemical oxidation of **5e** in dichloromethane solution with $[FeCp_2]PF_6$ produced $[Rh\{(4\text{-}MeOC_6H_4)NC(NMe_2)N(4\text{-}MeOC_6H_4)\}_3]PF_6$, **6e** (Scheme 20), with absorption bands in the Vis–near-IR region [λ_{max} = 714 (ε = 5200 $M^{-1}\cdot cm^{-1}$) and 983 nm (2600)]. After adding these oxidants, the color of solution changed instantaneously from pale yellow to yellow green and associated with the formation of metallic silver precipitate when using AgOTf. However, depending on different Rh^{III} complexes, the choice of ferrocenium derivatives varies, *i.e.* $[FeCp_2]PF_6$ can be used to generate **6e–f** from **5e–f**, but for **5a–d**, only $[FeCp(\eta^5\text{-}C_5H_4COCH_3)]PF_6$ is strong enough to oxidize Rh^{III} to Rh^{IV}. The Rh^{IV} complexes were characterized by ESI–MS and UV–Vis spectroscopy. Because of the instability of the Rh^{IV} complexes, elemental analysis could not be obtained.

Scheme 20. Synthesis of Rh^{IV} Compounds **6a**–**f**.

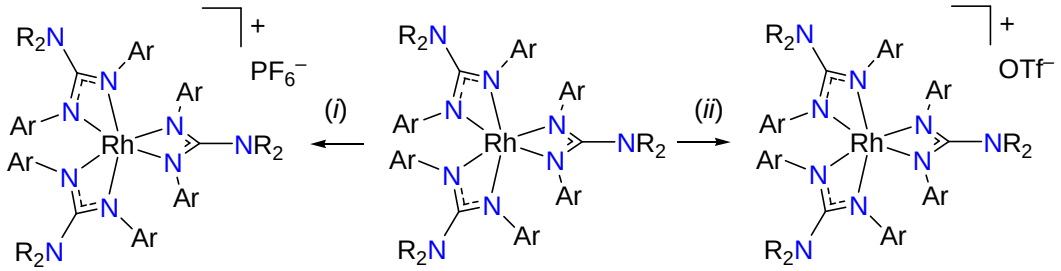

6a–f **5a–f**

a, R = Me; Ar = Ph; **b**, R = Et; Ar = Ph; **c**, R = Me; Ar = 4-MeC_6H_4; **d**, R = Et; Ar = 4-MeC_6H_4; **e**, R = Me; Ar = 4-$MeOC_6H_4$; **f**, R = Et; Ar = 4-$MeOC_6H_4$

(*i*) 1 equiv of $[FeCp_2]PF_6$ or $[FeCp(\eta^5\text{-}C_5H_4COCH_3)]PF_6$; (*ii*) 1 equiv of AgOTf

Rh^{IV} complexes **6a–f** were unstable, and their $t_{1/2}$ values were evaluated using UV−Vis spectroscopy at ambient temperature (Figure 49 and Table 16). As can be seen, the compounds with ethyl substituents are more stable than others with methyl substituents. Although the stability trend (**6f** > **6d** > **6b** > **6e** > **6c** > **6a**) does not follow the redox potential (**6f** > **6e** > **6d** > **6c** > **6b** > **6a**), the correlation between electron donating strength of guanidinato ligands and the stability of Rh^{IV} complexes can still be observed, *e.g.* all ethyl substituent complexes are more stable than all methyl ones. The possible explanation for the greater stability of the complexes with ethyl substituents could be that the metal center is better protected than that in methyl substituents.

Table 16. Redox potential (V) and Stability ($t_{1/2}$) of **6a–f** at 20 °C.

Rh^{IV}	Redox potential (V)	$t_{1/2}$ (min)
6a	0.09	15
6b	0.06	28
6c	–0.05	20
6d	–0.06	73
6e	–0.12	23
6f	–0.13	102

5.3.6 Spectroscopic Characterization

Rhodium(IV) Complexes

As shown in Figure 24, incremental addition of $[FeCp_2]PF_6$ demonstrated that one equivalent is required for maximal formation of **6e**, and the isosbestic point in this conversion indicates that **6e** was formed directly from **5e**. The complex cations, $[Rh\{ArNC(NR_2)NAr\}_3]^+$, were identified by ESI(+)–MS.

The electronic spectra of **6a–f** were recorded in dichloromethane solution in the range 200–1100 nm (Figure 49). **6a–f** exhibits similar features of multiple transitions in

the UV–Visible and near-IR regions: < 300, 652–722, 927–970 nm (Table 17). High extinction coefficients for the intense transitions < 300 nm indicate that these are most likely ligand-based π-π* transitions. The bands in the visible region 652–722 nm with extinction coefficients of about 2400–6400 $cm^{-1}M^{-1}$ are too intense to be considered as *d-d* transitions. It is reasonable to assume these transitions are correlated to the electron excited from the filled ligand π orbitals to the vacancy in the metal t_{2g} subshell. Likewise, the bands in the region of 927–970 nm with extinction coefficients of about 1800–3800 $cm^{-1}M^{-1}$ are also considered as the electron excited from the filled ligand π orbitals to the vacancy in the metal t_{2g} subshell.

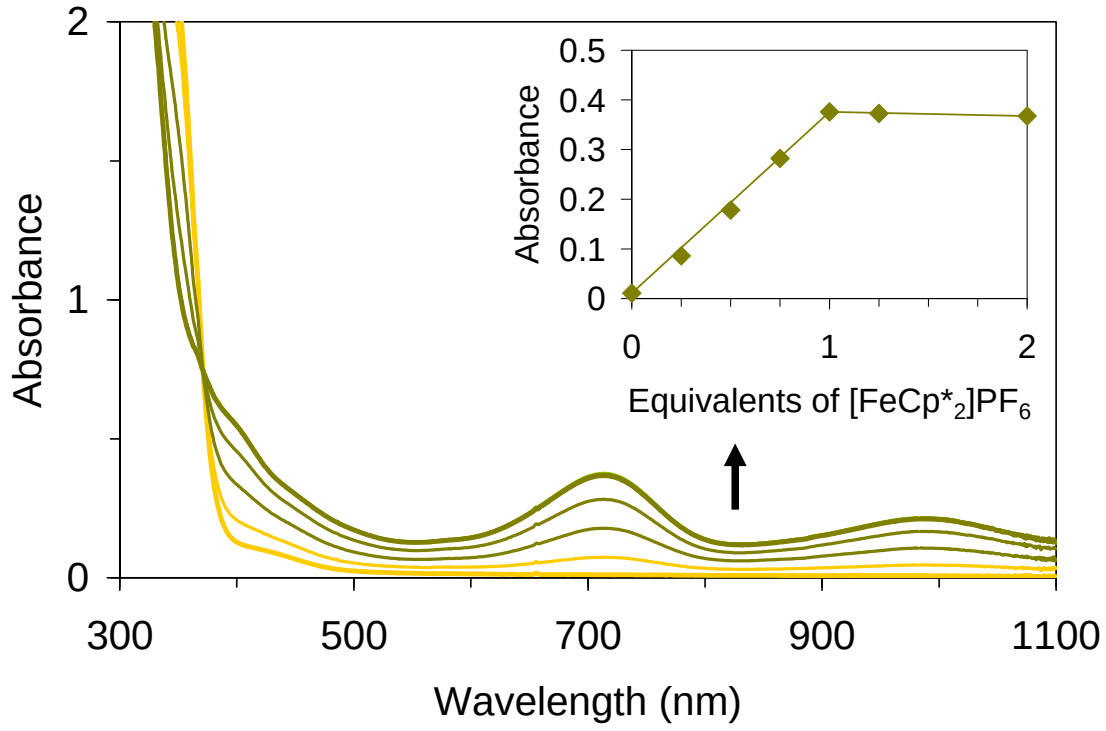

Figure 36. Oxidation of 0.1 mM **5e** (—, yellow) to **6e** (—, green) in CH_2Cl_2 by addition of $[FeCp_2]PF_6$ in increments of 0.25 equiv as monitored by electronic absorption spectroscopy (pathlength, 0.5 cm). Inset: Corresponding changes of the absorbance at 717 nm (◆, green).

Table 17. Absorption maxima in the UV−Vis-NIR spectra of **5a–f** and **6a–f** complexes.

Rh^{III} complex	λ_{max} (nm)	Rh^{IV} complex	λ_{max} (nm)
5a	273, 336	**6a**	652, 927
5b	275, 340	**6b**	653, 927
5c	275, 338	**6c**	677, 937
5d	276, 342	**6d**	678, 935
5e	280, 309	**6e**	717, 970
5f	280, 316	**6f**	722, 966

Because the Rh^{IV} complexes are thermally unstable at room temperature, only the most stable compound, **6f** was investigated by near-IR spectroscopy (NIR spectrum of **6e** observed in Figure 50 is not the spectrum of full formation resulting from low stability). As shown in Figure 50, the bands close to 970 and 1500 nm with extinction coefficients of about 2200–3500 $cm^{-1}M^{-1}$ are too intense to be considered as *d–d* transitions. It is reasonable to assume these transitions are correlated to the charge transfer (MLCT or LMCT).

5.4 Conclusion

In summary, rare examples of air-sensitive coordinatively saturated Rh^{III} complexes were prepared and characterized. Although oxidation of these compounds led to the thermally unstable Rh^{IV} complexes, all the spectroscopic methods suggest that the Rh^{IV} complexes are structurally similar to their Ir^{IV} counterparts. These results underscore the exceptional ability of the *N*,*N*-dialkyl-*N*′,*N*″-diarylguanidinate anions to stabilize transition metals in high oxidation states and suggest them as excellent ancillary ligands for new high-valent Rh complexes that may be tailored to effect useful transformations. Current efforts are directed at the identification of the even further oxidized species detected in our electrochemical studies.

5.5 Supplemental Materials

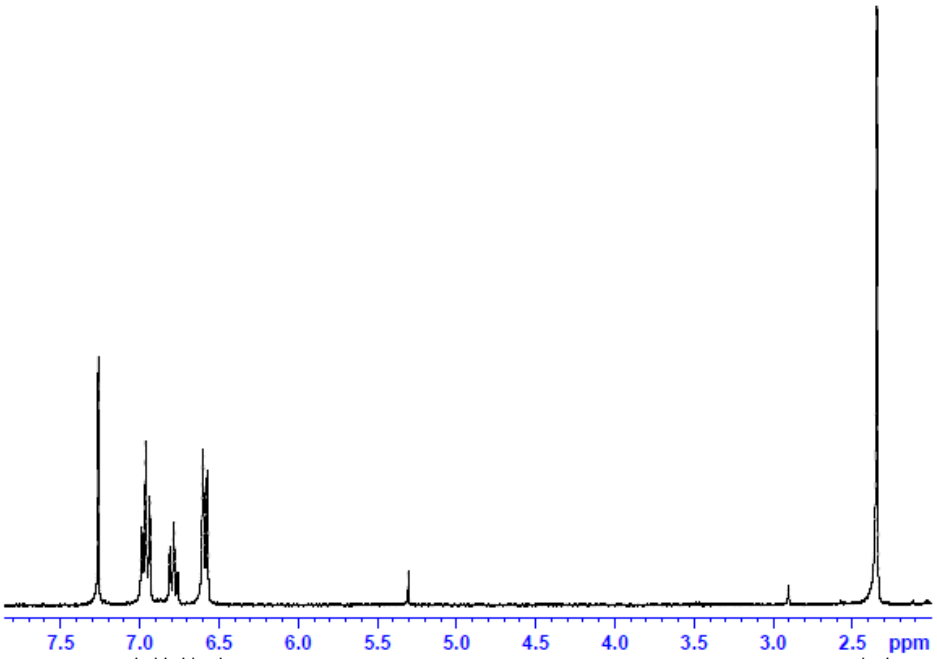

Figure 37. ^{1}H NMR spectrum of **5a**.

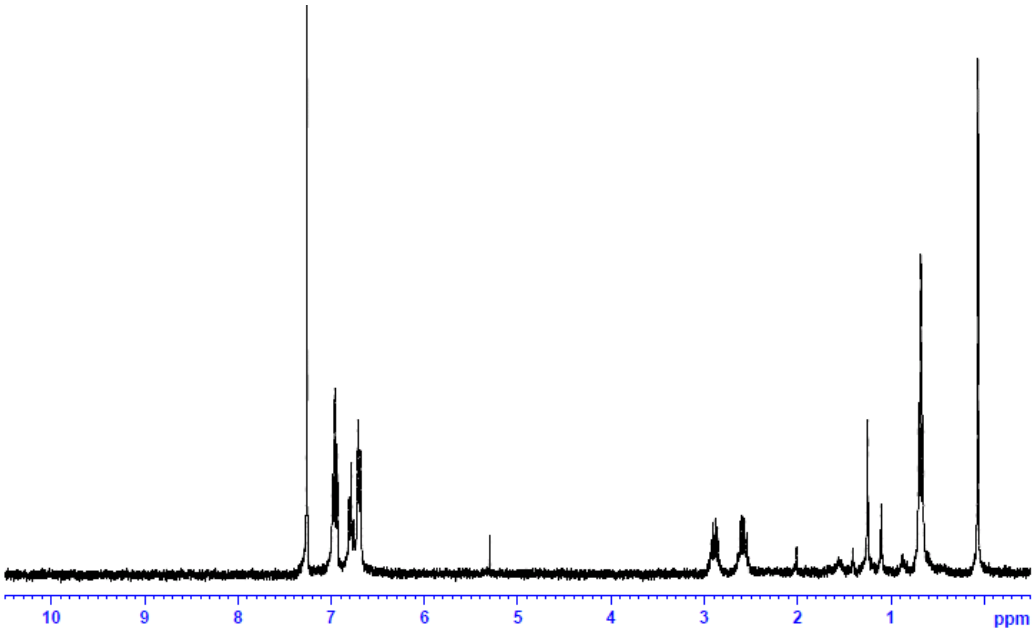

Figure 38. ^{1}H NMR spectrum of **5b**.

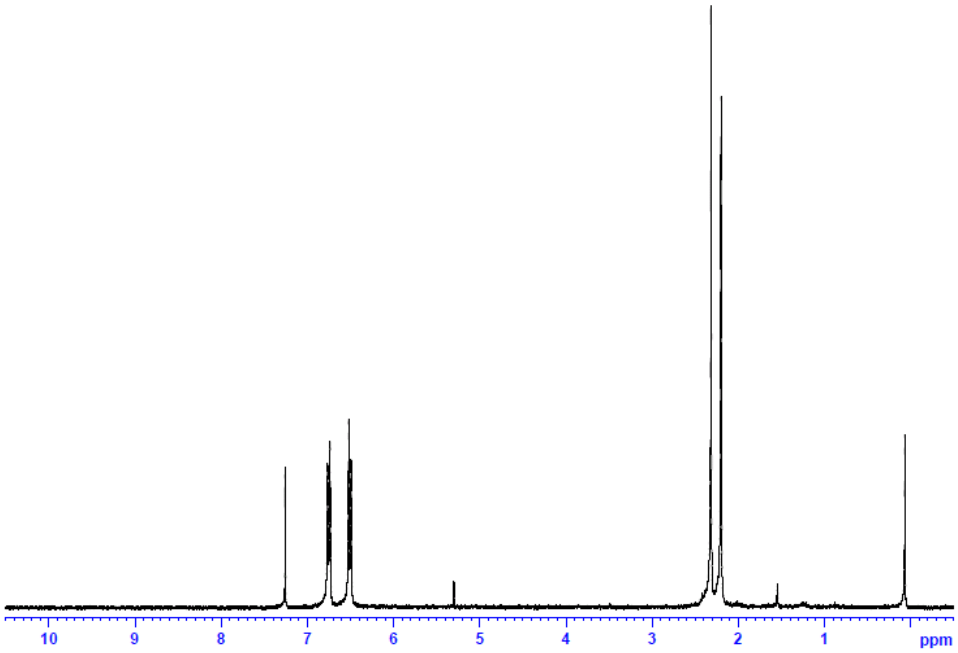

Figure 39. ^{1}H NMR spectrum of **5c**.

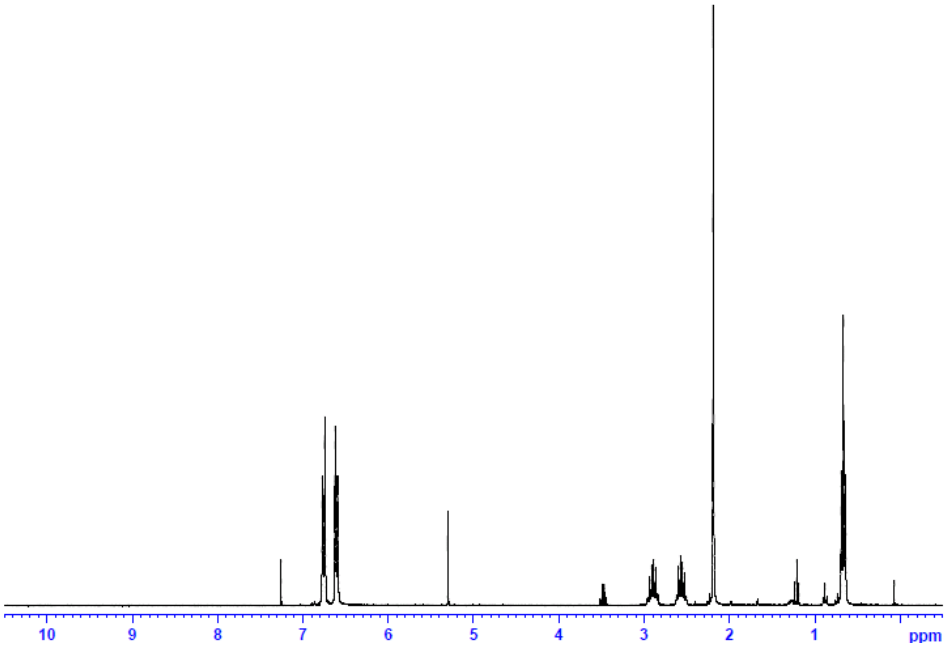

Figure 40. ^{1}H NMR spectrum of **5d**.

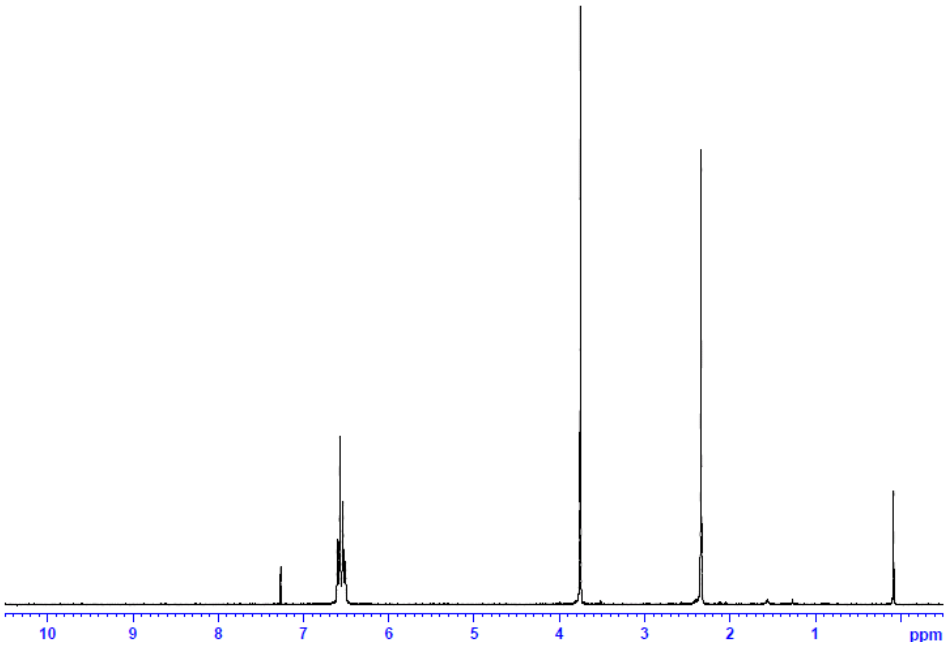

Figure 41. ^{1}H NMR spectrum of **5e**.

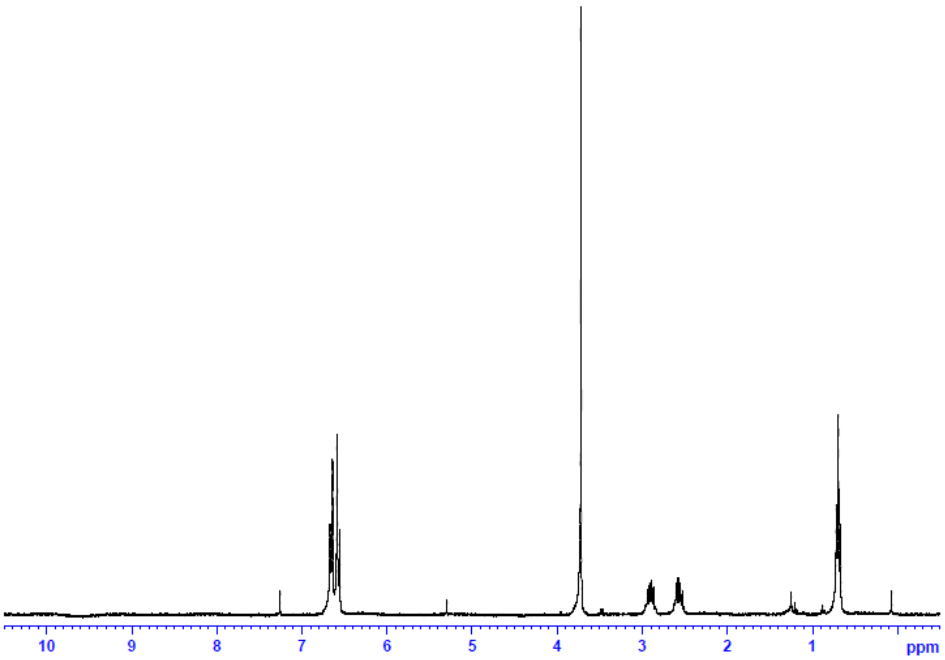

Figure 42. ^{1}H NMR spectrum of **5f**.

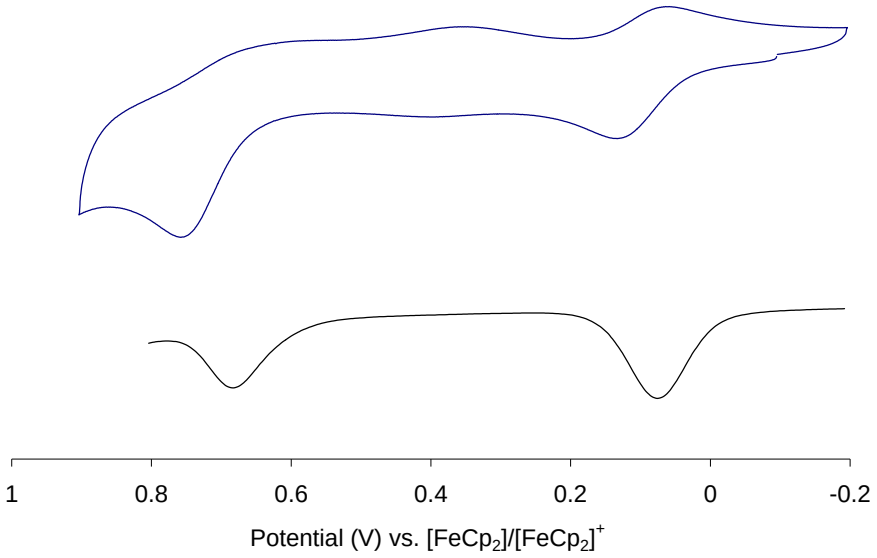

Figure 43. Cyclic and DPV voltammograms of 0.1 mM **5a** in CH_2Cl_2 (0.1 M NBu_4ClO_4) at scan rates of 0.1 $V \cdot s^{-1}$.

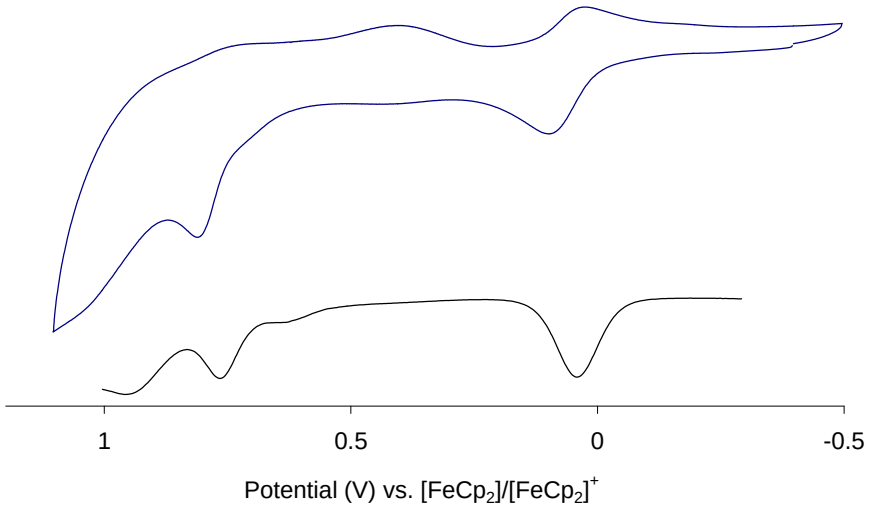

Figure 44. Cyclic and DPV voltammograms of 0.1 mM **5b** in CH_2Cl_2 (0.1 M NBu_4ClO_4) at scan rates of 0.1 $V \cdot s^{-1}$.

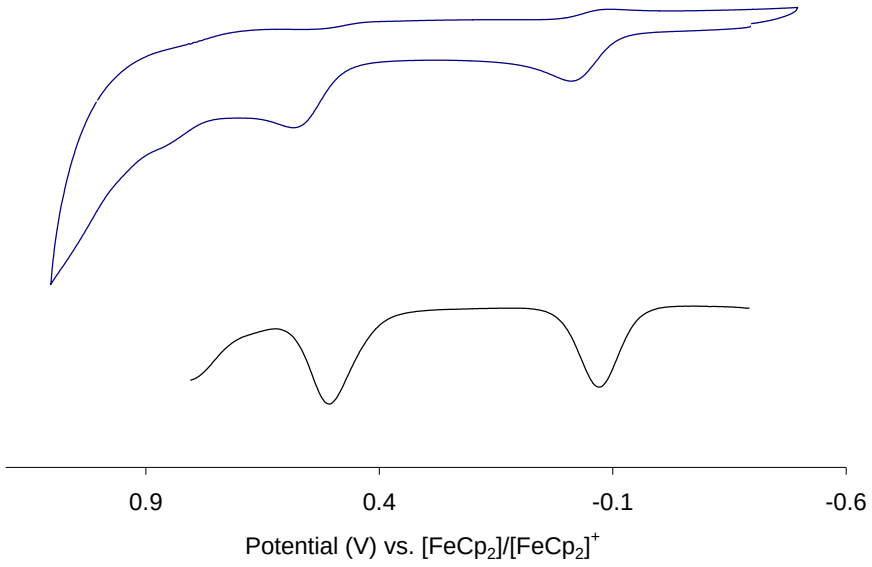

Figure 45. Cyclic and DPV voltammograms of 0.1 mM **5c** in CH_2Cl_2 (0.1 M NBu_4ClO_4) at scan rates of 0.1 $V \cdot s^{-1}$.

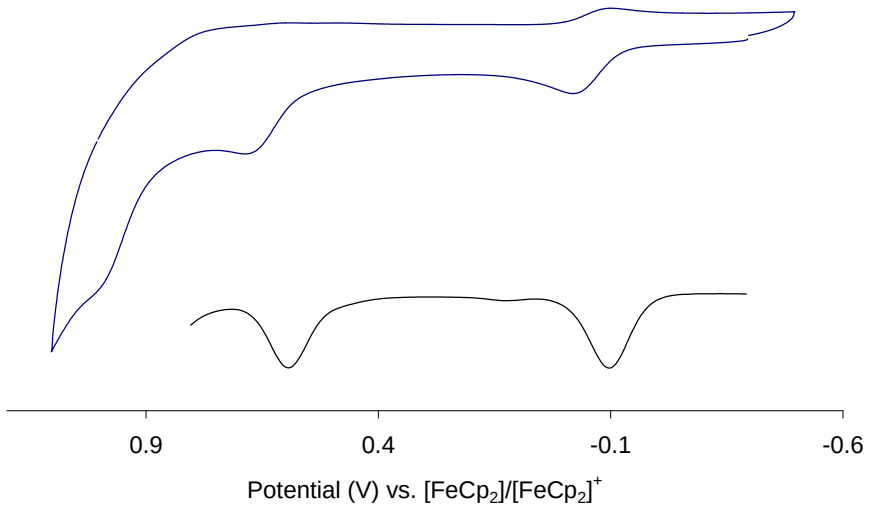

Figure 46. Cyclic and DPV voltammograms of 0.1 mM **5d** in CH_2Cl_2 (0.1 M NBu_4ClO_4) at scan rates of 0.1 $V \cdot s^{-1}$.

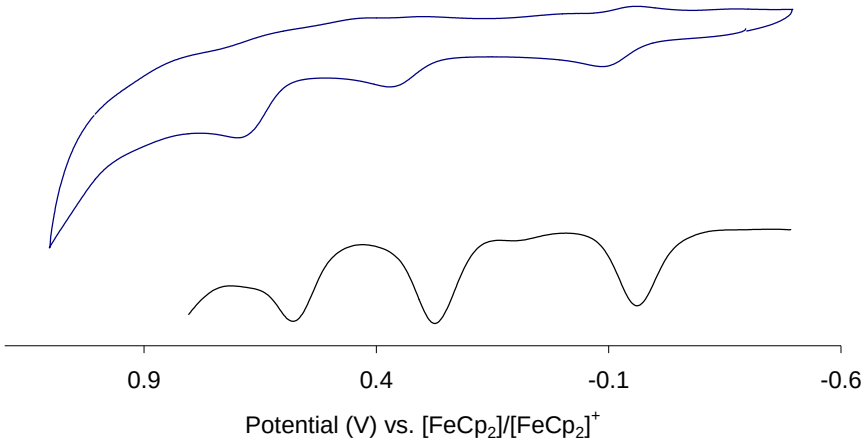

Figure 47. Cyclic and DPV voltammograms of 0.1 mM **5e** in CH_2Cl_2 (0.1 M NBu_4ClO_4) at scan rates of 0.1 $V \cdot s^{-1}$.

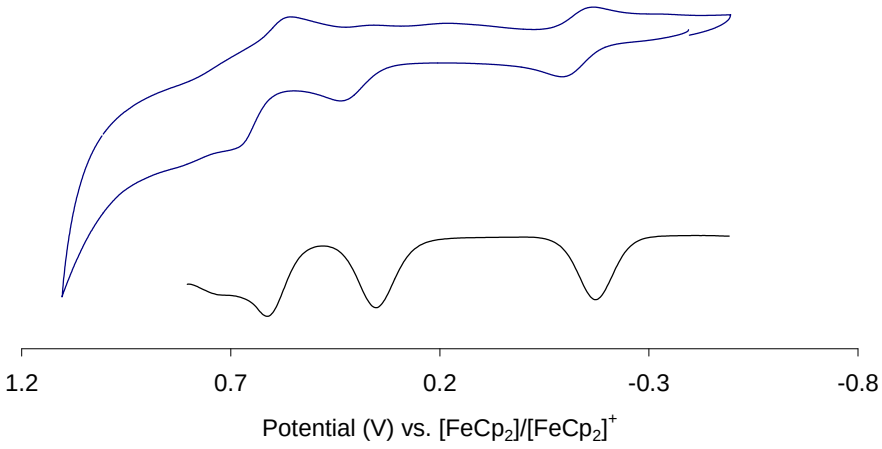

Figure 48. Cyclic and DPV voltammograms of 0.1 mM **5f** in CH_2Cl_2 (0.1 M NBu_4ClO_4) at scan rates of 0.1 $V \cdot s^{-1}$.

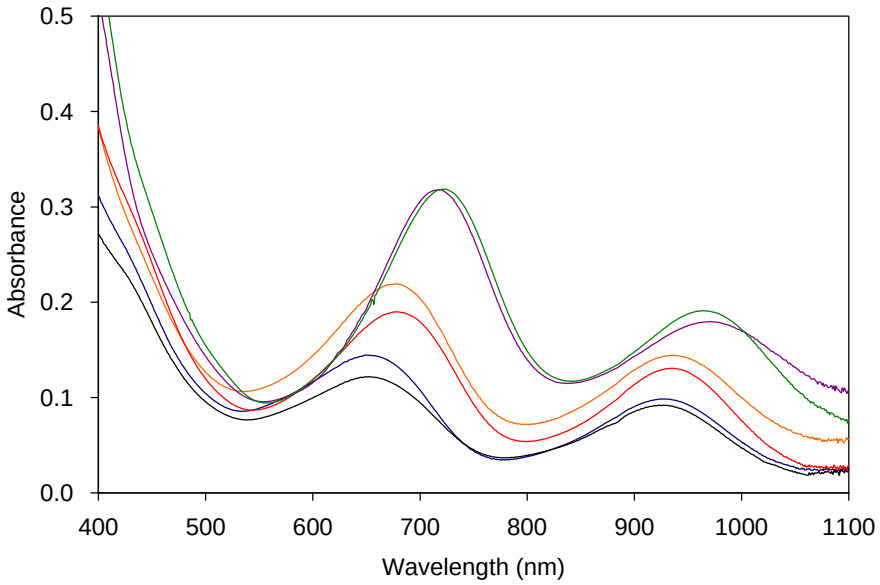

Figure 49. UV–Vis spectra of 0.1 mM of **6a** (—, blue), **6b** (—, black), **6c** (—, orange), **6d** (—, red), **6e** (—, purple), and **6f** (—, green) in CH_2Cl_2. Pathlength = 0.5 cm.

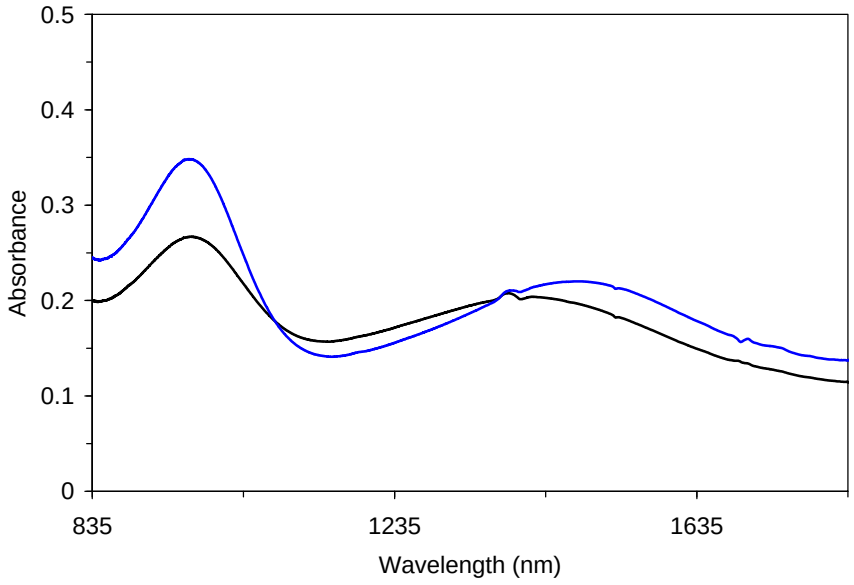

Figure 50. Near-IR spectra of 0.1 mM of **6e** (—, blue) and **6f** (—, black) in $CDCl_3$. Pathlength = 1.0 cm.

CHAPTER 6

REACTIVITY OF TRIS(GUANIDINATO) COMPLEXES OF IRIDIUM AND RHODIUM

6.1 Introduction

The reactivity of Ir and Rh complexes with guanidato ligands is described in this chapter. The chemical reversibility of the Ir^{III}/Ir^{IV} redox couple was demonstrated by adding reductants to **4a**. A series of acids was utilized for investigating the pK_a of **3a** and **4a**. As expected, compared to Ir^{IV} the more electron rich Ir^{III} complex, **3a**, can be protonated by relatively weaker acids. Substrate oxidation was examined by reacting **4a** with substrates having weak O–H or C–H bonds. The products in the oxidation of 2,4-di-*t*-butylphenol and hydroquinone were identified as 3,3',5,5'-tetra-*t*-butyl-(1,1'-biphenyl)-2,2'-diol and quinhydrone by GC-MS. A kinetic investigation was carried out for the reaction of **4a** with hydroquinone. Under pseudo-first-order conditions (10–100 equiv), the observed rate constant was independent of $[Ir]_0$ and increased linearly with $[\text{hydroquinone}]_0$; $k_2 = 5.2 \cdot 10^{-4}$ $M^{-1}\cdot s^{-1}$ (40 ºC). The kinetic isotopic effect (KIE = 0.9) revealed that the bond breaking is not the rate-determining step for this reaction. Values for $\Delta H^{\neq}$ (26.6 kcal·mol^{-1}) and $\Delta S^{\neq}$ (14.9 cal·mol^{-1}) were determined from reactions in the temperature range of 18–40 °C. On the other habd, no reaction was observed for substrates having weak C–H bonds (*e.g.*, xanthene, BDE = 75.5; 1,4-cyclohexadiene, BDE = 77.0 triphenylmethane, BDE = 81.0). Finally, substrate oxidation was also carried out by the rhodium complex, **6a**, and the reactivity is much greater compared to that of the Ir counterpart **4a**.

6.2 Experimental Section

Materials. All reagents and solvents were purchased from commercial sources and were used as received, unless noted otherwise. Acetonitrile and dichloromethane were deoxygenated by sparging with N_2 and purified by passage through two packed columns of molecular sieves under an N_2 pressure (MBraun solvent purification system). Preparation and handling of air- and moisture-sensitive materials were carried out under an inert gas atmosphere by using either standard Schlenk and vacuum line techniques or a glovebox. Hydroquinone was recrystallized from acetonitrile under N_2 atmosphere. 2,2,6,6-tetramethyl-piperidine-1-ol (TEMPOH) was synthesized according to a published procedure.[115] Hydroquinone-d_2 was prepared by treating hydroquinone with degassed D_2O.

Physical Methods. NMR spectra were recorded on a Bruker Avance 300 or Avance DRX 400 spectrometer at ambient temperature. ^{1}H chemical shifts are reported in parts per million (ppm) and were referenced to residual solvent peaks. Mass spectral data were acquired on a quadrupole ion trap ThermoFinnigan LCQ Deca mass spectrometer using an electrospray ionization source or on a double-focusing magnetic-sector Micromass, Inc., Autospec mass spectrometer using an electron impact ionization source (equipped with a solids probe). Analysis by GC–MS was performed on a TRACE GC 2000 gas chromatograph (column, DB-5 capillary) coupled with a single quadrupole ThermoFinnigan Voyager mass spectrometer with He carrier gas with a detector temperature of 250 °C and an injection temperature of 230 °C; initial temperature was maintained at 50 °C for 2 min and then raised to 250 °C at the rate of 10 °C·min^{-1}. UV–Visible spectra were recorded on an HP 8454A diode array spectrophotometer (Agilent Technologies).

Kinetic Measurements. The kinetic measurements were carried out using UV–Vis spectroscopy. A 0.1 mM solution of **4a** (1×10^{-4} mmol) in 1 mL of dichloromethane was placed in a 0.5-cm UV–Vis cuvette at 40 ºC. All kinetic runs were made under pseudo-first order conditions. The progress of the reactions was monitored by following the decrease in absorbance of **4a** at 696 nm. All measurements were done in triplicate, and the rate constants were obtained by linear least-squares fit to a first-order rate law.

The observed rate constants, k_{obs}, were determined from reactions with a concentration of **4a** of 0.1 mM and concentrations of hydroquinone in the range of 1–100 mM. k_{obs} values were also determined for reactions with a concentration of hydroquinone of 10 mM and concentrations of **4a** in the range of 0.05–0.2 mM. For the Eyring analysis, measurements were performed between 18 ºC and 40 ºC.

6.3 Electron transfer

The prior study in Chapter 4 showed that the chemical oxidation of **3a–d** in dichloromethane solution with $[FeCp_2]PF_6$ produced the Ir^{IV} complex, **4a–d**. On the other hand, the reduction of the iridium complexes from Ir^{IV} to Ir^{III} by mild reductants, $[CoCp_2]$ (E^o = –1.33 V) and $[Fe(C_5Me_5)_2]$ (E^o = –0.59 V),[11] was achievable. As shown in Figure 26, one equivalent of $[Fe(C_5Me_5)_2]$, is required for the maximal formation of **3a**. Moreover, the isosbestic point at 440 nm indicates that Ir^{IV} converts to Ir^{III} without any formation of intermediates.

Oxidation of **3a–d** was also investigated with the organic oxidants TCNE (tetracyanoethylene) (E^o = –0.27 V) and TCNQ (tetracyanoquinodimethane) (E^o = –0.30 V).[11] For example, **3a–d** were converted to **4a–d** by treatment with 1 equiv of TCNE. However, TCNQ can only oxidize **3c** and **3d**.

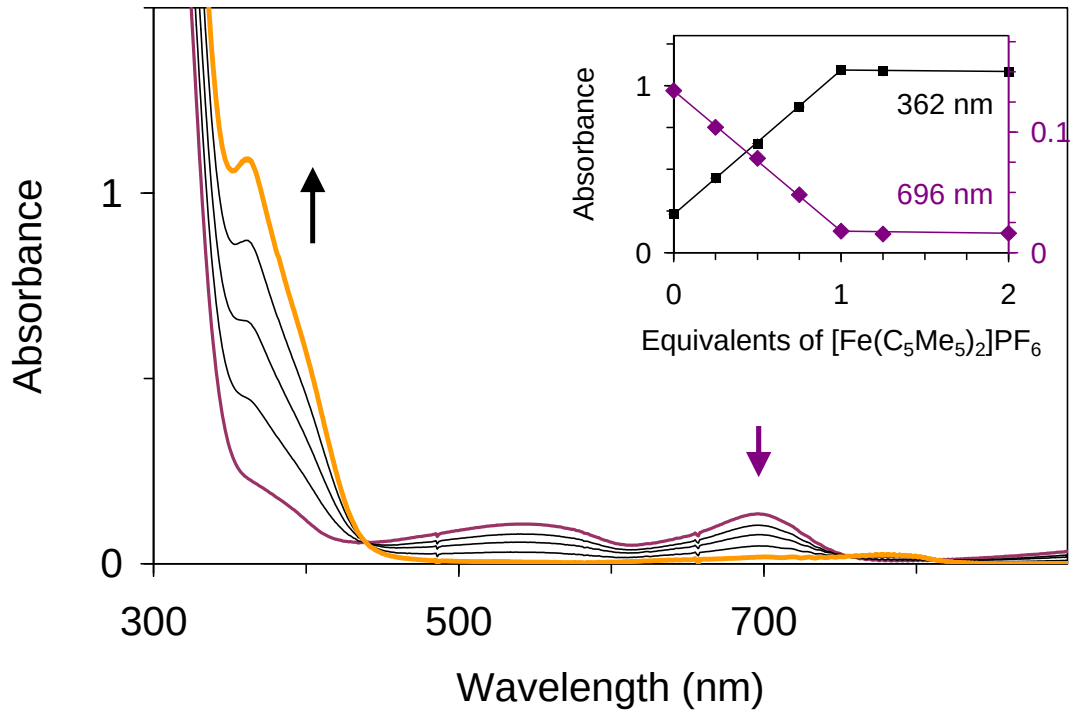

Figure 51. Reduction of 0.1 mM **4a** (—, yellow) to **3a** (—, violet) in CH_2Cl_2 by addition of [FeCp*$_2$] in increments of 0.25 equiv as monitored by electronic absorption spectroscopy (pathlength, 0.5 cm). Inset: Corresponding changes of the absorbance at 362 (■, black) and 696 nm (◆, violet).

6.4 Reactivity toward Acids

A series of acids including strong acids, hydrochloric acid and trifluoromethanesulfonic acid, and acetic acid derivatives were used to evaluate the tolerance of the iridium complexes toward acids. When acetic acid (pK_a = 4.8),[129] 3,5-dichlorobenzoic acid (pK_a = 3.5),[129] iodoacetic acid (pK_a = 3.1),[129] and chloroacetic acid (pK_a = 2.9)[129] were added to **3a**, no change was observed in the UV–Vis spectrum, indicating that protonation did not occur. However, when stronger acids such as dichloroacetic acid (pK_a = 1.4),[129] trichloroacetic acid (pK_a = 0.7),[129] hydrochloric acid,

or trifluoromethanesulfonic acid were added to **3a**, the feature in the UV–Vis spectum changed instantaneously (Figure 26). Interestingly, after addition of 1 equiv of TfOH to **3a**, the ions representing protonation products observed in the ESI(+)MS at *m/z* = 908.0, 949.3, and 1140.3 are consistent with $\{\mathbf{3a} + H\}^+$, $\{\mathbf{3a} + H + MeCN\}^+$, and $\{\mathbf{3a} + 2H + 2MeCN + {}^-OTf\}^+$ (Scheme 21). The latter two ions may indicate that the guanidinato ligand was protonated, followed by conversion of bidentate to monodentate coordination and coordination of MeCN molecules to the It center, *e.g.* $[Ir\{L\}_2\{LH\}(NCMe)]^+$ and $[Ir\{L\}\{LH\}_2(NCMe)_2]^+$. Treatment of a second equiv of TfOH produced a new species, $\{\mathbf{3a} - L + 2\ MeCN\}^+$, where L = guanidinato ligand, observed in ESI(+)MS. This ion simply reflects that the protonation occurs continuously upon addition of acids and causes removal of the guanidinato ligands.

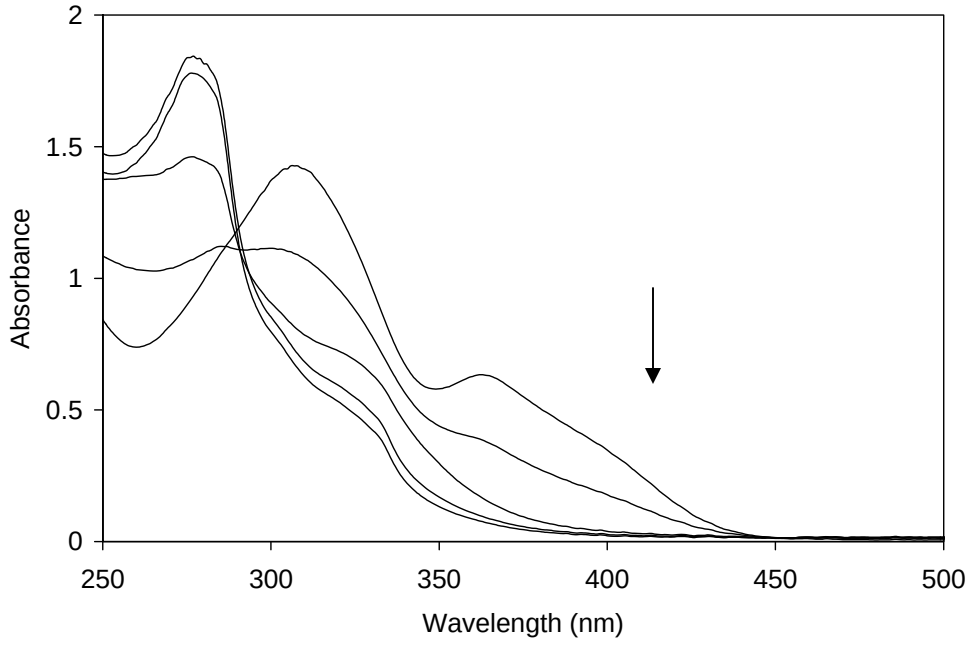

Figure 52. Reaciton of 0.1 mM **3a** with TfOH in CH_2Cl_2. Addition of [TfOH] in increments of 1 equiv as monitored by electronic absorption spectroscopy (pathlength, 0.5 cm).

On the other hand, **4a** was examined by the same series of acids. Compared to **3a**, **4a** shows higher tolerance toward strong acid TfOH (Figure 58). Likewise, no change of feature was observed when using 1–5 equiv of acetic acid, 3,5-dichlorobenzoic acid, iodoacetic acid, and chloroacetic acid. Unlike **3a**, **4a** does not react with dichloroacetic acid, and reacted slowly with 2 equiv of trichloroacetic acid, which indicates that **4a** has weaker affinity toward protons than **3a** because of its higher oxidation state of the metal center.

Scheme 21. Protonation of **3a** with Acid.

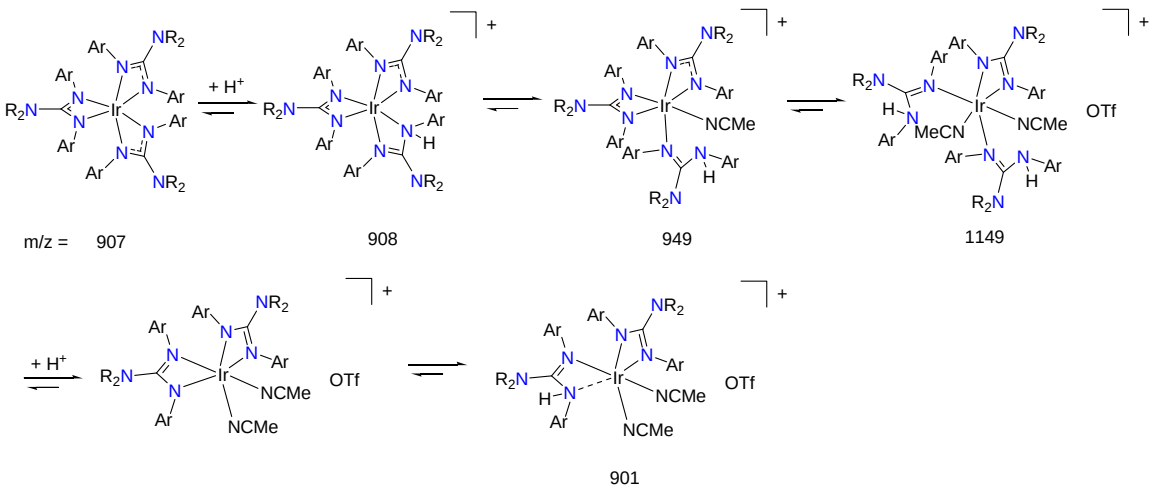

6.5 Reactivity toward Organic Substrates with O–H bonds

6.5.1 Reactivity of Iridium(IV) Complexes

In order to understand the reactivity of Ir^{IV} complexes, different types of substrates with C–H and O–H bond were investigated. First, the reaction with the O–H bond substrates was examined.

The reaction with 2,4-di-*tert*-butylphenol only occurred slowly at higher temperature (40 °C) and larger excess (>1000 equiv). Although TEMPOH would be a

good substrate (10 equiv, 20 °C: $t_{1/2}$ = 1700 s; 10 equiv, 40 °C: Ir^{IV} $t_{1/2}$ = 200 s) in terms of reaction time and amount of substrate used, the kinetic decay curve suggests that the reaction may not follow a simple first- or second-order rate law. Hydroquinone was a suitable candidate for the oxidative chemistry with Ir^{IV} complexes. Addition of 10 or more equiv of hydroquinone to 0.1 mM of **4a** in CH_2Cl_2 at 40 °C resulted in formation of the charge transfer complex, quinhydrone, which was observed in the GC–MS. Although the inorganic products were not observed by mass spectrospcopy, the final UV–Vis spectrum of the reaction was similar to the spectrum obtained from protonation of **3a**, which indicates that after oxidation of hydroquinone, a free proton was released causing the protonation of the Ir complex.

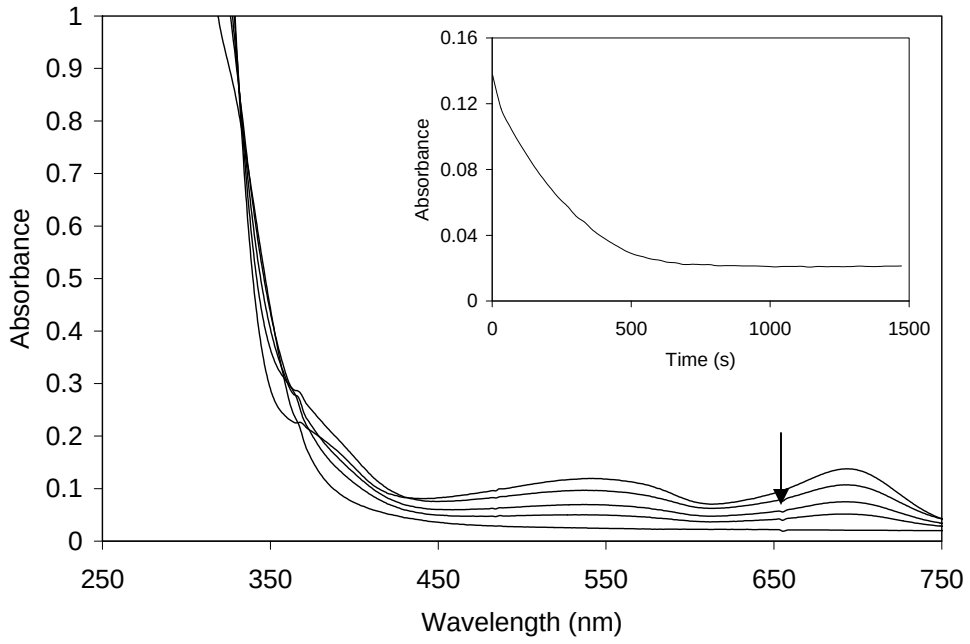

Figure 53. Reaction of 0.1 mM **4a** with 100 equiv of hydroquinone in CH_2Cl_2 at 40 °C as monitored by electronic absorption spectroscopy. Inset: Time course of the reactions of **4a** (λ = 696 nm). Pathlength = 0.5 cm.

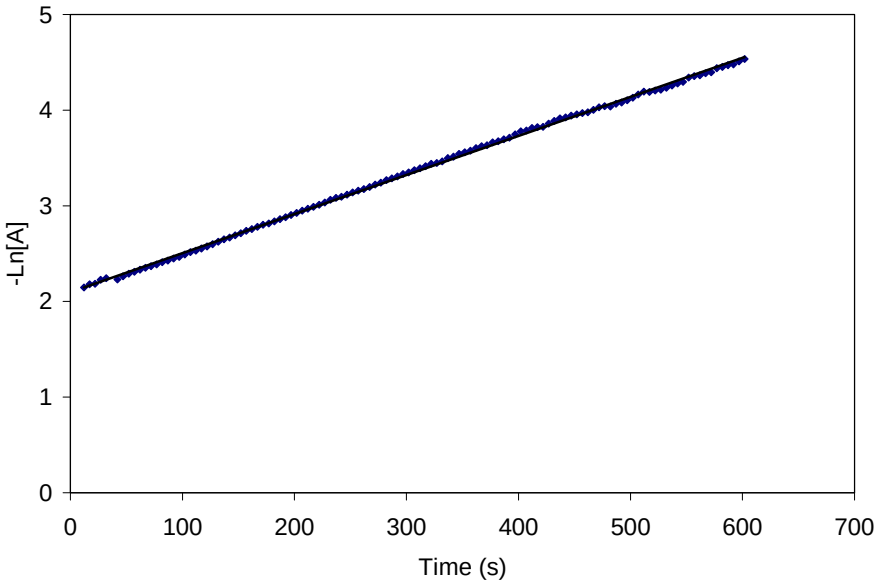

Figure 54. First-order rate law fit (solid line) for the reaction (♦) of 0.1 mM **4a** with 100 equiv of hydroquinone in CH_2Cl_2 at 40 °C as monitored by electronic absorption spectroscopy. Pathlength = 0.5 cm.

Time courses for six different concentrations (1, 4, 10, 20, 40, and 60 mM) of hydroquinone (under pseudo-first-order conditions) at 40 °C were investigated to determine the reaction order in hydroquinone (Figure 27). The half-lives decrease with increasing [HQ], and the time courses fit to a first-order rate law (Figure 28). It was found that experimental plots of ln[A] *vs*. *t* appeared to be approximately linear over three half-lives, and the k_{obs} values were in the range of $2.4 \cdot 10^{-4}$ to $2.0 \cdot 10^{-2}$ s^{-1} and increase linearly with [HQ] (Figure 29). In a similar manner, the time courses for five different concentrations (0.05, 0.07, 0.1, 0.14, and 0.2 mM) of **4a** under pseudo-first-order conditions at 40 °C were observed (Figure 59). The half-lives are constant with varying [**4a**], and the time courses fit to a first-order rate law. The plots of ln[A] *vs*. *t* appear to be approximately linear over three half-lives and the k_{obs} values were found to be independent of [**4a**]. As a result, the second-order rate constant, $k_2 = 3.2 \cdot 10^{-4}$ $M^{-1}s^{-1}$, was determined from the slope of a plot of k_{obs} *vs.* [HQ]. An inverse kinetic isotopic

effect (KIE = 0.9) suggests that the O–H(D) bond breaking is not the rate-determining step in the reaction (Figure 60). It is worth noting that the reaction was accelerated in the presence of trifluoromethanesulfonic acid, and the half-lives (145 to 15 s) decrease with increasing [TfOH] (1 to 4 equiv, Figure 61). Additionally, the reaction could also be sped up ($t_{1/2}$ = 160 s) in the presence of 1 equiv of pyridine under the same reaction conditions (100 equiv of hydroquinone at 40 °C, Figure 62).

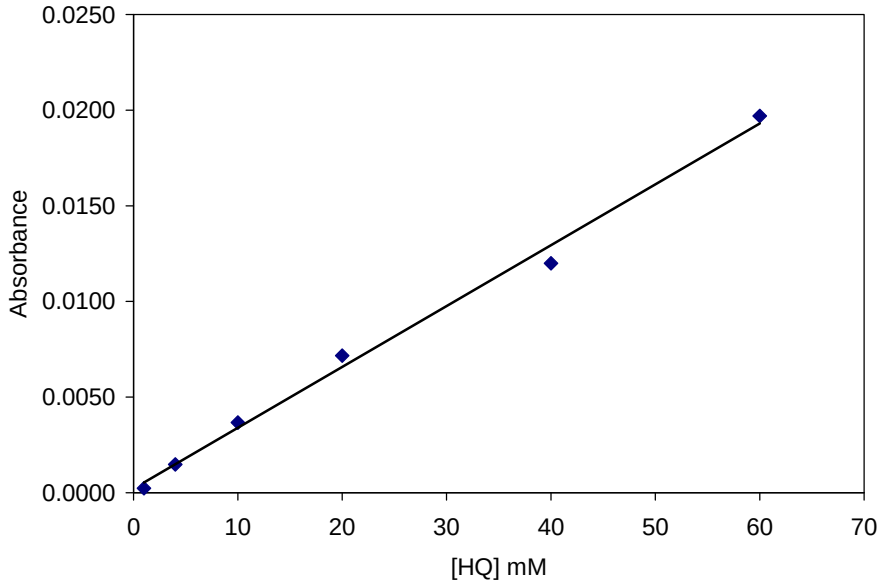

Figure 55. The plot of k_{obs} *vs.* [HQ] for the reaction of 0.1 mM **4a** with variable concentration of hydroquinone.

The Eyring plot for the reduction of **4a** by hydroquinone in dichloromethane over the temperature range of 18 to 40 °C is shown in Figure 30. A linear fit of $\ln(k_{obs}/T)$ vs. $1/T$ was used to determine the enthalpy ($\Delta H^{\neq}$) and entropy ($\Delta S^{\neq}$) of activation. The $\Delta H^{\neq}$ and $\Delta S^{\neq}$ were determined to be 26.6 kcal·mol^{-1} and 14.9 cal·mol^{-1}, respectively.

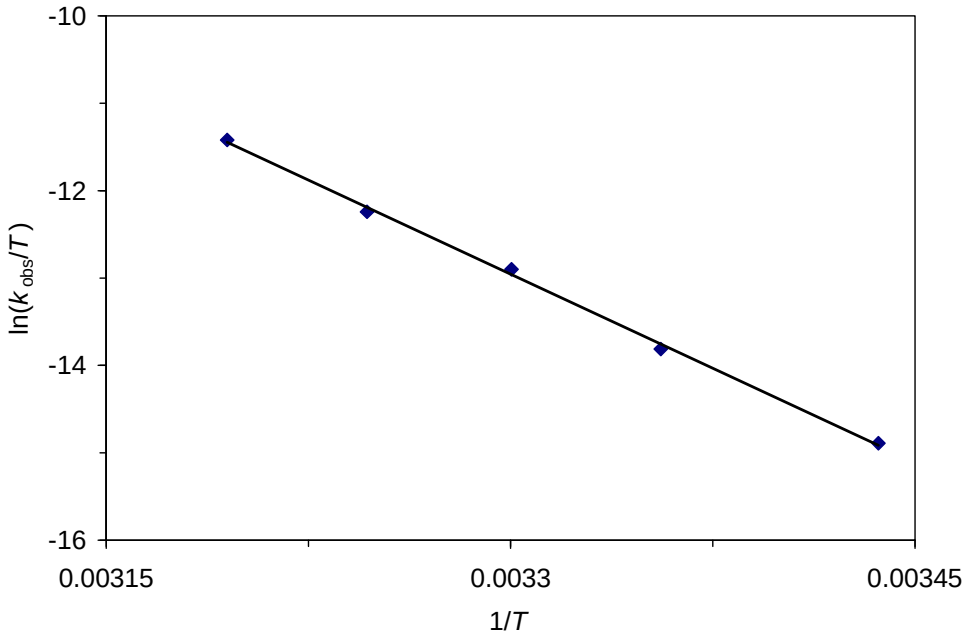

Figure 56. Eyring plot for the reduction of **4a** by hydroquinone. Temperatures range from 18 to 40 °C.

As anticipated, because the metal center is well protected by the bulky tris-ligand environment, the oxidation of hydroquinone is impossible through an inner-sphere mechanism, since no coordination site is available. In addition, the outer-sphere electron transfer was ruled out as well, considering the oxidation potential of **4a** is not strong enough to oxidize the organic substrates mentioned above. Therefore, the possible reaction mechanisms for the O–H bond substrate oxidation with Ir^{IV} complex were shown in Figure 31: a) the interaction of Ir^{IV} complex with organic substrate through hydrogen bonding followed by electron transfer; b) the protonation of Ir^{IV} complex occurred with the O–H organic substrate followed by opening a coordination site, binding with organic substrate, and transferring electron from substrates to metal center. Given the pK_a values of Ir^{IV} complex and organic substrates, the pathway (b) must be eliminated because the protonation evaluation (Section 6.4) shows that strong acids are

required to protonate Ir^{IV} complex. The interaction of Ir^{IV} complex with the O–H organic substrate through hydrogen bonding described in pathway (a) may be a key step for proceeding the reaction. This may be explained that no reaction occurred when using substrates with C–H bonds. In addition, the fact that the reaction can be accelerated by addition of acids can also elucidate that the open coordination site is crucial for the reaction.

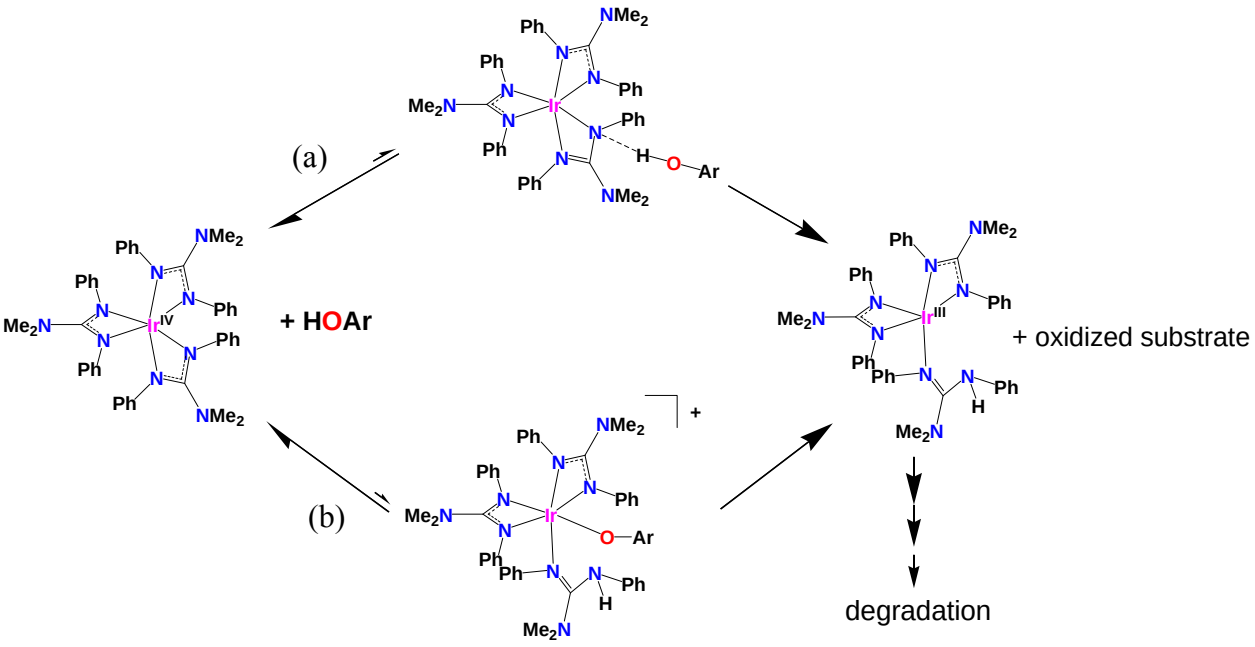

Figure 57. The proposed mechanism for the substrate oxidation of Ir^{IV} complexes

Likewise, while complexes **4b–d** also reacted with hydroquinone, the rates of the reactions varied with the substituents on the guanidinato ligand. Rate constants (k_2) for four different concentrations (4, 10, 40, and 60 mM) of hydroquinone (under pseudo-first-order conditions) at 40 °C were investigated to determine the reaction order in hydroquinone (Figures 63–65). Under the same conditions, the k_2 of the Ir^{IV} complexes decrease in the expected order **4a** < **4b** < **4c** < **4d** ($k_2 = 3.2 \cdot 10^{-4}$, $8.2 \cdot 10^{-5}$, $6.8 \cdot 10^{-5}$,

and 7.0 x 10^{-6} s respectively). The linear correlation between $Ir^{III/IV}$ redox potentials and the half-lives of the corresponding Ir^{IV} complexes may indicate that the rate determining step of the hydroquinone oxidation is the electron-transfer process.

Although the reaction with substrates possessing weaker C–H bonds (*e.g.* 1,4-cyclohexadiene, triphenylmethine, dihydroanthracene, and xanthene) did not occur, the transformation could be observed with the O–H bond substrate such as TEMPOH, 2,4-di-*tert*-butylphenol, and hydroquinone. Therefore, bond dissociation energy of the C–H/O–H is not the only factor that affects the reaction; another factor, pK_a value of C–H/O–H, also plays a major role in the substrate oxidation.

6.5.2 Reactivity of Rhodium(IV) Complexes

The reactivity of Rh^{IV} complexes is expected to be higher than their Ir^{IV} counterparts, because they have higher redox potentials (as described in Chapter 5). Due to thermal instability, all the reactions for **6a** must be carried out at –60 °C. However, even at low temperature **6a** is still highly reactive toward substrates with O–H bonds. For example, the $t_{1/2}$ for the reaction of **6a** with 100 equiv of 2,4-di-tert-butylphenol at –60 °C is *ca.* 1 hour, and the $t_{1/2}$ for reaction of **4a** with 1000 equiv of 2,4-di-tert-butylphenol at room temperature is *ca.* 3.3 hours. Therefore, the Rh^{IV} complexes should be good oxidants for the oxidation of substrates with O–H bond.

6.6 Conclusion

The reactivity studies suggest that the tris(guanidinato)iridium(III) and tris(guanidinato)iridium(IV) complexes can undergo a variety of reactions. First, the reversibility of $Ir^{III/IV}$ observed in electrochemical studies can be carried out through chemical oxidation and reduction. The protonation of Ir^{III} and Ir^{IV} complexes not only evaluates the approximate pK_a values for both complexes but also demonstrates that the

electron deficient Ir^{IV} complexes have less affinity toward acids than that of Ir^{III}. Kinetic measurements show that the overall reaction is second order, and the kinetic isotope effect study suggests that the O–H bond breaking is not the rate determining step. The outer-sphere and inner-sphere electron transfer mechanism would be ruled out considering the large gap of redox potential between Ir^{IV} complexes and substrates, and the coordinatively saturated nature of the Ir^{IV} complexes. The addition of acid, which will open a coordination site, causes acceleration of the reaction.

Therefore, all the evidence from the experiments suggests that opening a coordination site on coordinatively saturated Ir^{IV} complexes is a key step for the substrate oxidation reaction. Finally, the reactivity of substrate oxidation for Rh^{IV} complexes is found to be higher than that of the Ir^{IV} counterpart.

6.7 Supplemental Materials

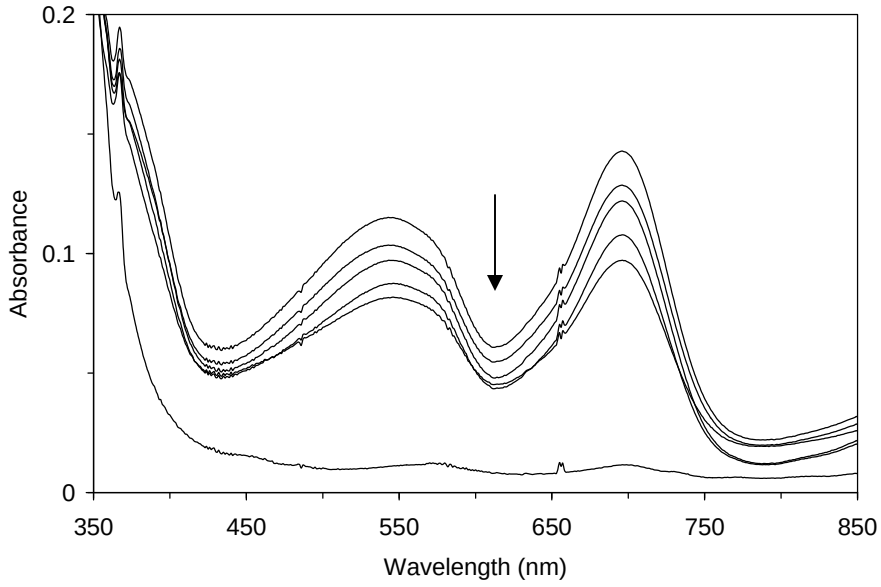

Figure 58. Reaciton of 0.1 mM **4a** with TfOH in CH_2Cl_2. Addition of [TfOH] in increments of 1 equiv as monitored by electronic absorption spectroscopy (pathlength, 0.5 cm).

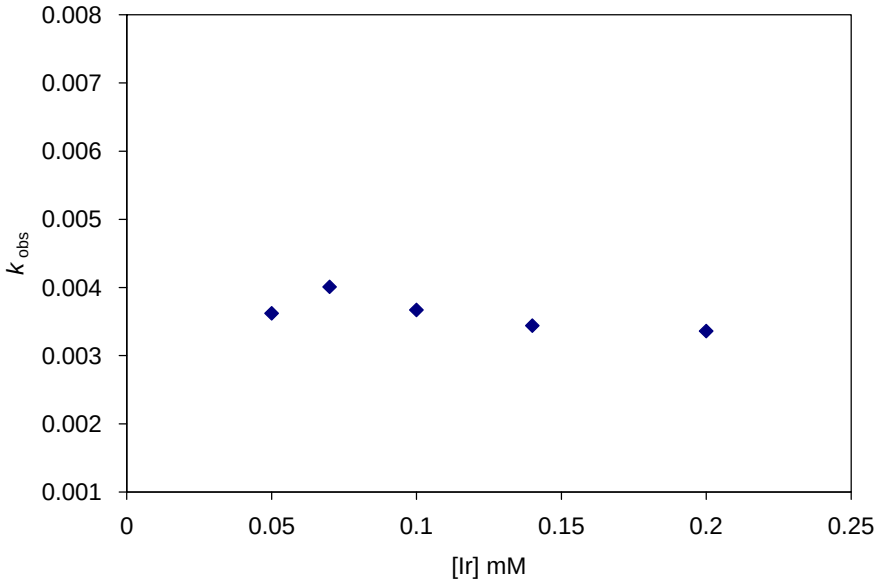

Figure 59. The plot of k_{obs} vs. [Ir] for the reaction of 10 mM hydroquinone with variable concentration of **4a**.

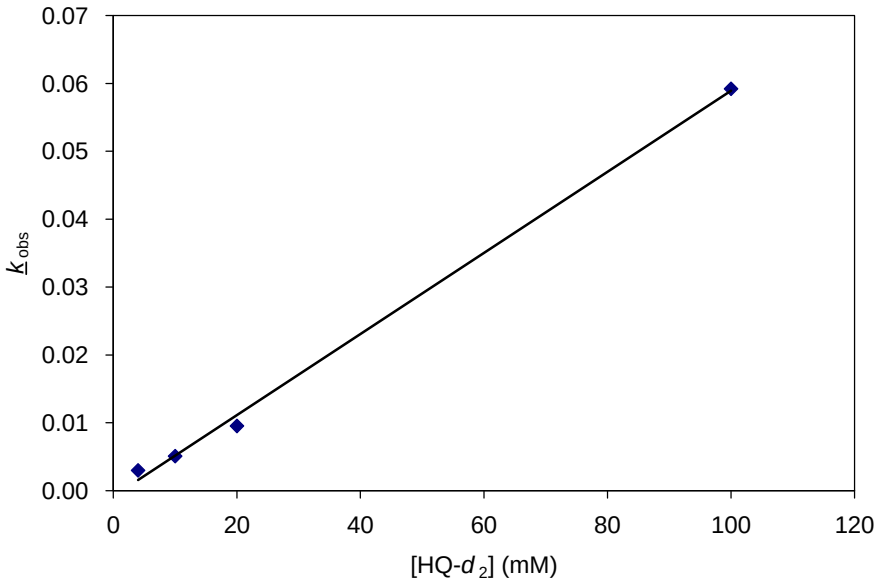

Figure 60. The plot of k_{obs} *vs.* [HQ-d_2] for the reaction of 0.1 mM **4a** with variable concentration of hydroquinone-d_2.

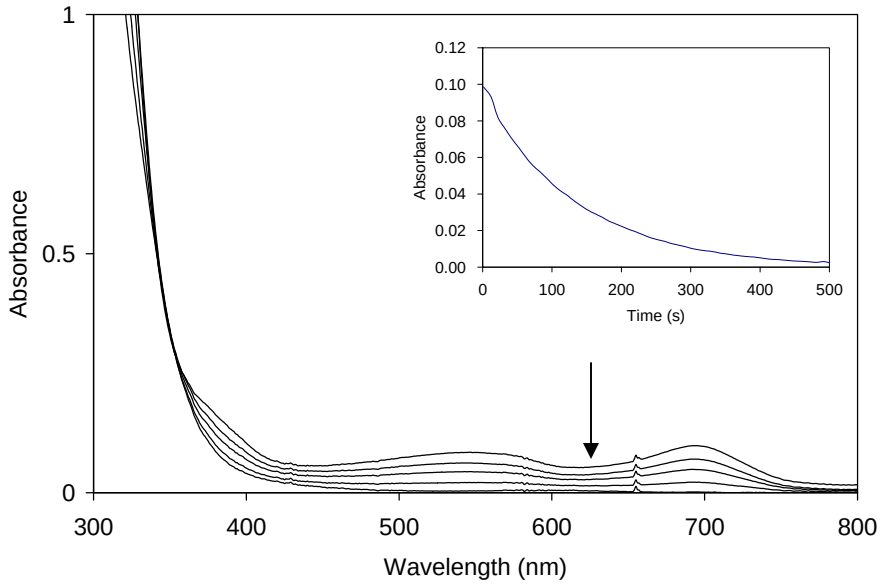

Figure 61. Reaction of 0.1 mM **4a** with 100 equiv of hydroquinone in the pres ence of 3 equiv of HOTf in CH_2Cl_2 at 40 °C as monitored by electronic absorption spectroscopy. Inset: Time course of the reactions of **4a** (λ = 696 nm). Pathlength = 0.5 cm.

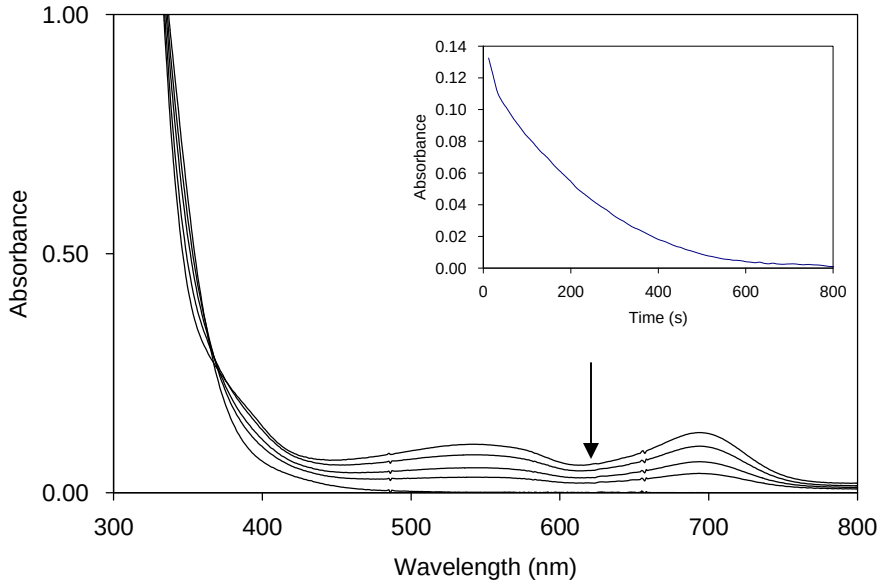

Figure 62. Reaction of 0.1 mM **4a** with 100 equiv of hydroquinone in the presence of 1 equiv of pyridine in CH_2Cl_2 at 40 °C as monitored by electronic absorption spectroscopy. Inset: Time course of the reactions of **4a** (λ = 696 nm). Pathlength = 0.5 cm.

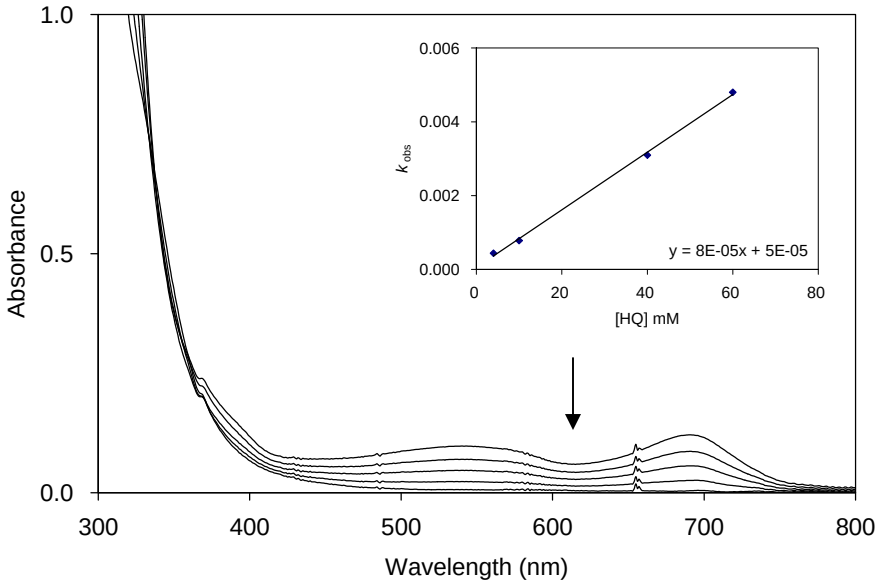

Figure 63. Reaction of 0.1 mM **4b** with 100 equiv of hydroquinone in CH_2Cl_2 at 40 °C as monitored by electronic absorption spectroscopy. Inset: The plot of k_{obs} *vs.* [HQ] for the reaction of 0.1 mM **4b** with variable concentration of hydroquinone. Pathlength = 0.5 cm.

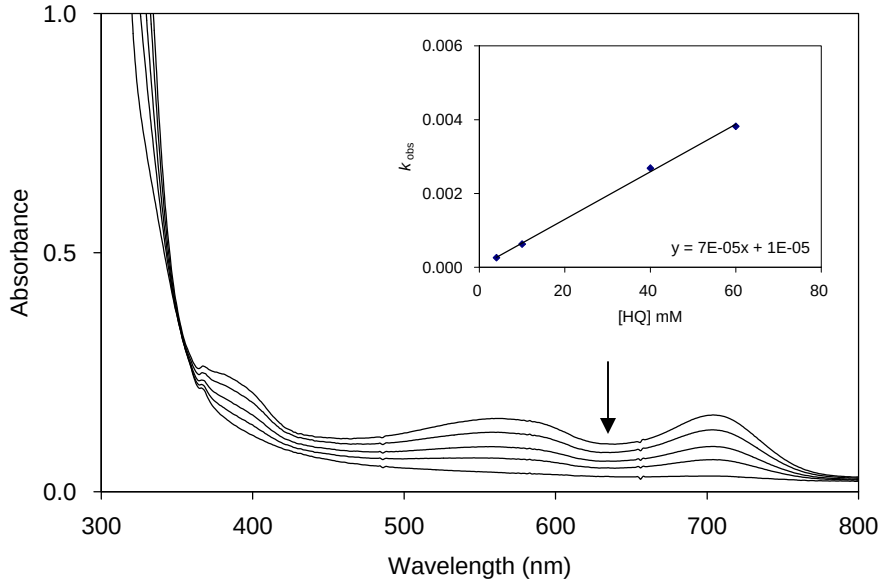

Figure 64. Reaction of 0.1 mM **4c** with 100 equiv of hydroquinone in CH_2Cl_2 at 40 °C as monitored by electronic absorption spectroscopy. Inset: The plot of k_{obs} *vs.* [HQ] for the reaction of 0.1 mM **4c** with variable concentration of hydroquinone. Pathlength = 0.5 cm.

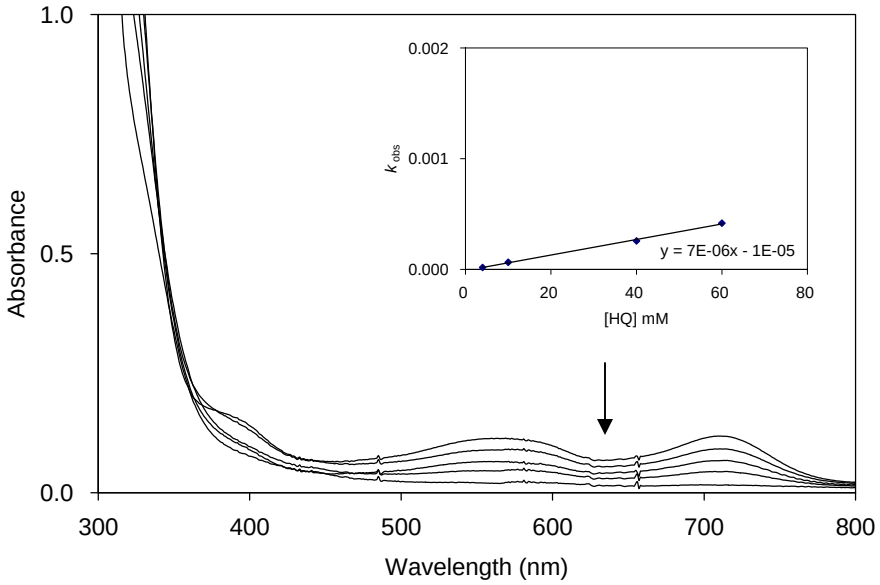

Figure 65. Reaction of 0.1 mM **4d** with 100 equiv of hydroquinone in CH_2Cl_2 at 40 °C as monitored by electronic absorption spectroscopy. Inset: The plot of k_{obs} *vs.* [HQ] for the reaction of 0.1 mM **4d** with variable concentration of hydroquinone. Pathlength = 0.5 cm.

CHAPTER 7

SUMMARY AND CONCLUSION

Mononuclear complexes of a low-valent *d*-block metal center coordinated by bidentate guanidinato(1–) ligands were prepared and characterized, thereby expanding the scope of this ligand platform in transition-metal chemistry. Spectroscopic evidence suggests that the *N*,*N*-dialkyl-*N*′,*N*″-diarylguanidinates employed here function as stronger donors than other monoanionic, nitrogen-based scaffolds, such as tris(pyrazolyl)borates-κ^2 and β-diketiminates, when bound to the $Ir^{I}(coe)_2$ unit. The reaction of complexes **2a–c** with O_2 led to product mixtures in which tris(chelate)iridium(III) complexes could be identified. This observation suggested a method for the rational synthesis of suxh complexes.

Rare examples of air-sensitive coordinatively saturated Ir^{III} and Rh^{III} complexes were prepared and characterized. Oxidation of the Ir compounds produced isolable, stable tris(guanidinato)iridium(IV) complexes, in which the Ir center is exclusively coordinated by nitrogen-donor ligands. For the Rh counterparts, oxidation generated thermally unstable tris(guanidinato)rhodium(IV) complexes. These results underscore the exceptional ability of the *N*,*N*-dialkyl-*N*′,*N*″-diarylguanidinate anions to stabilize transition metals in high oxidation states and suggest them as excellent ancillary ligands for new high-valent Ir and Rh complexes that may be tailored to effect useful transformations. Finally, the reactivity studies show that the high-valent complexes can oxidize substrates with O–H bonds.

Several directions related to this work can approach in the future. First, as observed in the cyclic voltammograms of **3a–d** in Figure 12 and Figures 26–28, the second redox process points at the existence of a doubly oxidized. Such compounds would be of interest because of their highly oxidizing power. However, they may be

expected to be fairly unstable so that the attempt synthesis and characterization may be carried out *in situ* at low temperature. Spectroscopic characterization could provide insights into their electronic structure and help answer the question whether those species are Ir^{V} or Ir^{IV}–ligand-radical complexes.

Secondly, the ability of the tris(guanidinato) platform to stabilize often transition metal centers in high oxidation states could be tested. For example, to complete the systematic investigation for the Group 9 of the periodic table, the cobalt tris(guanidinato) analogues can be prepared and characterized. Once the tris(guanidinato)cobalt(III) were prepared, the exploration of even rare Co^{IV} will be intriguing.

APPENDIX

TETRADENTATE PYRIDYL/BENZIMIDAZOLYL LIGANDS AND IRON(II) AND OXOIRON(IV) COMPLEXES

A.1 Introduction

Two tetradentate ligands **L1** and **L2**, and their Fe^{II} complexes, [Fe(**L1**)$(OTf)_2$] and [Fe(**L2**)$(OTf)_2$]; where **L1** = *N,N*-bis(2-benzimidazolylmethyl)-*N*-(2-pyridylmethyl)amine and **L2** = *N,N*-bis[(1-methylbenzimidazol-2-yl)methyl]-*N*-[(pyridin-2-yl)methyl]amine; were synthesized and characterized. The Fe–N bond lengths in the complexes obtained from solid state structures suggest that the Fe center in [Fe(**L1**)$(NCMe)_2$]$(OTf)_2$ is low-spin (S = 0) and that in [Fe(**L2**)$(NCMe)_2$]$(OTf)_2$ is high-spin (S = 2). However, the ^{1}H NMR spectra of these compounds in CD_3CN solution both exhibit paramagnetically shifted peaks between 120 and −15 ppm, which are typical for high-spin Fe^{II} complexes. The spin states of [Fe(**L1**)$(NCMe)_2]^{2+}$ in solution was further investigated by variable-temperature (VT) NMR spectroscopy. VT ^{1}H NMR spectroscopy (–40 to +80 °C) for [Fe(**L1**)$(NCMe)_2]^{2+}$ shows the spin equilibrium between high-spin and low-spin states over the temperature range of –40 to +50 °C. In addition, oxoiron(IV) complexes can be generated by reacting Fe^{II} complexes with excess of *m*CPBA at –40 °C. It is found that [Fe^{IV}(O)(**L1**)$(NCMe)_2$]$(OTf)_2$ and [Fe^{IV}(O)(**L2**)$(NCMe)_2$]$(OTf)_2$ are highly unstable in solution at –40 °C, where the former displays greater stability. The series studies of stability of [Fe^{IV}(O)(L)$(NCMe)_2$]$(OTf)_2$, where L = tris (pyridylmethyl)amine, **L1**, **L2**, and tris(2-benzimida`zolylmethyl)amine; suggest that the stability of these Fe^{IV}=O complexes varies with the pendant arm of the tetradentate ligands.

A.2 Experimental Section

Materials and Physical Methods. All reagents and solvents were purchased from commercial sources and were used as received, unless noted otherwise. Acetonitrile, dichloromethane, diethyl ether, and tetrahydrofuran were deoxygenated by sparging with N_2 and purified by passage through two packed columns of molecular sieves under an N_2 pressure (MBraun solvent purification system). Nitromethane was refluxed over CaH_2 under an Ar atmosphere, distilled, and passed through a column of basic Al_2O_3.[65] *m*-Chloroperbenzoic acid was purified by dissolving in benzene and washing with a pH 7.4 phosphate solution. The organic phase was dried over $MgSO_4$, evaporated under reduced pressure, and the residue was recrystallized from dichloromethane. Preparation and handling of air- and moisture-sensitive materials were carried out under an inert gas atmosphere by using either standard Schlenk and vacuum line techniques or a glovebox. $Fe(OTf)_2{\cdot}2MeCN$[116] was synthesized by a modified literature method[117] from anhydrous $FeCl_2$ and trimethylsilyl trifluoromethanesulfonate in acetonitrile and recrystallized from acetonitrile–diethyl ether.[118] [$Fe(Me_3ntb)(OTf)_2$] was received from professor Wonwoo Nam's research group in the Ewha Womans University, Korea. Elemental analyses were performed by Atlantic Microlab, Inc., Norcross, GA, USA.

NMR spectra were recorded on a Bruker Avance MicroBay 300, Avance DPX 300, and Avance DRX 400. VT-NMR spectra were recorded on Bruker Avance DRX 400 in the temperature range of –40 to +80 °C. ^1H chemical shifts are reported in parts per million (ppm) and were referenced to residual solvent peaks. Mass spectral data were acquired on a quadrupole ion trap ThermoFinnigan LCQ Deca mass spectrometer using an electrospray ionization source. UV–Visible spectra were recorded on an HP 8453A diode array spectrophotometer (Agilent Technologies) with samples maintained at low temperature using a cryostat from Unisoku Scientific Instruments, Japan.

2-Benzimidazolylmethylamine.[119] A solution of 3.30 g (44.0 mmol) of glycine and 4.75 g (43.9 mmol) of 1,2-diaminobenzene in 20 mL of 7 M HCl was heated under reflux for three days. When the solution was cooled to room temperature, the product precipitated in form of its hydrochloride salt. The precipitate was separated by filtration and dissolved in 20 mL of water, followed by addition of an NH_4OH solution to adjust the pH to 9. The solution was washed with dichloromethane (2 x 10 mL). The product, which is more soluble in water than in dichloromethane, was obtained in crystalline form by storing the aqueous solution at ca. 4 °C. Yield: 4.61 g (71%). ^{1}H NMR (300 MHz, D_2O, δ): 7.59-7.56 (m, 2H, Ar H), 7.30-7.27 (m, 2H, Ar H) 4.35 (s, 2H, CH_2NH$_2$).

***N*-(2-Benzimidazolylmethyl)-*N*,*N*-bis(2-pyridylmethyl)amine.** This compound was synthesized by a modified literature method.[117] A suspension of 3.90 g (23.8 mmol) of 2-(chloromethyl)pyridine hydrochloride and 1.04 g (7.07 mmol) of 2-benzimidazolylmethylamine in 50 mL of dichloromethane was prepared at 0 °C. A solution of 7.7 mL (5.6 g, 55 mmol) of triethylamine in 20 mL of dichloromethane was added dropwise to this suspension under stirring, after which the resulting mixture was allowed to warm to room temperature and stirred for three days. The reaction mixture was washed with 50 mL of water and dried over $MgSO_4$. The solvent was removed under reduced pressure to afford a red oil, which was washed with 50 mL of diethyl ether to remove excess 2-(chloromethyl)pyridine and dissolved in 50 mL of dichloromethane. The solution was washed with water (3 x 30 mL) and dried over $MgSO_4$. The solvent was removed under reduced pressure to give a brown solid. This product was used without further purification in the next step. Yield: 0.71 g (31%). ^{1}H NMR (300 MHz, $CDCl_3$, δ): 8.63 (m, 2H, Ar H), 7.64-7.59 (m, 4H, Ar H), 7.32 (d, 2H, Ar H), 7.24-7.17 (m, 4H, Ar H), 4.09 (s, 2H, benzimidazolyl CH_2N), 3.91 (s, 4H, pyridyl CH_2N).

***N*-[(1-Methylbenzimidazol-2-yl)methyl]-*N*,*N*-bis[(pyridin-2-yl)methyl]amine (L1).** To 88 mg (1.57 mmol) of powdered KOH (prepared under exclusion of moisture)

were added a solution of 170 mg (0.52 mmol) of *N*-(2-benzimidazolylmethyl)-*N,N*-bis(2-pyridylmethyl)amine in 10 mL of dimethyl sulfoxide and 0.049 mL (0.11 g, 0.79 mmol) of iodomethane. The reaction mixture was stirred for 1 h, after which it was poured into 50 mL of water. The product was extracted with chloroform (3 x 30 mL), and the combined organic phases were washed with water (5 x 30 mL) and dried over $MgSO_4$. The volatiles were removed under reduced pressure to afford an orange solid. The product was extracted from the residue with 100 mL of diethyl ether and, after evaporation of the solvent, isolated as a yellow solid. The product was recrystallized from acetone and dried *in vacuo*. Yield: 103 mg (58%). Anal. Calcd for $C_{21}H_{21}N_5$: C, 73.44; H, 6.16; N, 20.39. Found: C, 72.98; H, 6.11; N, 20.46. ^{1}H NMR (300 MHz, $CDCl_3$, δ): 8.54 (m, 2H, Ar H), 7.70 (m, 1H, Ar H), 7.60 (m, 2H, Ar H), 7.39 (d, J = 7.8 Hz, 2H, Ar H), 7.26-7.10 (m, 5H, Ar H), 4.02 (s, 2H, benzimidazolyl CH_2N), 3.88 (s, 4H, pyridyl CH_2N), 3.69 (s, 3H, NCH_3). ^{13}C NMR (75.5 MHz, $CDCl_3$, δ): 158.5, 151.6, 149.1, 143.1, 136.2, 123.6, 122.4, 122.1, 121.7, 119.6, 109.0, 60.3 (pyridyl CH_2N), 51.3 (benzimidazolyl CH_2N), 30.0 (NCH_3). EIMS (70 eV) *m/z*: $M^{+\bullet}$ calcd for $C_{21}H_{21}N_5$, 343.18; found, 343.0.

Dipotassium *N*-(2-pyridylmethyl)iminodiacetate.[120] To a stirred solution of 1.33 g (10.0 mmol) of iminodiacetic acid and 1.12 g (20.0 mmol) of KOH in 10 mL of water, which was kept in an ice bath, was added dropwise a solution of 1.64 g (10.0 mmol) of 2-(chloromethyl)pyridine hydrochloride and 0.56 g (10.0 mmol) of KOH in 10 mL of water. Subsequently, 0.69 g (4.99 mmol) of K_2CO_3 was added, and the solution was stirred at 80 °C for 18 h. The volatiles were removed under reduced pressure. The residue was taken up in 10 mL of methanol, the solution was filtered, and the maroon filtrate was evaporated to dryness. Yield: 1.61 g (54%). ^{1}H NMR (300 MHz, D_2O, δ): 8.41 (d, J = 4.8 Hz, 1H, Ar H), 7.80 (t, J = 6.5 Hz, 1H, Ar H), 7.53 (d, J = 7.8 Hz, 1H, Ar H), 7.31 (t, J = 7.5 Hz, 1H, Ar H), 3.95 (s, 2H, pyridyl CH_2N), 3.28 (s, 4H, NCH_2CO_2K).

***N,N*-Bis(2-benzimidazolylmethyl)-*N*-(2-pyridylmethyl)amine.**[118] A solution of 1.98 g (6.60 mmol) of dipotassium *N*-(2-pyridylmethyl)iminodiacetate and 1.44 g (13.3 mmol) of 1,2-diaminobenzene in 140 mL of 6 M HCl was heated under reflux for three days. Heating was briefly interrupted to add activated carbon, and the solution was heated under reflux for another 10 min. Subsequently, the solution was filtered and treated with an NH_4OH solution (to adjust the pH to 9), which resulted in the formation of a precipitate. The precipitate was separated by filtration and dissolved in 30 mL of chloroform. The organic solution was washed with an aqueous 0.1 M NaOH solution (3 x 20 mL), dried over $MgSO_4$ and evaporated to dryness. The crude product was purified by column chromatography on silica gel using a solution of 1% NEt_3 in acetone as the eluent to afford a brown solid. Yield: 0.26 g (11%). ^{1}H NMR (300 MHz, $CDCl_3$, δ): 8.46 (d, J = 3.5 Hz, 1H, Ar H), 7.58-7.55 (m, 4H, Ar H), 7.41 (m, 1H, Ar H), 7.26-7.17 (m, 5H, Ar H), 7.05-7.03 (m, 1H, Ar H), 4.04 (s, 4H, benzimidazolyl CH_2N), 3.85 (s, 2H, pyridyl CH_2N).

***N,N*-Bis[(1-methylbenzimidazol-2-yl)methyl]-*N*-[(pyridin-2-yl)methyl]amine (L2).** To 200 mg (3.56 mmol) of powdered KOH (prepared under exclusion of moisture) were added a solution of 220 mg (0.60 mmol) of *N,N*-bis(2-benzimidazolylmethyl)-*N*- (2-pyridylmethyl)amine in 10 mL of DMSO and 0.11 mL (0.25 g, 1.77 mmol) of iodomethane. The reaction mixture was stirred for 1 h, after which it was poured into 50 mL of water. The product was extracted with chloroform (3 x 40 mL), and the combined organic phases were washed with water (5 x 40 mL) and dried over $MgSO_4$. The volatiles were removed under reduced pressure to afford a red solid. The crude product was washed with acetone to afford a yellow solid, which was recrystallized from dichloromethane and dried *in vacuo*. Yield: 152 mg (64%). Anal. Calcd for $C_{24}H_{24}N_6$: C, 72.70; H, 6.10; N, 21.20. Found: C, 72.16; H, 5.99; N, 21.06. ^{1}H NMR (300 MHz, $CDCl_3$, δ): 8.56 (m, 1H, Ar H), 7.73 (m, 2H, Ar H), 7.57 (m, 1H, Ar H), 7.27-7.13 (m, 8H, Ar H), 4.09 (s, 4H, benzimidazolyl CH_2N), 3.95 (s, 2H, pyridyl CH_2N), 3.49 (s, 6H,

NCH_3). ^{13}C NMR (75.5 MHz, $CDCl_3$, δ): 157.7, 151.2, 149.1, 142.2, 136.3, 136.0, 124.3, 122.6, 122.3, 121.9, 119.6, 109.0, 60.2 (pyridyl CH_2N), 50.8 (benzimidazolyl CH_2N), 29.5 (NCH_3). EIMS (70 eV) *m/z*: $M^{+\bullet}$ calcd for $C_{24}H_{24}N_6$, 396.21; found, 396.3.

[Fe(L1)(OTf)$_2$]. A solution of 436 mg (1.00 mmol) of $Fe(OTf)_2{\cdot}2MeCN$ in 10 mL of tetrahydrofuran was added to a stirred solution of 350 mg (1.02 mmol) of **L1** in 10 mL of tetrahydrofuran under an N_2 atmosphere. The resulting solution was stirred for 3 h. The solution was concentrated to a volume of 2 mL, and 10 mL of diethyl ether was added to cause the product to precipitate. The product was separated by filtration and recrystallized by vapor diffusion of diethyl ether into a nitromethane solution of the product at −30 °C to yield pale yellow single crystals. The crystalline solid was dried *in vacuo*. Yield: 495 mg (71%). Anal. Calcd for $C_{23}H_{21}F_6FeN_5O_6S_2$: C, 39.61; H, 3.04; N, 10.04; S, 9.20. Found: C, 39.87; H, 3.24; N, 9.76; S, 9.23. ^1H NMR (300 MHz, CD_3CN, δ): 83.1 (br, 2H, pyridyl Ar H), 68.7, (br, 2H, pyridyl CH_2N), 65.8 (br, 2H, pyridyl CH_2N), 56.8 (br, 2H, benzimidazolyl CH_2N), 46.7 (s, 2H, pyridyl Ar H), 42.8 (s, 2H, pyridyl Ar H), 25.0 (s, 1H, benzimidazolyl Ar H), 15.7 (s, 1H, NCH_3) 5-0 (2H, benzimidazolyl Ar H), −4.7 (br, 1H, benzimidazolyl Ar H), −7.8 (s, 2H, pyridyl Ar H). ESI(+)MS ($MeNO_2$) *m/z*: M^+ calcd for $C_{22}H_{21}F_3FeN_5O_3S$ ($[Fe(L1)(OTf)]^+$), 548.07; found, 548.1. Upon dissolution in acetonitrile, [Fe(**L1**)$(OTf)_2$] was converted into [Fe(**L1**)$(NCMe)_2$]$(OTf)_2$. UV−Vis (MeCN) λ_{max}, nm (ε): 375 (1200), 495 (70). Red single crystals of X-ray diffraction quality were obtained by vapor diffusion of diethyl ether into an acetonitrile solution of the product at −30 °C.

[Fe(L2)(OTf)$_2$]. A solution of 436 mg (1.00 mmol) of $Fe(OTf)_2{\cdot}2MeCN$ in 10 mL of tetrahydrofuran was added to a stirred suspension of 404 mg (1.02 mmol) of **L2** in 10 mL of tetrahydrofuran under an N_2 atmosphere. The reaction mixture was stirred for 3 h. The mixture was concentrated to a volume of 2 mL and 10 mL of diethyl ether were added. The precipitate was separated by filtration, and the residue was recrystallized by vapor diffusion of diethyl ether into a nitromethane solution of the product at −30 °C.

Colorless single crystals were obtained and dried *in vacuo*. Yield: 596 mg (79%). Anal. Calcd for $C_{26}H_{24}F_6FeN_6O_6S_2$: C, 41.61; H, 3.22; N, 11.20; S, 8.55. Found: C, 40.80; H, 3.19; N, 10.95; S, 8.67. ^{1}H NMR (300 MHz, CD_3CN, δ): 118.1 (br, 1H, pyridyl Ar H), 99.6, (br, 2H, pyridyl CH_2N), 76.7 (br, 2H, benzimidazolyl CH_2N), 72.3 (br, 2H, benzimidazolyl CH_2N), 55.0 (s, 1H, pyridyl Ar H), 53.5 (s, 1H, pyridyl Ar H), 29.2 (s, 2H, benzimidazolyl Ar H), 19.9 (s, 6H, NCH_3) 5-0 (4H, benzimidazolyl Ar H), −4.8 (br, 2H, benzimidazolyl Ar H), −13.2 (s, 2H, pyridyl Ar H). ESI(+)MS ($MeNO_2$) *m/z*: M^+ calcd for $C_{25}H_{24}F_3FeN_6O_3S$ ($[Fe(L2)(OTf)]^+$), 601.09; found, 601.1. Upon dissolution in acetonitrile, [Fe(**L2**)$(OTf)_2$] was converted into [Fe(**L2**)$(NCMe)_2$]$(OTf)_2$. UV−Vis (MeCN) λ_{max}, nm (ε): 360 (1000), 490 (80). Pale yellow crystals of X-ray diffraction quality were obtained by vapor diffusion of diethyl ether into an acetonitrile solution of the product at −30 °C.

Reaction of [Fe(L1)(OTf)$_2$] and [Fe(L2)(OTf)$_2$] with *m*CPBA. Both Fe^{IV}=O species were prepared according to the general procedure outlined below. A 1 mL solution of 1 mM Fe^{II} complex in acetonitrile was cooled to −40 °C, then 3 equiv of *m*CPBA in acetonitrile were added to this cold solution. The greenish intermediate which forms immediately upon addition of *m*CPBA was monitored by UV−Vis spectroscopy. UV−Vis (MeCN) λ_{max}, nm (ε): 733 (230) for [Fe(**L1**)$(OTf)_2$] and 747 (220) for [Fe(**L2**)$(OTf)_2$].

Reaction of [Fe(L1)(OTf)$_2$] and [Fe(L2)(OTf)$_2$] with AcOOH. Both Fe^{IV}=O species could also be prepared by using peracetic acid with slightly lower yield. A 1 mL solution of 1 mM Fe^{II} complex in acetonitrile was cooled to −40 °C, and then 5 equiv of AcOOH in acetonitrile were added to this cold solution. The greenish intermediate which forms immediately upon addition of AcOOH was used for ESI mass spectroscopic measurements. Although higher yields were obtained with *m*CPBA according to UV−Vis spectroscopy, the ESI mass spectra were not satisfactory. Therefore, all the Fe^{IV}=O species monitored by ESI mass spectrometry were generated by peracetic acid. For

[Fe(**L1**)$(OTf)_2$], ESI(+)MS *m*/*z*: M^+ calcd for $C_{22}H_{21}F_3FeN_5O_4S$, 564.04; found, 563.9 $\{[Fe(\mathbf{L1})(OTf)] + O\}^+$, 227.9 $\{[Fe(\mathbf{L1})] + O + MeCN\}^{2+}$, 207.8 $\{[Fe(\mathbf{L1})] + O\}^{2+}$; For [Fe(**L2**)$(OTf)_2$], ESI(+)MS *m*/*z*: M^+ calcd for $C_{25}H_{24}F_3FeN_6O_4S$, 617.09; found, 616.9 $\{[Fe(\mathbf{L2})(OTf)] + O\}^+$, 254.5 $\{[Fe(\mathbf{L2})] + O + MeCN\}^{2+}$, 234.6 $\{[Fe(\mathbf{L2})] + O\}^{2+}$.

X-ray Crystallographic Analyses. A single crystal of each compound was coated with Paratone N oil and mounted on a glass capillary for data collection at 190(2) K for [Fe(**L1**)$(NCMe)_2$]$(OTf)_2$ and 210(2) K for [Fe(**L2**)$(NCMe)_2$]$(OTf)_2$ on a Nonius KappaCCD diffractometer using Mo *Kα* radiation (graphite monochromator). The temperature was controlled by an Oxford Cryostream Cooler (700 series, N_2 gas). Data collection, data reduction, and absorption correction were carried out following standard CCD techniques using the software packages Collect and HKL-2000.[69,70] Final cell constants were calculated from 5312 ([Fe(**L1**)$(NCMe)_2$]$(OTf)_2$) or 6279 [Fe(**L2**)$(NCMe)_2$]$(OTf)_2$ reflections from the complete data set. The space groups *P*–1 ([Fe(**L1**)$(NCMe)_2$]$(OTf)_2$) and *P*–1 ([Fe(**L2**)$(NCMe)_2$]$(OTf)_2$) were determined based on systematic absences and intensity statistics. The structures were solved by direct methods and refined by full-matrix least-squares minimization and difference Fourier methods (SHELXTL v.6.12).[71,72] All non-hydrogen atoms were refined with anisotropic displacement parameters. Severe disorder of the triflate anion in both complexes led to a less satisfactory *R* values, but the cations in both compounds are well defined. In [Fe(**L1**)$(NCMe)_2$]$(OTf)_2$, one of the two triflate anions was modelled with two components (74.0:26.0).The final full-matrix least-squares refinement converged to $R1$ = 0.222 and $wR2$ = 0.230 [F^2, all data]. For [Fe(**L2**)$(NCMe)_2$]$(OTf)_2$, the final full-matrix least-squares refinement converged to $R1$ = 0.103 and $wR2$ = 0.190 [F^2, all data]. Table A1 contains additional crystal and refinement information. Selected distances and angles are summarized in Tables A2 and A3.

Table A1. Crystallographic data and structure refinement for [Fe(**L1**)$(NCMe)_2$]$(OTf)_2$, and [Fe(**L2**)$(NCMe)_2$]$(OTf)_2$.

	[Fe(**L1**)$(NCMe)_2$]$(OTf)_2$	[Fe(**L2**)$(NCMe)_2$]$(OTf)_2$
Empirical formula	$C_{27}H_{27}F_6FeN_7O_6S_2$	$C_{30}H_{30}F_6FeN_8O_6S_2$
Formula weight	779.53	832.59
Crystal habit, color	bar, red orange	plate, colorless
Crystal size	0.175 x 0.085 x 0.035 mm^3	0.22 x 0.14 x 0.065 mm^3
Temperature, T	210(2) K	190(2) K
Wavelength, λ	0.71073 Å	0.71073 Å
Crystal system	triclinic	triclinic
Space group	$P\bar{1}$	$P\bar{1}$
Unit cell dimensions	a = 12.471(2) Å	a = 12.3355(13) Å
	b = 12.830(2) Å	b = 12.7095(14) Å
	c = 13.1212(19) Å	c = 13.1623(14) Å
	α = 82.376(13)°	α = 77.697(5)°
	β = 61.747(10)°	β = 77.568(5)°
	γ = 63.388(9)°	γ = 64.714(5)°
Volume, V	1645.0(4) $Å^3$	1804.9(3) $Å^3$
Z	2	2
Calculated density	1.574 $Mg \cdot m^{-3}$	1.532 $Mg \cdot m^{-3}$
Absorption coefficient, μ	0.671 mm^{-1}	0.618 mm^{-1}
F(000)	796	852
θ range for data collection	3.13 to 25.28°	2.85 to 25.37°
Limiting indices	$-14 \le h \le 14$, $-15 \le k \le 15$, $-15 \le l \le 15$	$-14 \le h \le 14$, $-15 \le k \le 15$, $-15 \le l \le 14$
Reflections collected / unique	10922 / 5903 [R(int) = 0.1087]	12094 / 6577 [R(int) = 0.0306]
Completeness to θ	98.8 % (θ = 25.28°)	99.2 % (θ = 25.37°)
Refinement method	Full-matrix least-squares on F^2	Full-matrix least-squares on F^2
Data / restraints / parameters	5903 / 20 / 464	6577 / 0 / 482
Goodness-of-fit on F^2	1.032	1.030
Final R indices [I>2sigma(I)]	$R1$ = 0.0969, $wR2$ = 0.1813	$R1$ = 0.0660, $wR2$ = 0.1656
R indices (all data)	$R1$ = 0.2216, $wR2$ = 0.2296	$R1$ = 0.1026, $wR2$ = 0.1901
Largest diff. peak and hole	0.576 and -0.357 $e \cdot A^{-3}$	0.953 and -0.566 $e \cdot A^{-3}$

Table A2. Selected interatomic distances (Å) for [Fe(**L1**)(NCMe)$_2$](OTf)$_2$ and [Fe(**L2**)(NCMe)$_2$](OTf)$_2$.[a]

	[Fe(**L1**)(NCMe)$_2$](OTf)$_2$		[Fe(**L2**)(NCMe)$_2$](OTf)$_2$
Fe–N1	2.019(6)	Fe–N1	2.296(4)
Fe–N2	1.967(6)	Fe–N2	2.177(4)
Fe–N3	1.992(6)	Fe–N3	2.142(3)
Fe–N5	1.976(6)	Fe–N5	2.115(4)
Fe–N6	1.966(7)	Fe–N7	2.198(4)
Fe–N7	1.924(8)	Fe–N8	2.127(4)

[a] Numbers in parentheses are standard uncertainties in the last significant figures. Atoms are labeled as indicated in Figures A5 and A6.

Table A3. Selected interatomic angles (°) for [Fe(**L1**)(NCMe)$_2$](OTf)$_2$ and [Fe(**L2**)(NCMe)$_2$](OTf)$_2$.[a]

[Fe(**L1**)(NCMe)$_2$](OTf)$_2$		[Fe(**L2**)(NCMe)$_2$](OTf)$_2$	
N(7)-Fe-N(6)	88.8(3)	N(5)-Fe-N(8)	111.65(15)
N(7)-Fe-N(2)	95.8(3)	N(5)-Fe-N(3)	86.94(13)
N(6)-Fe-N(2)	90.3(2)	N(8)-Fe-N(3)	96.92(13)
N(7)-Fe-N(5)	97.4(3)	N(5)-Fe-N(2)	151.40(15)
N(6)-Fe-N(5)	88.0(2)	N(8)-Fe-N(2)	96.88(15)
N(2)-Fe-N(5)	166.7(3)	N(3)-Fe-N(2)	91.73(13)
N(7)-Fe-N(3)	95.4(3)	N(5)-Fe-N(7)	88.38(14)
N(6)-Fe-N(3)	175.8(3)	N(8)-Fe-N(7)	89.64(14)
N(2)-Fe-N(3)	89.6(2)	N(3)-Fe-N(7)	173.01(14)
N(5)-Fe-N(3)	91.1(2)	N(2)-Fe-N(7)	89.89(13)
N(7)-Fe-N(1)	178.9(3)	N(5)-Fe-N(1)	77.39(14)
N(6)-Fe-N(1)	91.9(2)	N(8)-Fe-N(1)	169.94(14)
N(2)-Fe-N(1)	83.4(2)	N(3)-Fe-N(1)	78.74(13)
N(5)-Fe-N(1)	83.5(3)	N(2)-Fe-N(1)	74.35(14)
N(3)-Fe-N(1)	83.9(2)	N(7)-Fe-N(1)	95.16(13)

[a] Numbers in parentheses are standard uncertainties in the last significant figures. Atoms are labeled as indicated in Figures A5 and A6.

A.3 Results and Discussion

A.3.1 Synthesis of Tripodal Ligands and Iron(II) Complexes

Two tetradentate tripodal ligands (**L1** and **L2**), derivatives of tpa and Me_3ntb; where tpa = tris (pyridylmethyl)amine, Me_3ntb = tris(2-benzimida`zolylmethyl)amine; have been synthesized to provide a systematic variation on the ligand. The structures of the ligands are shown in Scheme A1, together with their abbreviations.

Scheme A1. Structures of the Tripodal Ligands.

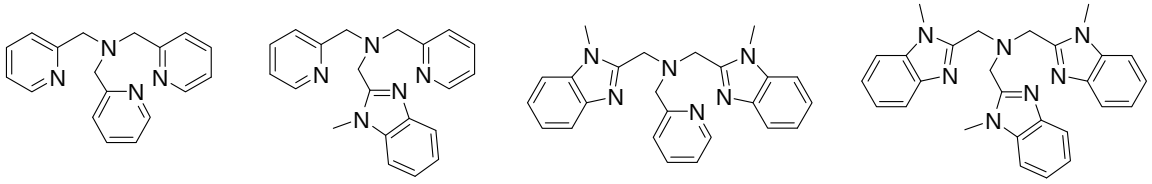

Three steps were required for the synthesis of each ligand (Scheme A2 and A3). In general, two synthetic routes for each ligand (**L1** and **L2**) may be considered. The reaction sequences of two different kinds of reactions, substitution and condensation, resulted in dramatically different outcomes. The synthetic route for **L1** was utilized by condensation prior to substitution. However, the opposite pathway in which substitution preceded condensation was used in preparing **L2**. In fact, **L2** is a new ligand, and it is worth noting that while **L1** and its Mn^{II} complex were previously reported, but no experimental details were given.[121]

Other routes for the synthesis of **L1** and **L2** were also considered and executed (Scheme A4 and A5). For both routes, the first step could result in reasonable yields, but only low yields could be obtained in the second step.

Scheme A2. Synthetic Routes for **L1**.

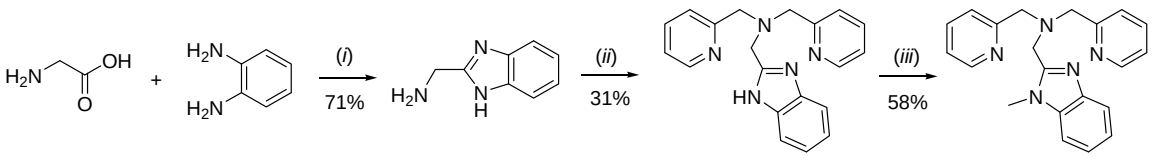

(i) 7 M HCl, reflux, 3 d; (ii) 2 equiv of 2-(chloromethyl)pyridine hydrochloride, NEt_3, 0 → 20 °C, 3 d; (iii) KOH, MeI, 20 °C, 1 h

Scheme A3. Synthetic Routes for **L2**.

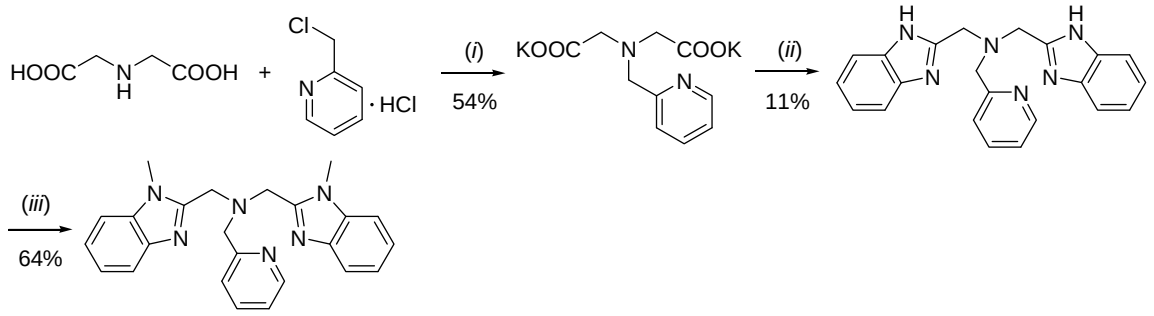

(i) KOH, K_2CO_3, 0 → 80 °C, 18 h; (ii) 2 equiv of 1,2-diaminobenzene, 6 M HCl, reflux, 3 d; (iii) KOH, MeI, 20 °C, 1 h

Scheme A4. Other Synthetic Route for **L1**.

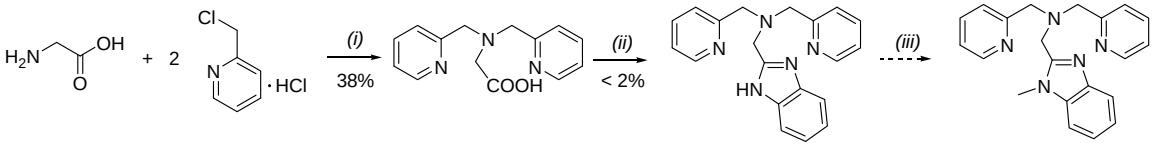

(i) NaOH, 20 °C, 5 d;[122] (ii) 1,2-diaminobenzene, 6 M HCl, reflux, 3 d, 2% yield;[118] (iii) KOH, MeI, 20 °C, 1 h

Scheme A5. Other Synthetic Route for **L2**.

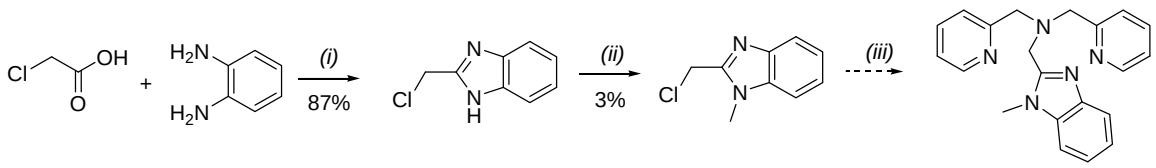

(i) ethylene glycol, 180 °C, 1 d;[123] b) 2-(chloromethyl)pyridine hydrochloride, K_2CO_3, 20 °C, 3 d; c) KOH, MeI, 20 °C, 1 h

The Fe^{II} complexes, [Fe(**L1**)$(OTf)_2$] and [Fe(**L2**)$(OTf)_2$], were synthesized by mixing $Fe(OTf)_2$·2MeCN with **L1** and **L2** in THF at ambient temperature, respectively. The complexes were isolated as microcrystalline solids, and characterized by ^{1}H NMR and UV−Vis spectroscopy, mass spectrometry, elemental analysis, and single-crystal X-ray diffraction. The solid state structures of [Fe(**L1**)$(NCMe)_2$]$(OTf)_2$ and [Fe(**L2**)$(NCMe)_2$]$(OTf)_2$, obtained from dissolving of [Fe(**L1**)$(OTf)_2$] and [Fe(**L2**)$(OTf)_2$] in MeCN, were crystallographically determined. Each Fe^{II} ion exhibits a FeN6 coordination environment with four nitrogen atoms from tetradentate ligand, **L1** or **L2**, and two nitrogen atoms belonging to two MeCN to yield octahedral complexes.

A.3.2 Spectroscopic Characterization of Iron(II) Complexes

The ^{1}H NMR spectrum of [Fe(tpa)$(OTf)_2$] in CD_3CN at room temperature exhibits features of a diamagnetic species, demonstrating that the Fe^{II} center in $[Fe(tpa)(NCCD_3)_2]^{2+}$ is low spin, S = 0 (Figure A2, Table A4). Unlike the low-spin complex $[Fe(tpa)(NCCD_3)_2]^{2+}$, complexes $[Fe(\mathbf{L1})(NCCD_3)_2]^{2+}$ and $[Fe(\mathbf{L2})(NCCD_3)_2]^{2+}$ have ^{1}H NMR spectra typical of a high-spin Fe^{II} complexes with peaks paramagnetically shifted over the range of −10 to +120 ppm (Figure A2, Table A4). These peaks can be assigned by comparison to the spectra of other high-spin complexes, [Fe(tpa)$(OTf)_2$] in $CDCl_3$ and [Fe(Me_3ntb)$(NCCD_3)_2$]$(OTf)_2$ in the literature.[124] Thus, the replacement of

even one of the pyridyl substituents in the tripodal ligand with a benzimidazolyl substituent is sufficient to change the Fe^{II} center from low spin to high spin in the $[Fe^{II}(\mathbf{L})(NCCH_3)_2]^{2+}$ series at ambient temperature.

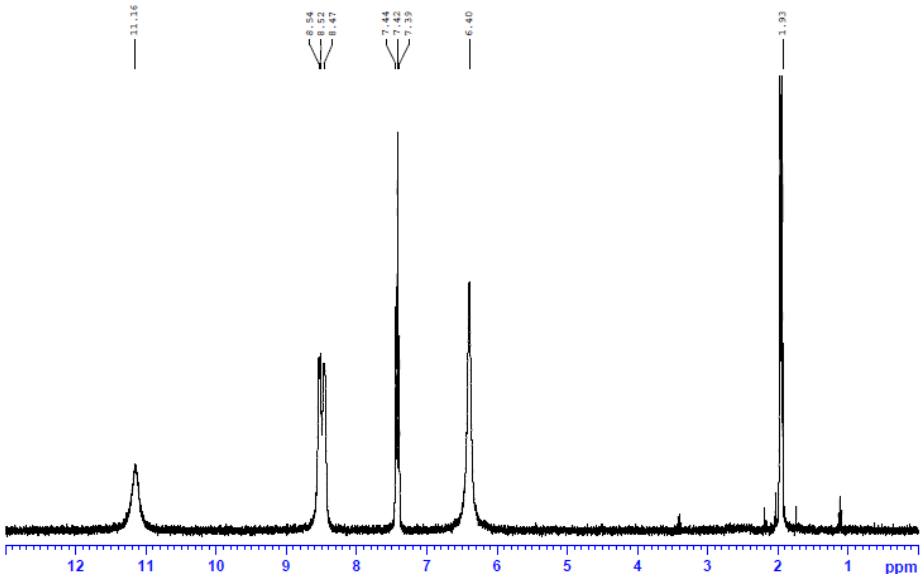

Figure A1. ^{1}H NMR spectrum of $[Fe(tpa)(NCMe)_2]^{2+}$ in CD_3CN at room temperature.

Considering the results from ^{1}H NMR spectroscopy (narrower range, similar to $[Fe(tpa)(OTf)_2]$), the high-spin complex, $[Fe(\mathbf{L1})(NCMe)_2](OTf)_2$, could be able to transform to a low-spin Fe^{II} complex at lower temperature. Therefore, $[Fe(\mathbf{L1})(NCCD_3)_2](OTf)_2$ was studied by variable temperature ^{1}H NMR spectroscopy in the temperature range of −40 to +80 °C (Figure A3). The spectra show that the range of resonances expanded from 20 to 85 ppm with increasing temperature from –40 to +50 °C and becomes narrower again above +50 °C. Therefore, the variable temperature NMR experiment shows that $[Fe(\mathbf{L1})(NCCD_3)_2](OTf)_2$ in acetonitrile exhibits a mixture of high- and low-spin species in the temperature range of –40 to +50 °C, and transforms to pure high-spin at a temperature of *ca.* 50 °C. For comparison, $[Fe(\mathbf{L2})(NCCD_3)_2](OTf)_2$

was acquired by variable temperature ^{1}H NMR spectroscopy in the same temperature range (Figure A4). The spectra show that the range of resonances shrinks from 160 to 100 ppm with increasing temperature from –40 to +80 °C. Unlike expansion and then shrinkage for [Fe(**L1**)$(NCCD_3)_2$]$(OTf)_2$, only shrinking ^{1}H NMR spectra of [Fe(**L2**)$(NCCD_3)_2$]$(OTf)_2$ was observed, indicating that [Fe(**L2**)$(NCCD_3)_2$]$(OTf)_2$ remains high-spin in this temperature range.

Table A4. ^{1}H chemical shifts, δ (ppm), of the Fe^{II} complexes $[Fe(tpa)(NCMe)_2]^{2+}$, $[Fe(\mathbf{L1})(NCMe)_2]^{2+}$, $[Fe(\mathbf{L2})(NCMe)_2]^{2+}$, and $[Fe(Me_3ntb)(NCMe)]^{2+}$.

	α-H 6-H_{py}	NCH_2	β-H, β'-H 3-H_{py}, 5-H_{py}			γ-H 4-H_{py}
$[Fe(tpa)(NCCD_3)_2]^{2+}$ [a]	3H, 11.2	6H, 6.40	6H, 8.52, 8.47			3H, 7.42
$[Fe(tpa)(OTf)_2]$ [b]	n. o.[c]	6H, 64.8	6H, 52.7, 51.4			3H, 10.3
$[Fe(\mathbf{L1})(NCCD_3)_2]^{2+}$ [a]	2H, 86.8	4H, 71.2, 68.3	4H, 48.2, 44.3			2H, –8.1
$[Fe(\mathbf{L2})(NCCD_3)_2]^{2+}$ [a]	1H, 115.8	2H, 96.8	2H, 54.1, 52.6			2H, –12.8
	NCH_2	Ar H 7-H_{bzim}	NCH_3	Ar H 5-H_{bzim}	Ar H 6-H_{bzim}	Ar H 4-H_{bzim}
$[Fe(\mathbf{L1})(NCCD_3)_2]^{2+}$ [a]	2H, 59.5	1H, 25.8	3H, 16.1	1H, 3.8	1H, 2.2	1H, –5.3
$[Fe(\mathbf{L2})(NCCD_3)_2]^{2+}$ [a]	4H, 75.8, 71.2	2H, 28.7	6H, 19.6	2H, 3.2	2H, 1.3	2H, –4.0
$[Fe(Me_3ntb)(NCCD_3)]^{2+}$ [a]	6H, 83.2	3H, 27.1	9H, 18.5	3H, 4.3	3H, 1.7	(*ca.* 3.5)[d]

[a] In CD_3CN. [b] In $CDCl_3$. [c] n. o. = not observed. [d] This resonance overlaps with the resonance at 4.3 ppm.

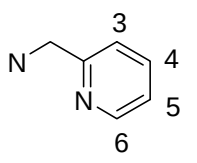

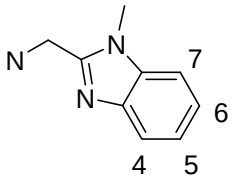

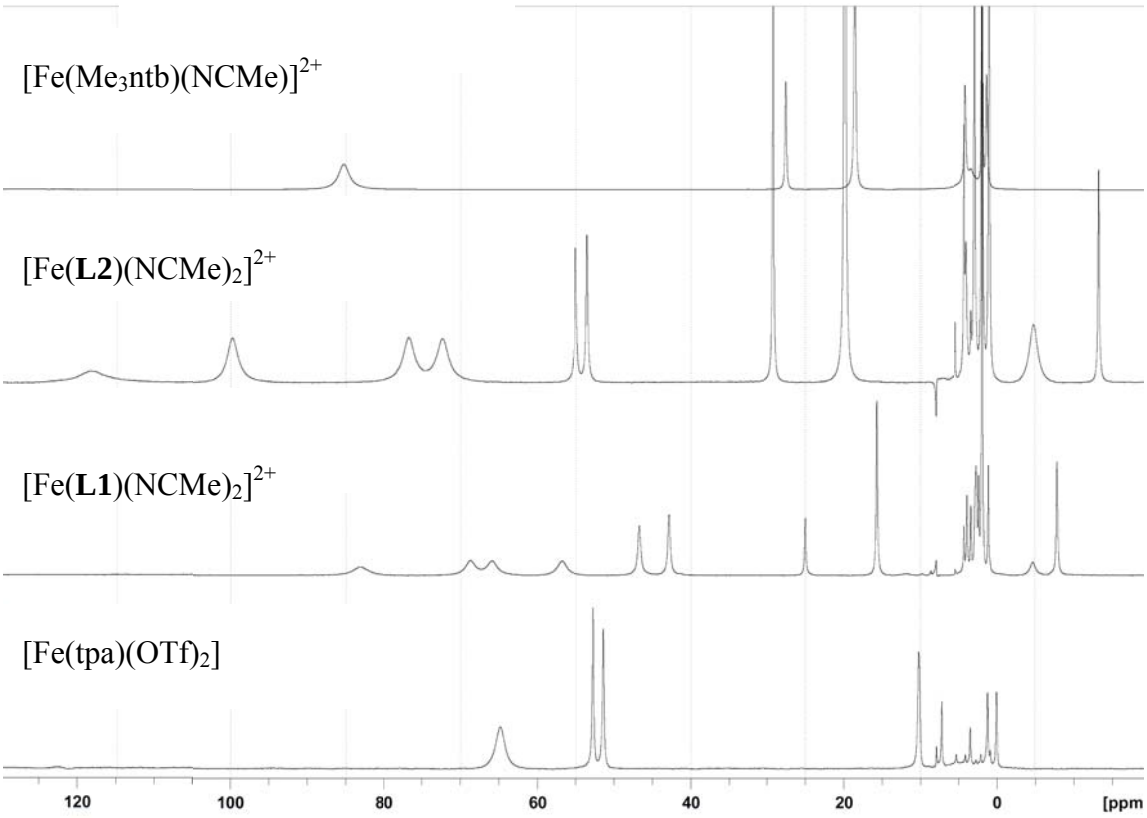

Figure A2. ^{1}H NMR spectra of [Fe(tpa)(OTf)$_2$] in $CDCl_3$ and [Fe(**L1**)(NCMe)$_2$]$^{2+}$, [Fe(**L2**)(NCMe)$_2$]$^{2+}$, and [Fe(Me$_3$ntb)(NCMe)]$^{2+}$ in CD_3CN at room temperature.

A.3.3 Crystal Structures of Iron(II) Complexes

The Fe^{II} center in each complex is in a distorted octahedral environment ligated by the two/one pyridine nitrogen(s), one/two benzoimidazole nitrogen(s) and one amine nitrogen of the tripodal ligand, and two acetonitrile nitrogens (Figures A5 and A6). Although [Fe(**L1**)(NCMe)$_2$](OTf)$_2$ and [Fe(**L2**)(NCMe)$_2$](OTf)$_2$ have similar coordination geometries, the Fe−N bond lengths and bond angles differ greatly between these two complexes, reflecting the difference in spin state (Tables A2 and A3). For example, although Fe−N$_{amine}$ distance in both complexes is longer than the other Fe−N

bonds, the Fe−N_{amine} distance of 2.033(4) Å in [Fe(**L1**)$(NCMe)_2$]$(OTf)_2$ is significantly shorter than the Fe−N_{amine} distance of 2.303(5) Å in [Fe(**L2**)$(NCMe)_2$]$(OTf)_2$.

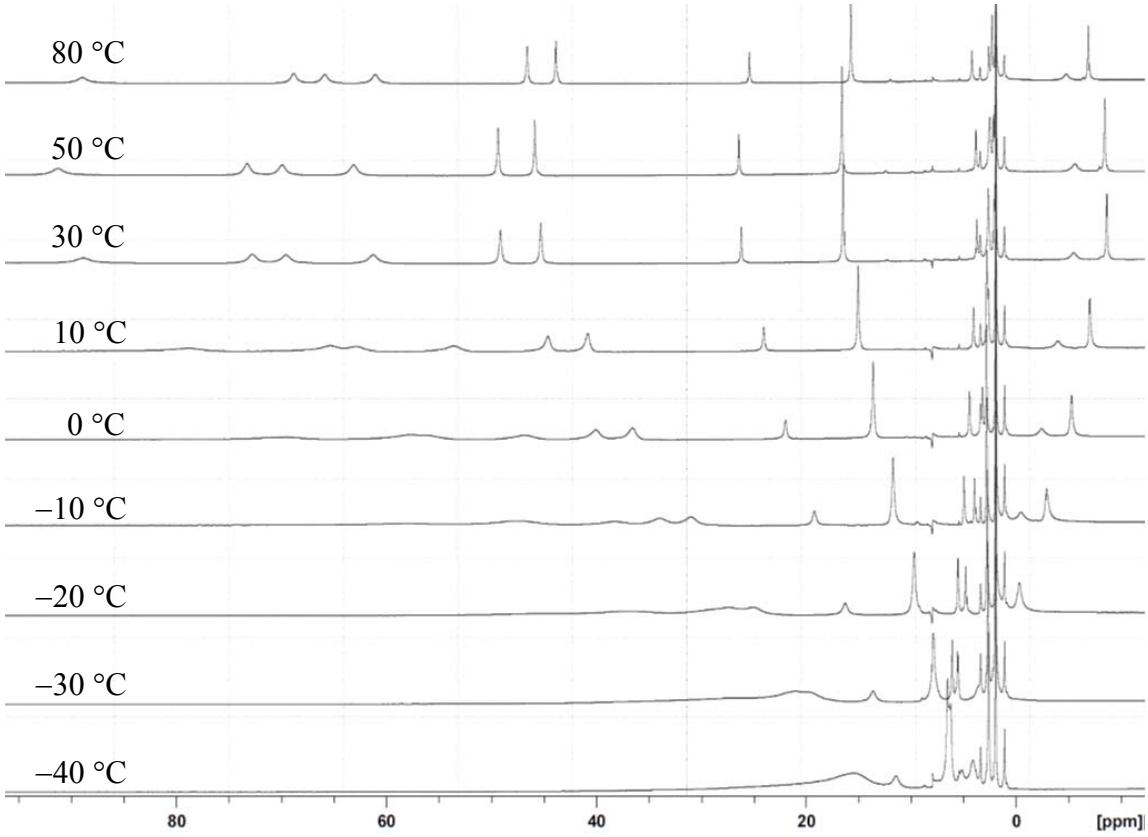

Figure A3. VT ^{1}H NMR spectra of [Fe(**L1**)$(NCCD_3)_2$]$^{2+}$ in CD_3CN in the temperature range of −40 to +80 °C.

Likewise, the Fe−N_{py}, Fe−N_{bzim}, and Fe−N_{MeCN} bond lengths of [Fe(**L1**)$(NCMe)_2$]$(OTf)_2$ are 0.20−0.21 Å, 0.12−0.15 Å, and 0.16−0.27 Å shorter than the corresponding Fe−N distances in [Fe(**L2**)$(NCMe)_2$]$(OTf)_2$, respectively. The Fe−N distances reflect different chemical nature of the donor atoms. With the similar Fe−N bond lengths in [Fe(**L1**)$(NCMe)_2$]$(OTf)_2$, this complex is expected to be a low-spin Fe^{II}

complex. Moreover, the average Fe–N_{py} distance of 1.97 Å found in [Fe(**L1**)$(NCMe)_2$]$(OTf)_2$ is comparable to those typically found in low-spin Fe^{II} complexes, such as $[Fe(phen)_3]^{2+}$ (1.97 Å),[125] $[Fe(bpy)_3]^{2+}$ (1.96 Å),[126] $[Fe(tpa)(NCMe)_2]^{2+}$ (1.95 Å).[127] On the contrary, with a noticeably longer Fe–N_{amine} bond length than Fe–N_{bzim}, Fe–N_{MeCN}, and Fe–N_{py} (0.10 to 0.18 Å), [Fe(**L2**)$(NCMe)_2$]$(OTf)_2$ is expected to be a high-spin Fe^{II} complex.

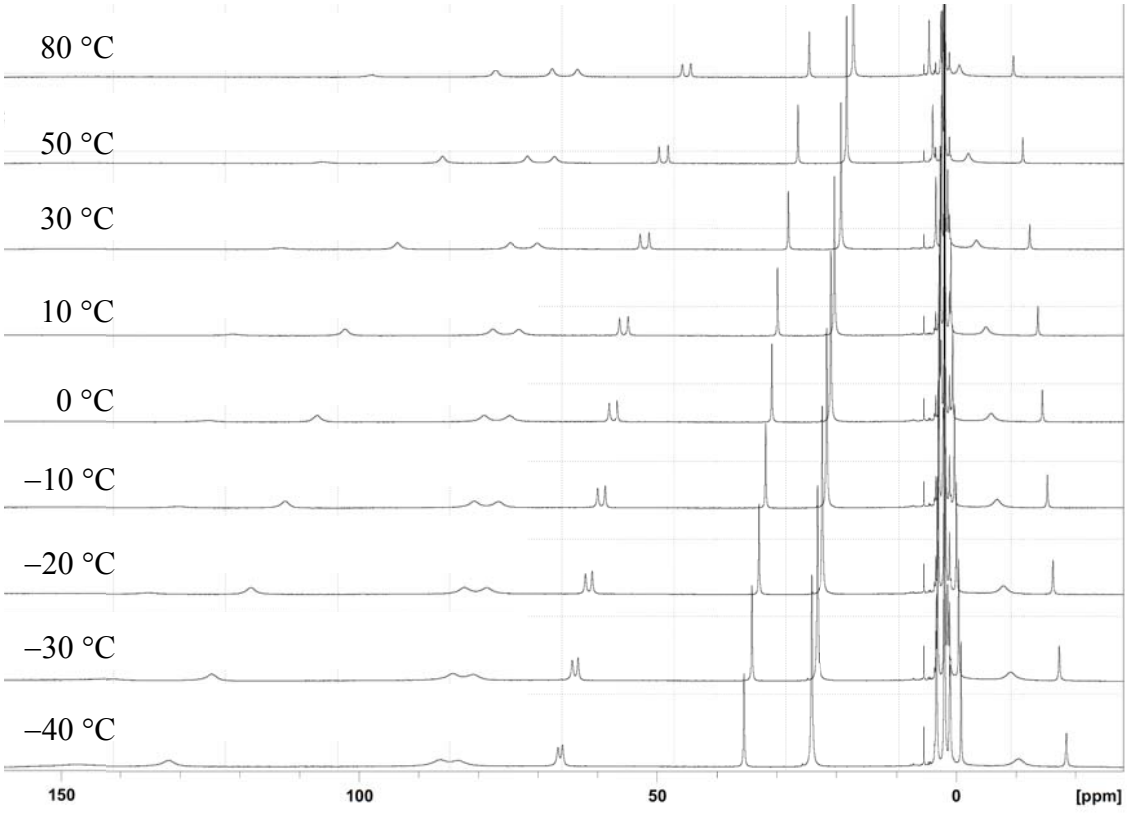

Figure A4. VT-^{1}H NMR spectra of [Fe(**L2**)$(OTf)_2$] in CD_3CN in the temperature range of −40 to +80 °C.

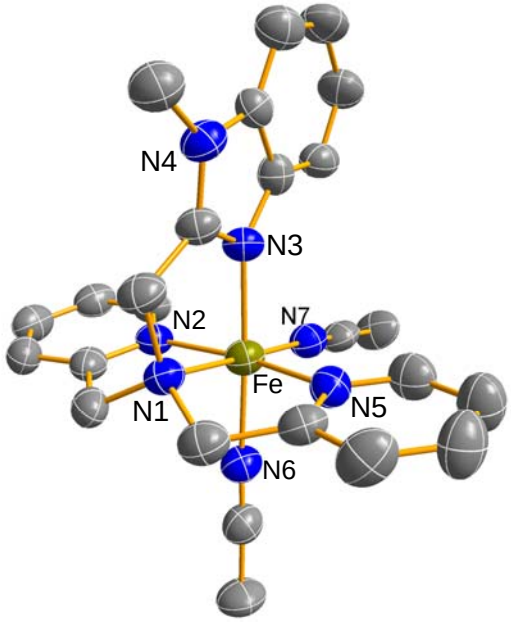

Figure A5. Molecular structure of the complex cation of [Fe(**L1**)(NCMe)$_2$](OTf)$_2$; displacement ellipsoids are drawn at 50% probability level; hydrogen atoms have been omitted for clarity.

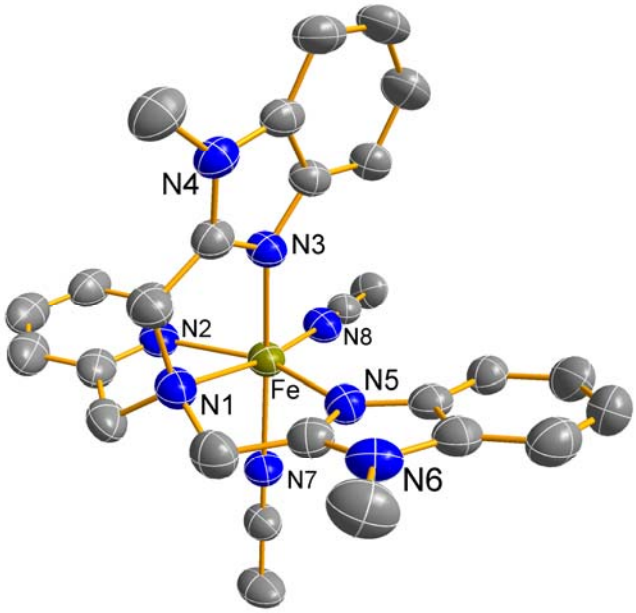

Figure A6. Molecular structure of the complex cation of [Fe(**L2**)(NCMe)$_2$](OTf)$_2$; displacement ellipsoids are drawn at 50% probability level; hydrogen atoms have been omitted for clarity.

A.3.4 Generation and Characterization of Oxoiron(IV) Complexes

Addition of 3 equiv of *m*-chloroperbenzoic acid (*m*CPBA) to a solution containing 1 mM of [Fe(**L1**)$(OTf)_2$] and [Fe(**L2**)$(OTf)_2$] immediately gave pale greenish solution with absorption bands at 733 nm ($\varepsilon \approx 220$ $M^{-1}\cdot cm^{-1}$) and 747 nm ($\varepsilon \approx 200$ $M^{-1}\cdot cm^{-1}$), respectively, in CH_3CN at –40 °C (Figures A7 and A8). Compared to [Fe(tpa)$(OTf)_2$] under the same reaction conditions, the intermediates were unstable and decayed faster (decay began at 10 min and 1 min for [Fe(**L1**)$(OTf)_2$] and [Fe(**L2**)$(OTf)_2$], respectively). Due to the fast decay of Fe^{IV}=O intermediates, growing single crystals of both intermediates for characterization is extremely challenging. Electrospray ionization mass spectrometer would be the suitable instrument for analyzing this type of species. However, when subjecting the solutions generated from Fe^{II} + *m*CPBA into mass spectrometer, no ion peaks represented Fe^{IV}=O could be observed, which may be due to acceleration of decomposition of Fe^{IV}=O by *m*CBA (hydroxylation of the aromatic ring of *m*CBA to form the corresponding Fe^{III} product).[128] Hence, using other oxidants, which may prevent activation of C–H bonds, could help us obtain the desired results. As described in the Experimental Section, peracetic acid could also be used for preparing the Fe^{IV}=O intermediate with slightly lower yield. Therefore, in order to clarify the identification of peaks in mass spectra, peracetic acid was used instead of *m*CPBA. The ESI(+)MS spectrum of [Fe(**L2**)$(OTf)_2$] exhibits overlapping ion peaks, whose mass and isotope distribution patterns correspond to $[Fe^{IV}(O)(\mathbf{L2})(OTf)]^+$ and $[Fe^{III}(OH)(\mathbf{L2})(OTf)]^+$ at *m/z* = 617.9 and 618.9, respectively in addition with other decay product, Fe^{III} species, *i.e. m/z* = 1276.7, $\{2\ [Fe(\mathbf{L2})] + 2\ OTf + OAc + O\}^+$. The $[Fe^{III}(OH)(\mathbf{L2})(OTf)]^+$ likely forms from the decomposition of $[Fe^{IV}(O)(\mathbf{L2})(OTf)]^+$.

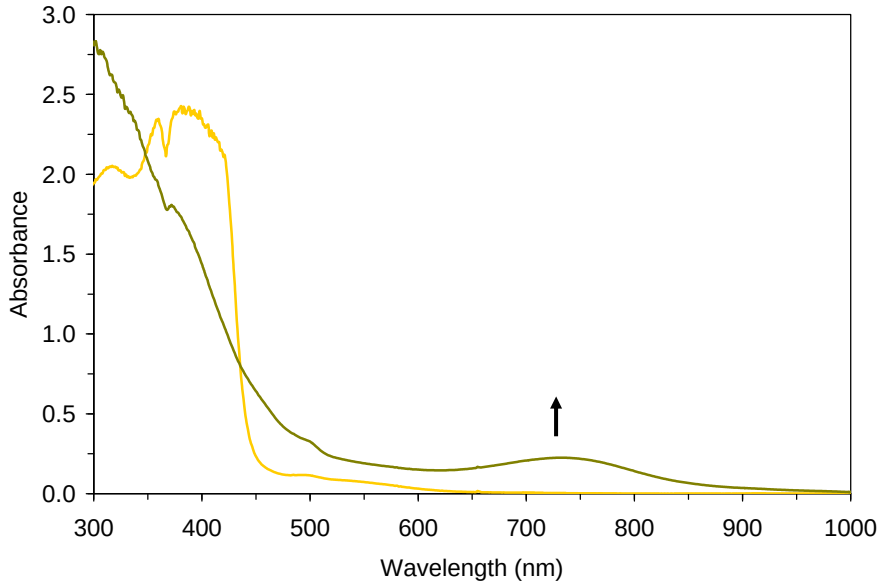

Figure A7. UV–Vis spectra of 1 mM of $[Fe(\mathbf{L1})(NCMe)_2]^{2+}$ (yellow) and $[Fe^{IV}(O)(\mathbf{L1})(NCMe)_2]^{2+}$ (green) in CH_3CN at –40 °C.

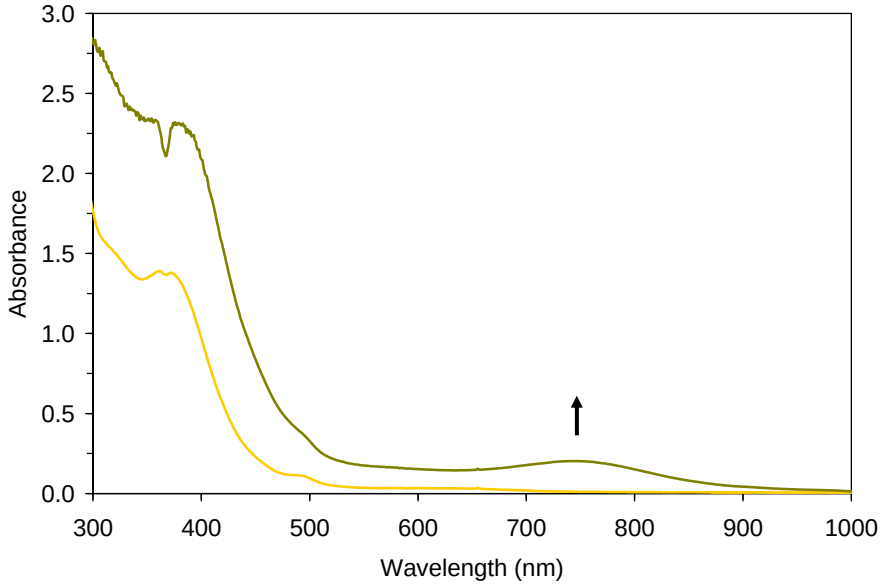

Figure A8. UV–Vis spectra of 1 mM of $[Fe(\mathbf{L2})(NCMe)_2]^{2+}$ (yellow) and $[Fe^{IV}(O)(\mathbf{L2})(NCMe)_2]^{2+}$ (green) in CH_3CN at –40 °C.

A.4 Conclusion

Two Fe^{II} complexes having tripodal tetradentate ligands, *N*-[(1-Methyl-benzimidazol-2-yl)methyl]-*N,N*-bis[(pyridin-2-yl)methyl]amine (**L1**) or *N,N*-Bis[(1-methylbenzimidazol-2-yl)methyl]-*N*-[(pyridin-2-yl)methyl]amine (**L2**) have been prepared and characterized in both solution and solid states. Spectroscopic analyses suggest that the spin states of $[Fe(\mathbf{L1})(NCMe)_2]^{2+}$ and $[Fe(\mathbf{L2})(NCMe)_2]^{2+}$ are high-spin (S = 2) in solution, but low-spin (S = 0) and high-spin in the solid state, respectively. $[Fe(\mathbf{L2})(NCMe)_2]^{2+}$ in acetonitrile exhibits spin equilibrium between low-spin and high-spin over the temperature range from –40 to 50 °C. This study provides the structural basis that replacing pyridyl with benzimidazolyl substituents could change the spin state and also tune the reactivity of Fe centers, which is demonstrated by the formation and stability of Fe^{IV}=O species.

REFERENCES

1. Alaimo, P. J.; Bergman, R. G. *Organometallics* **1999**, *18*, 2707.

2. Klei, S. R.; Tilley, T. D.; Bergman, R. G. *J. Am. Chem. Soc*. **2000**, *122*, 1816.

3. Kawamura, K.; Hartwig, J. F. *J. Am. Chem. Soc.* **2001**, *123*, 8422.

4. Young, K. J. H.; Mironov, O. A.; Periana, R. A. *Organometallics* **2007**, *26*, 2137.

5. Fortner, K. C.; Laitar, D. S.; Muldoon, J.; Pu, L.; Braun-Sand, S. B.; Wiest, O.; Brown, S. N. *J. Am. Chem. Soc*. **2007**, *129*, 588.

6. McDaniel, N. D.; Coughlin, F. J.; Tinker, L. L.; Bernhard, S. *J. Am. Chem. Soc.* **2008**, *130*, 210.

7. Hull, J.; Balcells, D.; Blakemore, J.; Incarvito, C.; Eisenstein, O.; Brudvig, G.; Crabtree, R. H. *J. Am. Chem. Soc.* **2009**, *131*, 8730.

8. Zhou, M.; Schley, N. D.; Crabtree, R. H. *J. Am. Chem. Soc.* **2010**, *132*, 12550.

9. Blakemore, J. D.; Schley, N. D.; Balcells, D.; Hull, J. F.; Olack, G. W.; Incarvito, C. D.; Eisenstein, O.; Brudvig, G. W.; Crabtree, R. H. *J. Am. Chem. Soc.* **2010**, *132*, 16017.

10. Brewster, T. P.; Blakemore, J. D.; Schley, N. D.; Incarvito, C. D.; Hazari, N; Brudvig, G. W.; Crabtree R. H. *Organometallics*, **2011**, *30*, 965.

11. Connelly, N. G.; Geiger, W. E. *Chem. Rev.* **1996**, *96*, 877.

12. Song, N.; Stanbury, D. M. *Inorg. Chem.* **2008**, *47*, 11458.

13. Diversi, P.; Iacoponi, S.; Ingrosso, G.; Laschi, F.; Lucherini, A.; Pinzino, C.; Uccello-Barretta, G.; Zanello, P. *Organometallics* **1995**, *14*, 3275.

14. Fooladi, E.; Graham, T.; Turner, M. L.; Dalhus, B.; Maitlis, P. M.; Tilset, M. *J. Chem. Soc., Dalton Trans.* **2002**, 975.

15. Strout, D. L.; Zari'c, S.; Niu, S.; Hall, M. B. *J. Am. Chem. Soc.* **1996**, *118*, 6068.

16. Hille, R. *Chem. Rev.* **1996**, *96*, 2757.

17. Holm, R. H.; Kennepohl, P.; Solomon, E. I. *Chem. Rev.* **1996**, *96*, 2239.

18. Holm, R. H. *Chem. Rev.* **1987**, *87*, 1401.

19. Gulliver, D. J.; Levason, W. *Coord. Chem. Rev.* **1982**, *46*, 1.

20. Yellowlees, L. J.; MacNamara, K. G. In *Comprehensive Coordination Chemistry II*; McCleverty, J. A.; Meyer, T. J., Eds.; Elsevier: Oxford, U.K., 2004; Vol. 6, pp 147–246.

21. Tensfeldt, D.; Preetz, W. *Z. Naturforsch., B: Chem. Sci.* **1984**, *39b*, 1185.

22. Preetz, W.; Steinebach, H.-J. *Z. Naturforsch., B: Chem. Sci.* **1985**, *40b*, 745.

23. Isobe, K.; Vazquez de Miguel, A.; Nutton, A.; Maitlis, P. M. *J. Chem. Soc., Dalton Trans.* **1984**, 929.

24. McGhee, W. D.; Foo, T.; Hollander, F. J.; Bergman, R. G. *J. Am. Chem. Soc.* **1988**, *110*, 8543.

25. Hay-Motherwell, R. S.; Wilkinson, G.; Hussain-Bates, B.; Hursthouse, M. B. *Polyhedron* **1991**, *10*, 1457.

26. Hay-Motherwell, R. S.; Wilkinson, G.; Hussain-Bates, B.; Hursthouse, M. B. *J. Chem. Soc., Dalton Trans.* **1992**, 3477.

27. Lu, Z.; Jun, C.-H.; de Gala, S. R.; Sigalas, M. P.; Eisenstein, O.; Crabtree, R. H. *Organometallics* **1995**, *14*, 1168.

28. Chatt, J.; Coffey R. S.; Shaw, B. L. *J. Chem. Soc.* **1965**, 7391.

29. Mann, B. E.; Masters, C.; Shaw, B. L. *J. Inorg. Nucl. Chem.,* **1971,** *33***,** 2195.

30. Meyer, T. J.; Huynh, M. H. V. *Inorg. Chem.* **2003**, *42*, 8140.

31. Che, C.-M.; Lau, T.-C. In *Comprehensive Coordination Chemistry II*; McCleverty, J. A.; Meyer, T. J., Eds.; Elsevier: Oxford, U.K., 2004; Vol. 5, pp 733–847.

32. Cipriano, R. A.; Levason, W.; Pletcher, D.; Powell, N. A.; Webster, M. *J. Chem. Soc., Dalton Trans.* **1987**, 1901.

33. Cipriano, R. A.; Hanton, L. R.; Levason, W.; Pletcher, D.; Powell, N. A.; Webster, M. *J. Chem. Soc., Dalton Trans.* **1988**, 2483.

34. Tamayo, A. B.; Alleyne, B. D.; Djurovich, P. I.; Lamansky, S.; Tsyba, I.; Ho, N. N.; Bau, R.; Thompson, M. E. *J. Am. Chem. Soc.* **2003**, *125*, 7377.

35. Jung, S.; Kang, Y.; Kim, H.-S.; Kim, Y.-H.; Lee, C.-L.; Kim, J.-J.; Lee, S.-K.; Kwon, S.-K. *Eur. J. Inorg. Chem.* **2004**, 3415.

36. Palmer, J. H.; Day, M. W.; Wilson, A. D.; Henling, L. M.; Gross, Z.; Gray, H. B. *J. Am. Chem. Soc.* **2008**, *130*, 7786.

37. Palmer, J. H.; Mahammed, A.; Lancaster, K. M.; Gross, Z.; Gray, H. B. *Inorg. Chem.* **2009**, *48*, 9308.

38. Dong, S. S.; Nielsen, R. J.; Palmer, J. H.; Gray, H. B.; Gross, Z.; Dasgupta, S.; Goddard, W. A. *Inorg. Chem.* **2011**, *50*, 764.

39. Cotton, F. A.; Wilkinson, G. Advanced Inorganic Chemistry, 5th ed.; Wiley-Interscience: New York, 1988; Chapter 19.

40. Ellison, I. J.; Gillard, R. D. *J. Chem. Soc., Chem. Commun*. **1992**, 851.

41. Holleman, A. F.;Wiberg, E.;Wiberg, N. Inorg. Chem., 101st ed.; Walter de Gruyter: Berlin, Germany, 2001.

42. Housecroft, C.E.; Sharp, A.G., "Inorganic Chemistry" 3rd ed.; Prentice Hall International: New York, 2008.

43. Hay-Motherwell, R. S.; Wilkinson, G.; Hussain-Bates, B.; Hursthouse, M. B. *Polyhedron* **1990**, *9*, 2071.

44. Pestovsky, O.; Bakac, A. *Inorg. Chem.* **2002**, *41*, 3975.

45. Srinivasan, A.; Toganoh, M.; Niino, T.; Osuka, A.; Furuta, H. *Inorg. Chem.* **2008**, *47*, 11305.

46. Trofimenko, S. *Chem. Rev.* **1993**, *93*, 943.

47. Trofimenko, S. *Polyhedron* **2004**, *23*, 197.

48. Bourget-Merle, L.; Lappert, M. F.; Severn, J. R. *Chem. Rev.* **2002**, *102*, 3031.

49. Roesky, P. W. *Chem. Soc. Rev.* **2000**, *29*, 335.

50. Barker, J.; Kilner, M. *Coord. Chem. Rev.* **1994**, *133*, 219.

51. Edelmann, F. T. *Coord. Chem. Rev.* **1994**, *137*, 403.

52. Sciarone, T.; Hoogboom, J.; Schlebos, P. P. J.; Budzelaar, P. H. M.; de Gelder, R.; Smits, J. M. M.; Gal, A. W. *Eur. J. Inorg. Chem.* **2002**, 457.

53. Bailey, P. J.; Pace, S. *Coord. Chem. Rev.* **2001**, *214*, 91.

54. Duncan, A. P.; Mullins, S. M.; Arnold, J.; Bergman, R. G. *Organometallics* **2001**, *20*, 1808.

55. Mullins, S. M.; Duncan, A. P.; Bergman, R. G.; Arnold, J. *Inorg. Chem.* **2001**, *40*, 6952.

56. Bazinet, P.; Wood, D.; Yap, G. P. A.; Richeson, D. S. *Inorg. Chem.* **2003**, *42*, 6225.

57. Soria, D. B.; Grundy, J.; Coles, M. P.; Hitchcock, P. B. *J. Organomet. Chem.* **2005**, *690*, 2278.

58. Wilder, C. B.; Reitfort, L. L.; Abboud, K. A.; McElwee-White, L. *Inorg. Chem.* **2006**, *45*, 263.

59. Rische, D.; Baunemann, A.; Winter, M.; Fischer, R. A. *Inorg. Chem.* **2006**, *45*, 269.

60. Robinson, S. D.; Sahajpal, A.; Steed, J. *Inorg. Chim. Acta* **2000**, *303*, 265.

61. Ogata, K.; Oka, O.; Toyota, A.; Suzuki, N.; Fukuzawa, S.-i. *Synlett* **2008**, 2663

62. Jones, C.; Mills, D. P.; Stasch, A. *Dalton Trans.,* **2008**, 4799.

63. Barker, J.; Kilner, M. *Coord. Chem. Rev.* **1994**, *133*, 219.

64. Rohde, J.-U.; Kelley, M. R.; Lee, W.-T. *Inorg. Chem.* **2008**, *47*, 11461.

65. Armarego, W. L. F.; Chai, C. *Purification of Laboratory Chemicals*, 5th ed.; Butterworth-Heinemann: Oxford, U.K., 2003.

66. Van der Ent, A.; Onderdelinden, A. L. *Inorg. Synth.* **1973**, *14*, 92.

67. Schmidt, H.-J.; Schäfer, H. J. *Angew. Chem., Int. Ed.* **1979**, *18*, 68.

68. Zepik, H. H.; Benner, S. A. *J. Org. Chem.* **1999**, *64*, 8080.

69. Hooft, R. W. W. *Collect*; Nonius BV: Delft, The Netherlands, 1998.

70. Otwinowski, Z.; Minor, W. *Methods Enzymol.* **1997**, *276*, 307.

71. SHELXTL: Program Library for Structure Solution and Molecular Graphics, version 6.12; Bruker Analytical X-Ray Systems, Inc.: Madison, WI, 2001.

72. Sheldrick, G. M. Acta Crystallogr., Sect. A: Found. Crystallogr. **2008**, A64, 112.

73. Kresze, G.; Hatjiissaak, A. *Phosphorus Sulfur Relat. Elem.* **1986**, *29*, 41.

74. Ramadas, K.; Srinivasan, N. *Tetrahedron Lett.* **1995**, *36*, 2841.

75. Srinivasan, N.; Ramadas, K. *Tetrahedron Lett.* **2001**, *42*, 343.

76. Ramadas, K.; Janarthanan, N.; Pritha, R. *Synlett* **1997**, 1053.

77. Lahoz, F. J.; Tiripicchio, A.; Tiripicchio Camellini, M.; Oro, L. A.; Pinillos, M. T., *J. Chem. Soc., Dalton Trans.* **1985**, 1487.

78. Cotton, F. A.; Poli, R., *Inorg. Chim. Acta* **1986,** *122*, 243.

79. Kanematsu, N.; Ebihara, M.; Kawamura, T., *Inorg. Chim. Acta* **1999,** *292*, 244.

80. Albinati, A.; Bovens, M.; Rüegger, H.; Venanzi, L. M. *Inorg. Chem.* **1997**, *36*, 5991.

81. Bernskoetter, W. H.; Lobkovsky, E.; Chirik, P. J. *Organometallics* **2005**, *24*, 6250.

82. Siegel, J. S.; Baldridge, K. K.; Linden, A.; Dorta, R. *J. Am. Chem. Soc.* **2006**, *128*, 10644.

83. Dahlenburg L.; Kuhnlein M. *Acta Cryst.* **2001**, *C57*, 709.

84. Cheung, W.-M.; Lai, C.-Y.; Zhang, Q.-F.; Wong, W.-Y.; Williams, I. D.; Leung. W.-H. *Inorg. Chim. Acta,* **2006**, *359*, 2712.

85. Bailey, P. J.; Pace, S. *Coord. Chem. Rev.* **2001**, *214*, 91.

86. Rische, D.; Baunemann, A.; Winter, M.; Fischer, R. A. *Inorg. Chem.* **2006**, *45*, 269.

87. Bailey, P. J.; Bone, S. F.; Mitchell, L. A.; Parsons, S.; Taylor, K. J.; Yellowlees, L. J. *Inorg. Chem.* **1997**, *36*, 867.

88. Bailey, P. J.; Bone, S. F.; Mitchell, L. A.; Parsons, S.; Taylor, K. J.; Yellowlees, L. J. *Inorg. Chem.* **1997**, *36*, 5420.

89. Irwin, M. D.; Abdou, H. E.; Mohamed, A. A.; Fackler, J. P., Jr. *Chem. Commun.* **2003**, 2882.

90. Mohamed, A. A.; Mayer, A. P.; Abdou, H. E.; Irwin, M. D.; Perez, L. M.; Fackler, J. P., Jr. *Inorg. Chem.* **2007**, *46*, 11165.

91. Coyle, J. P.; Monillas, W. H.; Yap, G. P. A.; Barry, S. T. *Inorg. Chem.* **2008**, *47*, 683.

92. Fandos, R.; Otero, A.; Rodriguez, A.; Terreros, P. *Collect. Czech. Chem. Commun.* **2007**, *72*, 579.

93. Green, S. P.; Jones, C.; Stasch, A. *Science* **2007**, *318*, 1754.

94. Jones, C.; Mills, D. P.; Rose, R. P.; Stasch, A. *Dalton Trans*. **2008**, 4799.

95. Bailey, P. J.; Grant, K. J.; Mitchell, L. A.; Pace, S.; Parkin, A.; Parsons, S. *J. Chem. Soc., Dalton Trans.* **2000**, 1887.

96. Coles, M. P.; Hitchcock, P. B. *Organometallics* **2003**, *22*, 5201.

97. Bazinet, P.; Wood, D.; Yap, G. P. A.; Richeson, D. S. *Inorg. Chem.* **2003**, *42*, 6225.

98. Soria, D. B.; Grundy, J.; Coles, M. P.; Hitchcock, P. B. *J. Organomet. Chem.* **2005**, *690*, 2278.

99. Rohde, J.-U.; Lee, W.-T. *J. Am. Chem. Soc.* **2009**, *131*, 9162.

100. Kelley, M. R.; Rohde, J.-U. Manuscript in preparation.

101. Chang, D.; Malinski, T.; Ulman, A.; Kadish, K. M. *Inorg. Chem.* **1984**, *23*, 817.

102. *CRC Handbook of Chemistry and Physics*, 89th ed.; Lide, D. R., Ed.; CRC Press/Taylor & Francis: Boca Raton, FL, 2008.

103. deBruin, B.; Budzelaar, P. H. M.; Gal, A. W. *Angew. Chem. Int. Ed.* **2004**, *43*, 4142.

104. Yoshikawa, N.; Masuda, Y.; Matsumura-Inoue, T. *Chem. Lett.* **2000**, 1206.

105. Grushin, V. V.; Herron, N.; LeCloux, D. D.; Marshall, W. J.; Petrov, V. A.; Wang, Y. *Chem. Commun.* **2001**, 1494.

106. Tamayo, A. B.; Alleyne, B. D.; Djurovich, P. I.; Lamansky, S.; Tsyba, I.; Ho, N. N.; Bau, R.; Thompson, M. E. *J. Am. Chem. Soc.* **2003**, *125*, 7377.

107. Jung, S.; Kang, Y.; Kim, H.-S.; Kim, Y.-H.; Lee, C.-L.; Kim, J.-J.; Lee, S.-K.; Kwon, S.-K. *Eur. J. Inorg. Chem.* **2004**, 3415.

108. Bond, A. M.; Colton, R.; Mann, D. R. *Inorg. Chem.* **1990**, *29*, 4665.

109. Hirani, B.; Li, J.; Djurovich, P. I.; Yousufuddin, M.; Oxgaard, J.; Persson, P.; Wilson, S. R.; Bau, R.; Goddard, W. A., III; Thompson, M. E. *Inorg. Chem.* **2007**, *46*, 3865.

110. Ringenberg, M. R.; Kokatam, S. L.; Heiden, Z. M.; Rauchfuss, T. B. *J. Am. Chem. Soc.* **2008**, *130*, 788.

111. Van der Ent, A.; Onderdelinden, A. L. *Inorg. Synth.* **1990**, *28*, 90.

112. Hursthouse, M. B.; Mazid, M. A.; Clark, T.; Robinson S. D. *Polyhedron* **1993**, *12*, 563.

113. Jiao, J.; Long, G. J.; Rebbouh, L.; Grandjean, F.; Beatty, A. M.; Fehlner T. P. *J. Am. Chem. Soc.,* **2005**, *127*, 17819.

114. Bhowruth, V.; Brown, A. K. Reynolds, R. C.; Coxon, G. D. Mackay, S. P.; Minnikin, D. E.; Besra, G. S. *Bioorg. Med. Chem. Lett.* **2006**, *16*, 4743.

115. Wu, A., Mader, E. A., Datta, A., Hrovat, D. A., Borden, W. T., and Mayer, J. M. *J. Am. Chem. Soc.* **2009**, *131*, 11985.

116. Abbreviations: TfO^- (= $CF_3SO_3^-$), trifluoromethanesulfonate or triflate anion.

117. Hagen, K. S. *Inorg. Chem.* **2000**, *39*, 5867.

118. Arnold, J.; Hoffman, C. G.; Dawson, D. Y.; Hollander, F. J. *Organometallics* **1993**, *12*, 3645.

119. Pascaly, M.; Duda, M.; Schweppe, F.; Zurlinden, K.; Müller F. K.; Krebs, B. *J. Chem. Soc., Dalton.* **2001**, 828.

120. Yang, X.-P.; Su, C.-Y.; Kang, B.-S.; Feng, X.-L.; Xiao, W.-L.; Liu, H.-Q. *J. Chem. Soc., Dalton.* **2000**, 3253.

121. Kloskowski, M.; Krebs, B. *Z. Anorg. Allg. Chem*., **2006**, *632*, 771.

122. Banerjee, S. R., Levadala, M. K., Lazarova, N., Wei, L., Valliant, J. F., Stephenson, K. A., Babich, J. W., Maresca, K. P., Zubieta, J. *Inorg. Chem.* **2002**, *41*, 6417.

123. Rodionov, V. O., Presolski, S. I., Gardinier, S., Lim, Y. H., and Finn, M. G. *J. Am. Chem. Soc.* **2007**, *129*, 12696.

124. Although the ^1H NMR spectrum of $[Fe(Me_3ntb)(NCCD_3)_2](OTf)_2$ does not provide a useful information in the literature, we have re-done the ^1H NMR experiment by using proper parameters to obtain a better spectrum.

125. Zalkin, A.; Templeton, D. H.; Ueki, T. *Inorg. Chem.* **1973**, *12*, 1641.

126. Posse, G. M. E.; Juri, M. A.; Aymonino, P. J.; Piro, O. E.; Negri, H. A.; Castellano, E. E. *Inorg. Chem.* **1984**, *23*, 948.

127. Wocadlo, S.; Massa, W.; Folgado, J. *Inorg. Chim. Acta* **1993**, *207*, 199.

128. Oh, N. Y.; Seo, M. S.; Lim, M. H.; Consugar, M. B.; Park, M. J.; Rohde, J.-U.; Han, J.; Kim, K. M.; Kim, J.; Que, L., Jr.; Nam, W. *Chem. Commun.* **2005**, 5644.

129. Haynes, W. M. *CRC Handbook of Chemistry and Physics*, 92nd ed.; CRC Press:

2011–2012.